Dark Cosmology Centre

Testing the Lambda-Cold Dark Matter model at galactic scales

A thesis submitted for the degree of
Doctor of Philosophy (PhD)
on October 8, 2008.
To be defended in Copenhagen, November 28, 2008.

Chloé Féron

Supervisor: Jens Hjorth

Co-supervisor: Steen H. Hansen

Dark Cosmology Centre, Niels Bohr Institute

Faculty of Science, University of Copenhagen

Cover painting: Philip Taaffe. Life at Sea , (2004). Oil and enamel on paper.

Acknowledgments

Writing this thesis brings along the opportunity to look back at the last three years, from the day I first came to Copenhagen till the end of my Ph.D now. There are many people I wish to thank.

First of all, I owe a great thanks to my advisor, Jens Hjorth, who made this PhD quite a unique experience, giving me at the same time freedom, advice, motivation and a lot of challenge. I learnt much from his teaching. And realized that a PhD is a lot more than a transition from studies to research. It is also a rare occasion in a life, when someone takes on to push further your education and abilities on a long period of time. The beauty of education being that once you have learnt to think, you can apply it not only to the area which you studied, but also to everything else which comes under the inspection of mind. During this PhD, I improved my knowledge and skills in astrophysics, but even much more my ability at thinking the world around me. And for that above all the rest, I am much grateful to Jens.

I would also like to thank all the people at DARK, for all the good time I spent there, and because the friendliness of the place made it like a home and family to me when I first arrived to Denmark. A special thanks to my fellow students at DARK, whose company helped me much through the grad student experience, and particularly Árdís, José María, Christina and Danka. Thank you also, Lisbeth, for all the great time I had sharing an

office with you, for your advice, and all our discussions!

My parents always supported me much in everything I wanted to do. Both their material support in allowing me so long studies, and the psychological support of their unwavering trust, helped me beyond anything else to follow my own way, and stand where I am today. Thank you.

I also have many friends that I wish to thank, for making life so much more enjoyable. My fantastic friends in Copenhagen, Ana, Helena, Djamel and Ulla, and also Marie-Louise and her sweet daughter Emma-Amalie, and Henrik my shiatsu teacher. Also those who, unfortunately for me, left Denmark one year earlier than I, Max, Marceau and Virginie. As well as my longtime friends in France, Christelle, Jean-Baptiste and Amandine. And of course all the others, who I enjoy meeting every time, but place is too short here to name them all.

One person I would like to mention specially is my sister Faustine. Her way through life has been for now full of difficulties, but she is a great example of strength in the face of adversity.

Last but not least, I thank Jeanluc very much for his great support in all the up and downs of this end of thesis period. And for his brave action of moving in to Denmark, reminding me everyday by his presence how amazing it is we met each other. Thank you for being my fellow traveler on the road of life.

Abstract

The Λ-Cold Dark Matter model has gained the place of cosmological paradigm, yet its success at explaining the large-scale universe is not reproduced at galactic scales. This thesis focus on aspects of testing the cosmological paradigm at galactic scales, by gaining insights both theoretically and observationally into the dark and baryonic matter distributions of galaxies.

Nonextensive statistical mechanics, a generalization of classical statistical mechanics designed to describe long-range interaction systems, has been proposed recently to predict the structure of dark matter halos, using stellar polytropes. A careful comparison of structural radial profiles of stellar polytropes with those of simulated dark matter halos is presented in this thesis. It establishes that nonextensive statistical mechanics is unable to predict the structure of dark matter halos.

Gravitational lensing provides a promising way of constraining the mass distribution of disk galaxies and measure their mass-to-light ratio. Unfortunately, only seven disk-galaxy lenses are known to date. Here is presented the first automated spectroscopic search for disk-galaxy lenses, using the Sloan Digital Sky Survey database. Eight disk-galaxy lens candidates are studied, using imaging and long-slit spectroscopy observations. Two new gravitational lenses are presented, which are probable disk and S0 galaxies, as well as four very interesting disk-galaxy lens candidates, and two probable lenses where the lens galaxy is either an S0 or elliptical galaxy. Higher resolution observations are needed to further study these systems. These results open promising perspectives for enlarging the sample of known disk-galaxy lenses, and gaining further understanding of the baryonic and dark matter distributions in disk galaxies.

Contents

List of Figures

List of Tables

Introduction

This thesis focus on aspects of testing the Λ-Cold Dark Matter (ΛCDM) cosmological paradigm at galactic scales. The thesis consists of two studies realized in a same perspective, that of gaining insights into the dark and baryonic matter distributions in galaxies. The two studies cover different domains, one investigating the theoretical prediction of dark matter (DM) halo structures using nonextensive statistical mechanics, the other turning to astronomical observation and the search for disk-galaxy lenses, in order to probe the mass-to-light ratio of disk galaxies.

Chapter 1 sets the cosmological context in which this thesis was undertaken. While the paradigm model is supported at large scales by most observations, comparison of ΛCDM predictions with observed galactic DM halos has evidenced long-standing problems. Simulated DM halos present steep inner density cusps, while observed DM halos at galactic scales have a flat density core in the inner parts. Moreover, disk galaxies grown in ΛCDM simulations do not reproduce the zero point of the Tully-Fisher relation, though it constitutes a fundamental property of observed disk galaxies. Physical understanding of DM halo structures and baryonic mass distributions in galaxies is missing to gain further insights into the above mentioned issues.

The study presented in Chapter 2 is motivated by recent claims that nonextensive sta-

tistical mechanics, a generalization of classical statistical mechanics, could describe DM halo structures, derived from first principles. Nonextensive statistical mechanics is a formalism that statistically describes the equilibrium states of long-range interaction systems. It is thus particularly well suited to study DM halos, which interact via the gravitational force alone. This formalism predicts the equilibrium states of DM halos to be described by stellar polytropes, which are well-known models in stellar physics. To clarify the contradictions found in previous studies, and establish whether nonextensive statistical mechanics can theoretically predict DM halo structures, we perform a careful comparison of stellar polytropes with simulated DM halos.

In Chapter 3 is presented the first automated spectroscopic search for disk galaxy lenses. Gravitational lensing with disk galaxies is a promising way to measure the mass-to-light ratios of disk galaxies, and thus to gain insights into their structure, stellar population, and their dark and baryonic matter distributions. Unfortunately, only seven disk-galaxy lenses are known to date. In this chapter, a selection of height disk-galaxy lens candidates from the Sloan Digital Sky Survey is presented, as well as imaging and long-slit spectroscopy follow-up, data reduction, and candidate by candidate analysis.

Finally, conclusions of the studies presented in this thesis are summarized in Chapter 4. In addition, mathematical details relative to Chapter 2 can be found in Appendices A and B. At last, Appendix C presents statements of coauthorship for publications including some of the work presented in this thesis.

Chapter 1

Testing the Lambda-Cold Dark Matter model at galactic scales

Abstract

The current cosmological paradigm, the Lambda-Cold Dark Matter (ΛCDM) model, is supported at large scales by a wealth of observations in remarkable agreement. However, its extrapolation to galactic scales raises important challenges: observations of galactic dark matter (DM) halos do not corroborate the predictions of cosmological simulations. Difficulties in testing the ΛCDM model at galactic scales originate largely in the lack of theoretical predictions for the structure of DM halos and in the difficulty of subtracting the baryonic mass distribution from galaxy observations to probe the structure of observed DM halos.

1.1 Introduction

1.1.1 The ΛCDM model: a brief introduction

Our current cosmological picture of the Universe is described by the ΛCDM concordance model, which relies on two essential but unknown components: Dark Energy (DE) and Cold Dark Matter (CDM). According to large-scale observations, these two "dark" components account for ~ 95 % of the energy content of the Universe (Komatsu et al. 2008). However, ΛCDM being a model and not a theory, it does not explain the nature and origin of DE and CDM.

Evidences for DM are found at both large- and galactic-scales. Yet, five decades after the existence of DM was inferred, no experiment to date successfully detected DM particles. From a theoretical point of view, many extensions of the Standard Model of particle physics predict the existence of particles having the characteristics of DM. Cold DM, such as the weakly interacting massive particles (WIMPs) predicted by supersymmetry, is favored by cosmological numerical simulations compared to hot DM such as neutrinos.

DE is probed on large-scales, the main evidence for its existence coming from the distance measurements of Type Ia supernovae. DE is a negative pressure field (acting as a repulsive gravity) filling uniformly the Universe. From a theoretical point of view, DE could be a cosmological constant, associated to the energy of vacuum. However, the measured value of the cosmological constant is off by 120 orders of magnitude from predictions of particle physics. DE could otherwise be a scalar field (possibly varying with time), as predicted by many extensions of the Standard Model of particle physics. To date, no scalar field has ever been observed, but the discovery of the Higgs boson at the Large Hadron Collider would prove the existence of such physical fields in nature.

It is interesting that the necessity for both DM and DE arise from discrepancies with the expected behaviour of the gravitational force. Indeed, the idea of DM is derived as an explanation for galaxies that appear more massive at large radii than expected from their baryonic content, while DE is born out of an attempt at explaining how the Universe can expand faster than expected considering the effect of gravitational attraction on large scales, requiring the addition of a repulsive gravitational effect. Based on these considerations, the thought naturally comes that perhaps our theoretical description of gravity has to be revised, instead of introducing two "ad hoc" components to account for the observed discrepancies. However, no attempts to improve our understanding of gravity have yet proposed a model or theory which could seriously challenge the ΛCDM model.

The success of the ΛCDM paradigm is based on an ensemble of large-scale observations in remarkable agreement. Measurements of the cosmological microwave background (CMB), Type Ia supernovae (SNeIa) distances, and baryon acoustic oscillations (BAO) in the distribution of galaxies, all agree on the values of the six parameters of the ΛCDM

model. The currently favored values for the composition of the Universe are determined from the results of the Wilkinson Microwave Anisotropy Probe (WMAP) satellite five years data release, joint to the constraints from SNeIa and BAO. The reduced energy density of DE is $\Omega_\Lambda = 0.72$, that of baryons is $\Omega_b = 0.04$, that of DM is $\Omega_{DM} = 0.24$, and finally the reduced Hubble constant is $h = 0.70$ (Komatsu et al. 2008).

However, while a consistent picture emerge from observations of CMB, SNeIa and BAOs, some studies only marginally cited by the mainstream cosmology literature find that observations do not confirm so well ΛCDM predictions. For example, while the determination of the Hubble constant by Freedman et al. (2001) leads to $h \sim 0.70$ in agreement with WMAP results, the study of Sandage et al. (2006) finds $h \sim 0.62$, although both studies are based on *Hubble Space Telescope* (HST) data. Difference between the two studies comes from the adopted Cepheid distances for calibrating SNeIa. The value from Sandage et al. (2006) is in good agreement with values of the Hubble constant from gravitational lensing, using time delay measurements. Another example comes from the measure of the Sunyaev-Zel'dovich (SZ) effect in galaxy clusters. The SZ effect is due to the passage of CMB photons through the hot gas of clusters: as CMB photons gain energy from interacting with free electrons, this distorts the CMB energy spectrum by shifting CMB photons toward higher energies. The works of Bielby & Shanks (2007) and Lieu et al. (2006) based on WMAP three years data release find a SZ effect significantly lower than expected from cluster X-ray data predictions. On the other hand, the study of Bonamente et al. (2006), which is not based on WMAP data but on radio interferometric techniques, finds a SZ effect at the expected level. There is no explanation yet for the origin of this difference. However, it is a puzzling problem, as the presence of SZ effect is a probe of the cosmological origin of CMB. Other contradictory results about the consistency of the ΛCDM model with cosmological observations are found in the literature. However, we do not treat the topic further, for that section is meant to be a brief introduction to the current cosmological context. But it reminds of the necessity of continuing testing the ΛCDM model, although it might seem a well established paradigm.

1.1.2 Extrapolation to galactic scales

The ΛCDM model is based on large-scale observations. To be a consistent cosmological model, it also must explain the formation of structures in the Universe, and be able to predict the structures we observe at present.

We can measure the matter density fluctuations present at the time of the primordial Universe by observing the temperature anisotropies of the CMB. However, we are for now limited by instrumental resolution, and can only detect angular scales in the CMB anisotropies corresponding to the large-scale structures of the Universe (that is, galaxy clusters and larger structures).

The power spectrum of initial density fluctuations can be extrapolated to smaller scales using the predictions of inflationary theories. A period of inflation early in the history of the Universe is the currently favored explanation to account for the flatness, homogeneity and isotropy of the Universe today, as well as for the absence of magnetic monopoles. Quantum fluctuations formed during this inflationary period would freeze when inflation stops, forming a nearly scale-invariant spectrum of density perturbations of the form $P(k) \propto k^{n_s}$ with the spectral index n_s close to 1. Observations of the CMB by the WMAP satellite confirmed this prediction by measuring a value of the spectral index $n_s = 0.960 \pm 0.014$ (Komatsu et al. 2008).

The evolution of these small matter overdensities to form the complex structures in the Universe today can be described by a linear growth as long as the amplitude of the density fluctuations is small ($|\delta\rho/\rho| << 1$). However, as dense regions become denser due to gravitational collapse, their evolution becomes more complex, including non-linear physics, and must be modeled by powerful N-body simulations or semi-analytical models. For small scale structures not to be scattered during the first stages of structure formation, a large amount of CDM is needed, that is, a large amount of presureless matter which is governed by gravitational collapse only, with no radiation pressure. This allows small structures which will be the actual galaxies to form first, and reach equilibrium before large-scale structures, as observed in the Universe.

1.1.3 The structure of simulated CDM halos

The CDM halos grown in cosmological N-body simulations have universal properties, independent of their formation and environment, and independent of their size (dwarf, galaxy or cluster). Navarro, Frenk and White proposed an empirical fitting formula to describe the universal density profile of CDM halos, known as the NFW profile (Navarro et al. 1996). It is given by

$$\rho(r) = \frac{\delta_c \ \rho_{crit}}{(r/r_s)(1 + r/r_s)^2}, \tag{1.1}$$

where δ_c is a characteristic density contrast, r_s is a scale radius, and ρ_{crit} is the critical density of the Universe. The profile tends to a logarithmic density slope of -3 in the outer parts, and of -1 in the inner parts. The central cusp is one of the important predictions of cosmological simulations. An even steeper cusp was proposed in the Moore profile with a central logarithmic density slope of -1.5 (Moore et al. 1999). However, no agreement exist on the value of the central logarithmic slope of simulated DM halos, as simulations do not converge to an asymptotic central slope in the radial range where they are robustly resolved.

In the past years, the Sérsic profile (Sérsic 1963, 1968) was proposed as a very good fit to simulated CDM halos, matching more accurately the inner parts of recent high resolution simulations than the usual NFW profile (Navarro et al. 2004). The Sérsic profile is given by

$$\rho(r) = \rho_e \ exp\left(-d_\alpha \left[(r/r_e)^\alpha - 1\right]\right), \tag{1.2}$$

where α is a shape parameter, ρ_e is the density at the effective radius r_e, and d_α is a function of α such that half the total mass is enclosed within r_e (Navarro et al. 2004; Graham et al. 2006). In contrast to the broken power-law profiles proposed in Navarro et al. (1996) and Moore et al. (1999), the Sérsic profile has a continuously varying density slope. Interestingly, the Sérsic profile also provides a good description of luminous matter structures (Merritt et al. 2005) and was first developed to fit galaxy luminosity profiles (Sérsic 1963, 1968).

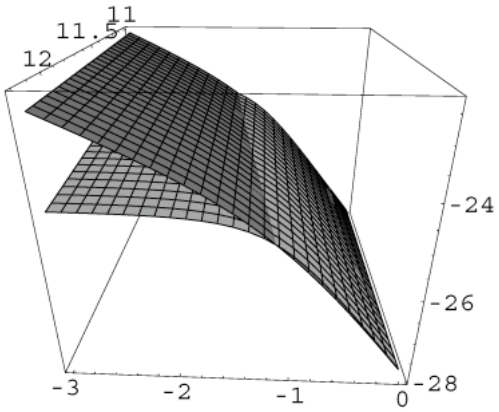

Figure 1.1: *DM halo density profile from spiral galaxy observations versus NFW model density profile, for objects of the same mass. The figure shows the density radial profile as a function of normalized radius. The third axe shows the dependence on virial mass. Credit: Salucci et al. (2007), MNRAS 378, 41.*

In addition to a universal density profile, simulated CDM halos show other universal properties. Their pseudo phase-space density ρ/σ^3 (where σ is the velocity dispersion) follows a power law in radius (Taylor & Navarro 2001), and the velocity anisotropy profile is related to the logarithmic density slope by a nearly linear relation (Hansen & Moore 2006). Finally, a universality of velocity distribution functions was identified in Hansen et al. (2006).

1.2 Comparison with galaxy observations

We will now compare the predictions of cosmological N-body simulations with galaxy observations. We will focus on two major and long-standing issues for the ΛCDM model, the cusp-core problem (§ 1.2.1) and the Tully-Fisher relation zero point problem (§ 1.2.2).

1.2.1 The cusp-core problem

While simulated CDM halos exhibit a steep density profile in the inner parts, forming a cusp, DM halos observed at galactic scales point to a shallow density profile in the inner parts, forming a flat core. This discrepancy is a well-known problem of the ΛCDM model

when compared to galaxy observations.

Measuring DM distribution in galaxies is difficult due to the necessity of first removing the contribution of baryonic matter. However, in dwarf galaxies and low luminosity spiral galaxies, DM is thought to be dominant on the entire radial range of the galaxy, allowing a good determination of its distribution through rotation curve measurements. The observed mass distribution of their DM halos reveals a core in the central parts, in contradiction with the cusp predicted by ΛCDM simulations (see de Blok & Bosma (2002) and references therein). Recent work on normal surface brightness spiral galaxies (see Gentile et al. (2004) and Salucci et al. (2007), and references therein) leads to the same conclusion, finding that rotation curves are better fitted with a DM component described by a core profile such as a Burkert profile (Burkert 1995) than by an NFW profile (see Fig. 1.1).

While the large error bars on observations and the low resolution of simulations were initially invoked to account for this discrepancy, both domains greatly improved the resolution of their results during the past years. Still, high resolution simulations find a central cusp (Navarro et al. 2004) while high resolution rotation curves of low surface brightness and normal spiral galaxies still find evidence for a central core in galactic DM halos (de Blok & Bosma 2002; Gentile et al. 2004; Kassin et al. 2006). Adding adiabatic contraction in simulations to include the effect of baryons on CDM halos even steepen the central cusp. Although some mechanisms have been proposed to smooth the cusp of initial CDM halos into a core after evolving along with baryonic matter in the galaxy (see Sellwood (2008), and references therein), no agreement is found to explain this major discrepancy between observed galaxies and ΛCDM predictions.

The study presented in Chapter 2 is related to the cusp-core problem, by trying to find a theoretical prediction for DM halo structures, which would settle the issue between cored or cuspy inner parts for DM halos.

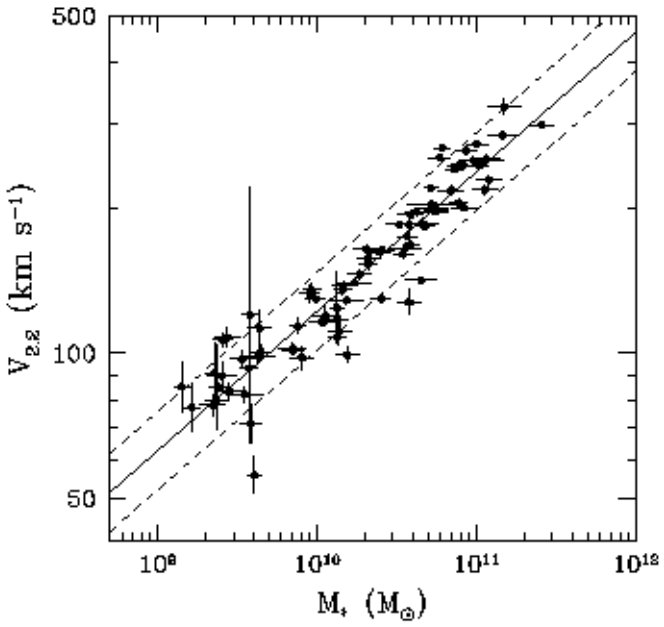

Figure 1.2: *Observed Tully-Fisher relation in the i band, with the luminosity converted to a stellar mass using a chosen mass-to-light ratio. Credit: Gnedin et al. (2007), ApJ 671, 1115.*

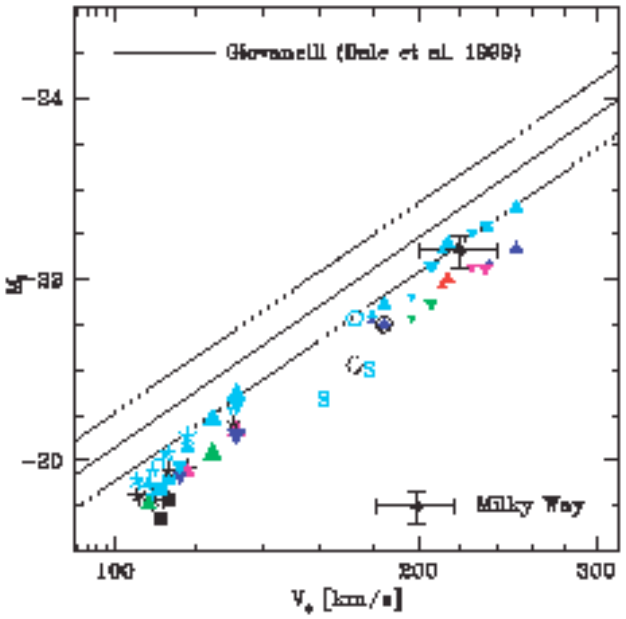

Figure 1.3: *Tully-Fisher relation from various simulations (marks), compared to the observed Tully-Fisher relation (black line), and to the value observed for the Milky Way (cross). Credit: Portinari & Sommer-Larsen (2007), MNRAS 375, 913.*

1.2.2 The Tully-Fisher relation zero point problem

A second problem arise, when comparing simulations including baryons in addition to DM with observed disk galaxies. A fundamental property of disk galaxies is expressed by the Tully-Fisher (TF) relation (Tully & Fisher 1977). As appears in Fig. 1.2, the rotational velocity of disk galaxies, tracing both baryonic and dark matter, is related to the luminosity of disk galaxies, tracing the baryonic matter alone, in a linear relation showing very small intrinsic scatter (Courteau et al. 2007). However, simulated disk galaxies are systematically offset from the observed galaxies with respect to the TF relation (see Fig. 1.3).

Disk galaxy formation models based on ΛCDM systematically predict disk galaxies with too high rotational velocity with respect to observed galaxies, corresponding to too concentrated CDM halos in simulations. This problem was first announced in Navarro & Steinmetz (2000b,a). While the simulations of disk galaxies improved, the problem did not disappear, as indicated by the recent literature on the topic (van den Bosch et al. 2003; Dutton et al. 2007; Gnedin et al. 2007; Portinari & Sommer-Larsen 2007). It is possible to simulate individual disk galaxies reproducing the characteristics of observed ones (e.g. Governato et al. 2004; Robertson et al. 2004), but the global properties of simulated disk galaxies could not reproduce simultaneously the zero point of the TF relation and the galaxy luminosity function.

However, a recent study by Governato et al. (2007) simulated realistic disk galaxies falling on the observed TF relation, using a higher resolution cosmological simulation. Therefore, the problem might originate in the too low resolution of previous simulations. On the other hand, a recent study based on observations of stars in the Solar Neighborhood found the Milky Way (MW) to be offset from the observed TF relation by about the same amount as simulated disk galaxies (Flynn et al. 2006, and Fig. 1.3 in the present section). This suggests another possible origin of the TF relation zero point problem, that simulations reproduce the MW model but the MW might not be representative of all disk galaxies.

In Chapter 3, we turn to the latter as a possible origin of the TF relation zero point

problem, and search for disk-galaxy lenses, which would allow to measure the mass-to-light ratio of disk galaxies and constrain independently their baryonic mass distribution.

1.3 Difficulties in comparing simulations to observations

The main difficulty in comparing simulations with observations is our lack of understanding of the physical processes underweaving the formation of pure DM structures and the effect of baryons on them. We will treat these two aspects in § 1.3.1 and § 1.3.2.

1.3.1 Lack of theoretical predictions for the structure of DM halos

Numerical simulations provide us with a wealth of information on the structure of CDM halos, yet until now, they did not further improve our understanding of the physics at work in the process. Indeed, the nonlinear physics involved and the repeated mergers that halos encounter through hierarchical formation does not allow to trace back a simple physical picture of their evolution.

Analytical and semi-analytical studies become necessary in order to gain some understanding in the universal properties of simulated CDM halos. In particular, because of the disagreement between observations and simulations (and between simulations themselves) on the value of the central logarithmic density slope of DM halos, obtaining theoretical predictions on that matter is important. Simple analytic considerations using a central density profile of the form $\rho \propto r^{\beta}$ suggest a value of β greater than -2 (Williams et al. 2004). By using the spherically symmetric and isotropic Jeans equation (Binney & Tremaine 1987), constraints can be put on the central parts such as $-3 \leq \beta \leq -1$ (Hansen 2004). These two results suggest that there is indeed a cusp in the central parts of pure DM halos. Additionally, the universal power-law profile of the pseudo phase-space density ρ/σ^3 seems to originate not in the result of hierarchical merging as was proposed in Syer & White (1998),

but in the outcome of violent relaxation (Austin et al. 2005). A complementary approach consists in using the universal properties found in simulated halos to constrain the Jeans equation and find corresponding distribution functions which could analytically describe the structure of DM halos (Dehnen & McLaughlin 2005; Van Hese et al. 2008).

In this thesis we will consider an alternative approach which could provide analytical predictions for the structure of DM halos. While the works cited above are based on classical statistical mechanics for describing the long-range interaction of particles in a collisionless system, another approach has been recently proposed that relies on a generalization of statistical mechanics encompassing the effect of long-range interaction by the use of a generalized entropy (Tsallis 1988). This formalism was shown by recent studies to be a promising way to predict the structure of DM halos from theoretical grounds (Hansen et al. 2005; Leubner 2005; Zavala et al. 2006; Kronberger et al. 2006). We will investigate this possibility in Chapter 2.

1.3.2 Baryons contribution

From an observational point of view, it is difficult in galaxies to isolate the DM component from the baryonic matter contribution, and therefore to measure the DM distribution without assumptions about the baryonic mass distribution. One often used technique is to assume a maximum disk (van Albada & Sancisi 1986) in spiral galaxies, that is, that almost all the mass contribution at the maximum rotational velocity comes from the disk. Although it seems in general agreement with rotation curves of spiral galaxies (Salucci & Persic 1999), it also naturally implies a low concentration of DM in the inner parts, in contradiction with ΛCDM predictions. An important element missing in practice, that would allow to determine the DM distribution with no assumptions about the baryonic matter contribution, is the mass-to-light (M/L) ratio of disks and bulges in spiral galaxies. These ratios allow to convert the observed luminous distribution of baryonic matter into its mass distribution, and provides a direct access to the remaining mass distribution, namely that of DM. In Chapter 3, we will consider the current knowledge about the M/L ratios

of disk galaxies, and present a search for new disk-galaxy lenses in the Sloan Digital Sky Survey, which constitutes a promising way of providing direct measurements of the M/L ratios of disk galaxies.

Part of this chapter is published as: C. Féron & J. Hjorth (2008) – *"Simulated Dark-Matter Halos as a Test of Nonextensive Statistical Mechanics,"* Physical Review E 77, 022106.

Chapter 2

Can the structure of DM halos be predicted by nonextensive statistical mechanics?

Abstract

Nonextensive statistical mechanics is a generalization of classical statistical mechanics, proposing a generalized entropy to describe long-range interaction systems. The theory predicts the equilibrium states of DM halos to be of the form of stellar polytropes (SPs), parameterized by the polytropic index n. To clarify contradictions in previous studies and establish whether SPs predicted by nonextensive statistical mechanics can describe DM halo structures, radial profiles of SPs are carefully compared to those of simulated CDM halos.

2.1 Introduction

In this chapter we will consider a possible approach to predict theoretically the structure of DM halos. We will use a generalization of classical statistical mechanics, named nonextensive statistical mechanics (Tsallis 1988), which proposes to describe the statistical equilibrium states of systems in which long-range forces are at work. This is particularly well-suited to the case of DM halos, as DM particles interact via the long-range gravitational force only.

The persistence of the cusp-core problem (§ 1.2.1) when comparing the predictions of simulations to DM halos observed in galaxies makes the theoretical prediction of DM halo structures a question of importance. Although the equilibrium structures of DM halos

can be predicted by classical statistical mechanics, there is an infinite number of solutions (Binney & Tremaine 1987). In contrast, nonextensive statistical mechanics restrict the range of solutions for the equilibrium structures of DM halos to the class of SPs. These are well-known structures in astrophysics, used to describe the structure of stars (Chandrasekhar 1939). We will investigate in this chapter whether SPs can describe DM halo structures.

More precisely, we will compare SPs with the profiles of simulated CDM halos. While DM halos observed in galaxies might be shaped partly by the presence of baryons, DM halos grown in CDM simulations are ideal to be compared with the predictions of nonextensive statistical mechanics, being pure collisionless self-gravitating systems.

SPs can describe a large range of different structural shapes depending on the value of the polytropic index n ($0 \leq n \leq \infty$). For small n, the outer parts of the density profile is very steep, while for large n, SPs have a shallow density profile, tending to the isothermal density profile for $n \to \infty$ (Binney & Tremaine 1987).

The study presented in this chapter is motivated by recent claims that the structures predicted by nonextensive statistical mechanics for collisionless self-gravitating systems could give a good description of DM halos (Hansen et al. 2005; Leubner 2005; Zavala et al. 2006; Kronberger et al. 2006). The value of the polytropic index $n = 16.5$ was proposed as fitting best simulated halos, compared to other values of n (Kronberger et al. 2006). However, a contradiction appears in the aforementioned studies, some of them using SPs with a central core, the other using SPs with a central cusp, while no explanation is given of that difference.

In this chapter, we will study both cored and cuspy SPs, and clarify the situation by finding that only cored SPs can be consistently compared with simulated CDM halos. We will then compare cored SPs with simulated CDM halos for the entire range of polytropic index n, and investigate whether any of the solutions predicted by nonextensive statistical mechanics can be used to describe the structure of DM halos.

2.2 Nonextensive statistical mechanics and stellar polytropes

2.2.1 What is nonextensive statistical mechanics?

An introduction to nonextensive statistical mechanics is presented in this section. As the topic is wide to cover, we will focus on the aspects which are relevant for the rest of the study.

Nonextensive statistical mechanics was proposed by C. Tsallis in 1988, based on the idea of a generalized entropy. He found that a formalism similar to that of thermodynamics could be derived using the generalized entropy, leading to the development of a generalized formalism for thermodynamics and statistical mechanics. The underlying concept is as follows. In thermodynamics and statistical mechanics, a unique solution for the entropy exists to describe the equilibrium state of a collisional system (e.g., an ideal gas), the Boltzmann-Gibbs entropy. However, an infinite number of solutions for the entropy exists to describe systems without collisions, that is, long-range interaction systems. In nonextensive statistical mechanics, a generalized entropy is proposed, parameterized by an index q. When $q = 1$, the generalized entropy is equal to the Boltzmann-Gibbs entropy, and hence describes collisional systems. In contrast, when $q \neq 1$, the generalized entropy describes systems where long-range interactions between the elements are at play. Both short- and long-range interaction systems (that is, collisional and collisionless systems) can thus be described with a same entropy formulation in this formalism.

Most systems in nature are constituted of elements interacting through long-range interactions, that is, the electromagnetic and gravitational interaction. Therefore, nonextensive statistical mechanics have applications in many domains, from self-gravitating systems to solar neutrinos, or plasma physics, Bose-Einstein condensation, biological systems, geophysics or even theory of finance, among others[1]. In this work we will focus exclusively on the application of nonextensive statistical mechanics to the field of astrophysical self-

[1] see `http://tsallis.cat.cbpf.br/biblio.htm` for a complete overview.

gravitating systems.

A few concepts are reviewed in the following, which are useful to the understanding of the theory.

Entropy

Entropy is a fundamental quantity in thermodynamics. In a system about which we know macroscopic quantities (e.g., the total temperature, the total energy, or the total mass) but not the behaviour of each element, entropy is a measure of the lack of information about the initial conditions. It is used to statistically predict the most probable state of the system once it has reached equilibrium, regardless of the details of its evolution.

The maximum entropy principle is commonly used to predict the equilibrium state of systems made of a large number of elements. This principle states that the distribution which maximizes the entropy of a system is the distribution which expresses the maximum uncertainty about what we don't know. That is, it expresses what we know about the system, but is the least biased by assumptions concerning the missing information. It is used as a corner stone of classical statistical mechanics, as well as in nonextensive statistical mechanics, and in many information related theories.

Short-range interaction systems

A short-range interaction system is a system in which the elements exchange energy and thus information through collisions. A classical example of a short-range interaction system is an ideal gas. The thermodynamical equilibrium state of an ideal gas corresponds to its maximum entropy state, for which all microstates are equiprobable. Indeed, the elements of the system interacted by collisions and lost all information about their initial state. This maximum entropy state is given by the usual Boltzmann-Gibbs entropy. Since all information is exchanged on short ranges, the entropy is additive, meaning that the entropy of a system is equal to the sum of the entropies of its subsystems:

$$S(A+B) = S(A) + S(B), \tag{2.1}$$

where $S(A)$ and $S(B)$ are respectively the entropy of the subsystems A and B, and $S(A+B)$ is the total entropy of the system.

Long-range interaction systems

If the elements of a system interact through long-range forces, such as the electromagnetic or gravitational force, the spatial and temporal evolution of the system become very complex. In the case of a gravitating system, each of the elements interacts with all the others, that is, the system is self-interacting, and memory effects appear due to nonlocality. In classical statistical mechanics, the evolution of astrophysical self-gravitating systems is predicted using the mechanisms of violent relaxation and incomplete mixing to account for the exchange of energy between its elements in the absence of collisions (Lynden-Bell 1967; Tremaine et al. 1986; Binney & Tremaine 1987).

Back to nonextensive statistical mechanics

Nonextensive statistical mechanics aims at extending the formalism of Boltzmann-Gibbs thermodynamics and classical statistical mechanics to long-range interaction systems by the introduction of a generalized entropy S_q, given by

$$S_q = k_B \frac{1 - \sum_{i=1}^{W} p_i^q}{q-1} \ (q \in R). \tag{2.2}$$

It reduces in the limit $q \to 1$ to the Boltzmann-Gibbs entropy

$$S_{BG} = -k_B \sum_{i=1}^{W} p_i \ln p_i, \tag{2.3}$$

where p_i is the probability of finding the system in the microstate i, W is the number of microstates i for a given macrostate, and k_B is the Boltzmann constant.

The generalized entropy is parameterized by an index q, sometimes called the entropic index. When the index $q \neq 1$, the entropy of the system is nonextensive, meaning that it is not possible to sum the entropies $S_q(A)$ and $S_q(B)$ of two subsystems A and B. However,

the generalized entropy S_q is conveniently pseudo-additive:

$$S_q(A+B) = S_q(A) + S_q(B) + (1-q)S_q(A)S_q(B). \tag{2.4}$$

The third term accounts for coupling between the subsystems, due to nonlocal effects from long-range interaction. We note that when $q = 1$, equation 2.4 reduces to equation 2.1, which describes the entropy of short-range interaction systems.

Intuitively, one can expect the index q to account for the degree of nonextensivity in the system. However, studies started to probe the physical meaning of q only recently (Silva & Alcaniz 2004; Jiulin 2006). As it is not clearly defined yet, we will consider that q is only a parameterization index.

2.2.2 Predictions for the equilibrium structures of astrophysical self-gravitating systems

We will present in this section how SPs, a model long-used in theoretical astrophysics to describe the structure of stars, emerge from the formalism of nonextensive statistical mechanics when applied to astrophysical self-gravitating systems. More details on the derivation of the polytropic distribution function from extremizing the generalized entropy S_q are given in Appendix A. SPs themselves, as used in classical statistical mechanics, will be presented in § 2.3.

The study of astrophysical self-gravitating systems was one of the first applications of nonextensive statistical mechanics (Plastino & Plastino 1993). Astrophysical self-gravitating systems are structures in which the elements (e.g., stars, DM particles) interact via the long-range gravitational force, and collisions are negligible.

The system is described by the distribution function $f(\mathbf{x},\mathbf{v})$, where $\mathbf{x}$ and $\mathbf{v}$ are the position and the velocity of each element. The behaviour of the system is governed by the

collisionless Boltzmann equation, or Vlasov equation (Binney & Tremaine 1987):

$$\frac{\partial f(\mathbf{x},\mathbf{v})}{\partial t} + \mathbf{v} \cdot \frac{\partial f(\mathbf{x},\mathbf{v})}{\partial \mathbf{x}} - \nabla\phi \cdot \frac{\partial f(\mathbf{x},\mathbf{v})}{\partial \mathbf{v}} = 0, \tag{2.5}$$

where ϕ is the gravitational potential.

The Vlasov equation has an infinite number of solutions of the form $S = -\int C(f) d^6\tau$, where S is the entropy of the system, $C(f)$ is a convex function, and $d^6\tau$ is a phase-space element (Tremaine et al. 1986). For example, the Boltzmann-Gibbs entropy S_{BG} corresponds to the distribution function known as the isothermal distribution (Binney & Tremaine 1987). Although the distribution functions which are solutions of the Vlasov equation can be used as models to describe the structure of self-gravitating systems (for example, see Hjorth & Madsen (1991)), classical statistical mechanics can not predict which ones among the infinite number of solutions correspond to the equilibrium states of self-gravitating systems.

In the case of nonextensive statistical mechanics, the range of solutions is restricted to the generalized entropy S_q which reads as

$$S_q = -\frac{1}{q-1} \int (f(\mathbf{x},\mathbf{v})^q - f(\mathbf{x},\mathbf{v})) d^6\tau. \tag{2.6}$$

Following the maximum entropy principle, S_q can be extremized at fixed mass and energy using the Lagrange multipliers (Plastino & Plastino 1993), leading to a spherically symmetric isotropic system with a distribution function of the form

$$f(\mathbf{x},\mathbf{v}) \propto \epsilon^{1/(q-1)}, \tag{2.7}$$

where ϵ is the relative energy per unit mass. This is a distribution function similar to the one of SPs (Binney & Tremaine 1987)

$$f(\mathbf{x},\mathbf{v}) \propto \epsilon^{n-3/2} \quad (\epsilon > 0), \tag{2.8}$$

$$f(\mathbf{x},\mathbf{v}) = 0 \quad (\epsilon \leq 0), \tag{2.9}$$

when identifying the polytropic index n as

$$n = \frac{3}{2} + \frac{1}{q-1}. \tag{2.10}$$

Therefore, the extremization of the generalized entropy S_q under fixed mass and energy for collisionless self-gravitating systems leads to the prediction that equilibrium states of astrophysical self-gravitating systems are described by SPs.

New formalism

In a newer version of the theory (Tsallis et al. 1998), the fundamental quantity describing the system is not the distribution function $f(\mathbf{x},\mathbf{v})$ anymore, but the probability function $p(\mathbf{x},\mathbf{v})$. Both functions are related but not identical (see Appendix A). The generalized entropy of eq. 2.2 now reads as

$$S_q = -\frac{1}{q-1}\int (p(\mathbf{x},\mathbf{v})^q - p(\mathbf{x},\mathbf{v}))d^6\tau. \tag{2.11}$$

In this new formalism, the constraints under which the generalized entropy S_q is extremized are the total energy and the normalization of the probability function. This leads to a solution for the probability function, corresponding to the maximum entropy state, from which it is possible to derive the distribution function of the system (Appendix A, eq. A.13), which is the physically relevant distribution we are interested in.

This leads to an equilibrium distribution function of the form (Taruya & Sakagami 2003)

$$f(\mathbf{x},\mathbf{v}) \propto \epsilon^{q/(1-q)}. \tag{2.12}$$

It still corresponds to the distribution function of SPs, this time with

$$n = \frac{1}{2} + \frac{1}{1-q}. \tag{2.13}$$

We see that the change of formalism in nonextensive statistical mechanics did not modify the predictions for the equilibrium structure of astrophysical self-gravitating systems (it is still SPs), but it did change the relation between the polytropic index n of SPs and the parameter q of the theory (eqs. 2.10 and 2.13). It is important to emphasize that our study will be completely independent of these definition problems, as it focus on the application of the theory, and not on its basis. We will study SP profiles parameterized by the polytropic index n, hence the relation between this parameter and the index q will not need to be considered.

2.3 Application to DM halos

We will now focus on the application of nonextensive statistical mechanics to DM halos. The nature of DM particles is unknown, but observations indicate that they are very weakly interacting and have a mass. Therefore, DM halos are collisionless systems whose elements interact via the long-range gravitational force only, allowing a direct comparison to the theory.

The application of nonextensive statistical mechanics to describe the structure of DM halos was considered only recently. Velocity distributions of isotropic collisionless self-gravitating systems following a power-law density profile were found to be well described by the velocity distribution derived from nonextensive statistical mechanics (Hansen et al. 2005). Comparisons of SP profiles with simulated CDM halos or with DM halos observations led to the conclusion that SPs can describe the structure of DM halos as well as the NFW profile (Leubner 2005; Kronberger et al. 2006; Zavala et al. 2006). However, the study of Barnes et al. (2007) showed that though SP density profiles can match the NFW density profile on the radial range of simulated CDM halos, the velocity dispersion profiles are inconsistent with each other, evidencing the inability of nonextensive statistical mechanics to describe the structure of DM halos in the current form of the theory.

However, noticing some contradictions between previous studies, we decided to perform an independent investigation in order to figure out whether SPs predicted by nonextensive statistical mechanics can fit simulated CDM halos density profiles. Contrary to what was expected from previous studies, we found that SPs predicted by nonextensive statistical mechanics show a large discrepancy with simulated CDM halos in all their structural profiles, including the density profile. This clearly demonstrates that the theory is unable to predict the structure of DM halos.

2.3.1 Confusion in the literature

We will consider here the main contradiction appearing in the literature. It concerns how well SPs predicted by nonextensive statistical mechanics do match DM halo density

profiles. We find two categories of claims.

1. SPs match well the outer parts of the density profile of simulated CDM halos, and show a core in the central parts, in disagreement with simulations, but possibly in agreement with observations of galactic DM halos (Leubner 2005; Zavala et al. 2006).

2. SPs match the density profile of simulated CDM halos on the entire resolved radial range, that is, both in their inner and outer parts (Kronberger et al. 2006; Barnes et al. 2007).

Obviously, in the first case, the authors studied SPs with a core in the central parts, while in the second case, the authors studied SPs with a cusp instead. However, no mention is made in Kronberger et al. (2006) and Barnes et al. (2007) about the appearance of a cusp in the polytropic profile. Although it is possible to obtain cuspy SPs by choosing a nonzero density slope as boundary condition near the center, the central boundary conditions used in Kronberger et al. (2006) and Barnes et al. (2007) are not mentioned, and more importantly, there is no discussion about whether these solutions are physically relevant as predictions of DM halo structures.

2.3.2 Can SPs match an NFW profile: cored versus cuspy SPs

We will now present the characteristics of cored and cuspy SPs, and discuss their respective physical relevance.

Classical SPs

As mentioned previously, SPs first emerged from stellar studies (Chandrasekhar 1939). Stars can be described as a self-gravitating fluid in hydrostatic equilibrium. Combining the Poisson equation for the gravitational potential

$$\nabla^2\phi = 4\pi G\rho \tag{2.14}$$

to the equation of hydrostatic equilibrium

$$\frac{dp}{dr} = -\rho \frac{d\phi}{dr}, \tag{2.15}$$

and to the polytropic equation of state

$$p = K\rho^{\gamma} \tag{2.16}$$

which links the pressure p of a polytropic fluid to the density ρ via the adiabatic index γ and a constant K, leads to the Lane-Emden equation

$$\frac{1}{\xi^2}\,\frac{\mathrm{d}}{\mathrm{d}\xi}\left(\xi^2 \frac{\mathrm{d}\theta}{\mathrm{d}\xi}\right) + \theta^n = 0, \tag{2.17}$$

where ξ is the reduced radius

$$\xi = r\sqrt{\frac{4\pi G\rho_0}{(n+1)\sigma_0^2}}, \tag{2.18}$$

and θ is the reduced density

$$\theta = \left(\frac{\rho}{\rho_0}\right)^{1/n}. \tag{2.19}$$

SPs are the structures that are solution of the Lane-Emden equation. The free parameters are the central density ρ_0, the central velocity dispersion σ_0, and the polytropic index n. While ρ_0 and σ_0 are scaling parameters, the index n controls the shape of the profile.

Analytical solutions of the Lane-Emden equation exist only for $n = 0, 1, 5$. The other solutions are computed numerically by applying the natural boundary conditions $\rho = \rho_0$ and $d\rho/d\mathrm{r} = 0$ at the center. The asymptotic solution for $n \to \infty$ is the isothermal sphere (Binney & Tremaine 1987). The density profiles of SPs are presented in Fig. 2.1 in normalized units ($\rho_0 = \sigma_0 = G = 1$). We note that only SPs with $n < 5$ have a finite mass, while SPs with $n \geq 5$ have an infinite mass and a logarithmic density slope oscillating around -2, as for the isothermal sphere solution (Binney & Tremaine 1987; Medvedev & Rybicki 2001). For all values of n there is a central core.

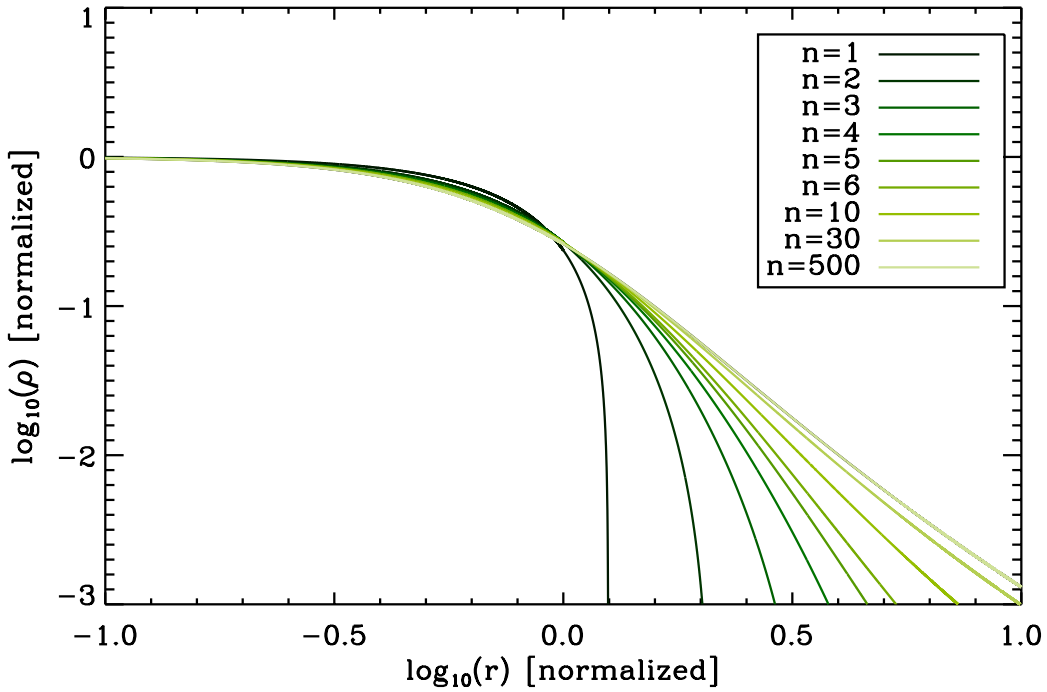

Figure 2.1: *Density profiles of stellar polytropes for values of the polytropic index n ranging from 2 to 500. The natural boundary conditions are used at the center: $\rho = \rho_0$ and $d\rho/dr = 0$ when $r \to 0$. The profiles are normalized to $\rho_0 = \sigma_0 = G = 1$.*

Cuspy SPs

Nonextensive statistical mechanics predicts SPs to describe the equilibrium state structures of DM halos, but does not specify the boundary conditions at the center, which are needed to numerically solve the Lane-Emden equation. Although the natural boundary conditions are often used (e.g., in Plastino & Plastino (1993) and Taruya & Sakagami (2003)), the introduction of a nonzero slope near the center is not excluded by the theory, and can create a central cusp in polytropic profiles.

In Kronberger et al. (2006) and Barnes et al. (2007), the authors fixed a non-zero logarithmic density slope near the center, chosen to match the NFW density profile[2]. They adopted a value of the polytropic index $n = 16.5$, found to fit the NFW model best

[2]E. I. Barnes, private communication; E. van Kampen, private communication for Kronberger et al. (2006).

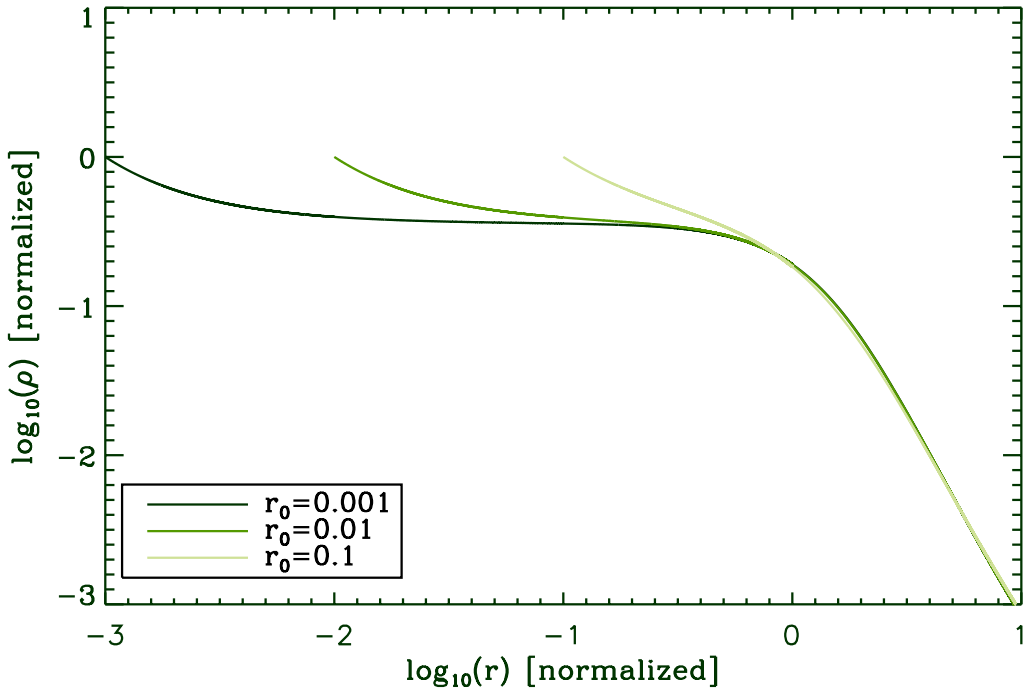

Figure 2.2: *Density profiles of stellar polytropes computed for* $n = 16.5$, *with* $\rho = \rho_0$ *and* $d\log_{10}(\rho)/d\log_{10}(\mathrm{r}) = -1$ *at the starting radius* r_0. *Profiles for different* r_0 *are presented. Only when starting the computation at* $r = 0.1$ *a cusp ressembling that of simulated DM halos appears. The profiles are normalized to* $\rho_0 = \sigma_0 = G = 1$.

(Kronberger et al. 2006; Barnes et al. 2007). We will use this value in the following for consistency with previous studies. The entire range of polytropic index n will be considered later in § 2.4.

A physically relevant logarithmic density slope to apply near the center of SPs is $\beta = d\log_{10}(\rho)/d\log_{10}(\mathrm{r}) = -1$, which is the asymptotic slope of the NFW profile toward the center. We illustrate in Fig. 2.2 how it is possible to obtain a cusp. We solve the Lane-Emden equation with the boundary conditions $\rho = \rho_0$ and $\beta = -1$, starting at radii $r = 0.001, 0.01, 0.1$. The fitting parameters ρ_0 and σ_0 are normalized to 1, and physical constants are expressed in natural units. We can notice in Fig. 2.2 that a cusp-halo profile appears only if fixing boundary conditions with a nonzero slope at a radius far from the center, that is, at $r = 0.1$ in Fig. 2.2. Otherwise, the core feature remains dominant.

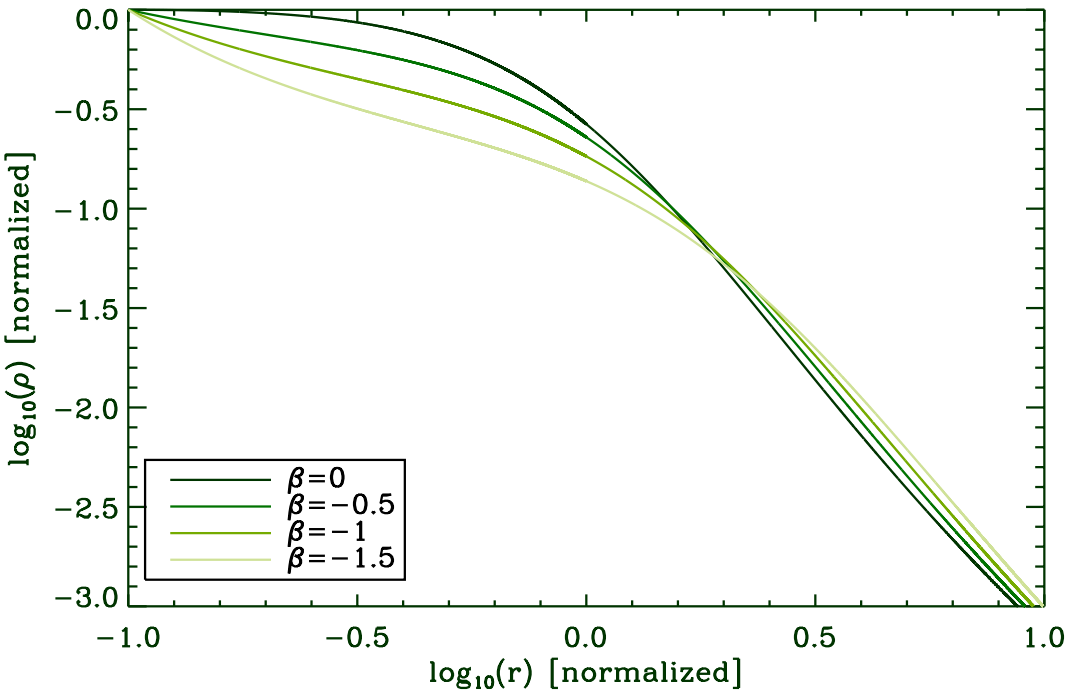

Figure 2.3: *Density profiles of stellar polytropes computed for* $n = 16.5$*, from a starting radius* $r = 0.1$*, with* $\rho = \rho_0$ *and varying the logarithmic density slope* $\beta = d\log_{10}(\rho)/d\log_{10}(\mathrm{r})$ *as initial condition. The profiles are normalized to* $\rho_0 = \sigma_0 = G = 1$*.*

We now solve the Lane-Emden equation starting at $r = 0.1$ and varying the initial logarithmic density slope (see Fig. 2.3). For values of $\beta = 0$ and -0.5, we observe a core in the central parts, while $\beta = -1$ leads to the cusp-halo structure distinctive of simulated CDM halos. On the other hand, a steeper initial slope such as $\beta = -1.5$ leads to an unlikely profile where the density slope is in turn steep, shallow and steep again. Therefore, we have seen that solutions of the Lane-Emden equation include cuspy SPs, if properly tuned. But this class of solutions is obtained by starting the numerical solution of the equation far from the origin. Consequently, it does not ensure physical boundary conditions at the center, and must be treated with caution from a physical point of view.

Let us now turn to the test of the central behaviour of the cuspy SP we obtained in Figs. 2.2 and 2.3. This would enable us to verify that it is a well-behaved solution all the way in, towards the center. To realize this, we developed a code which, given the values

of the density and density slope of a SP profile at a fixed radius, can solve the Lane-Emden equation inwards instead of outwards. Considering the cuspy SP we studied, with $n = 16.5$ and $\beta = -1$ fixed at $r = 0.1$, we can take the values of the density and density slope at, e.g., a radius $r = 10$, and compute the profile inwards until a radius $r = 0.001$ for instance. We already computed this profile from $r = 0.1$ to $r = 10$ (see Fig. 2.3), therefore we can check the consistency of the reverse computation within this radial range. We also checked the code's robustness on classical SPs and on analytical solutions of the Lane-Emden equation. Our result is presented in Fig. 2.4. The cuspy SP (light-green line) is compared to the classical SP (dark-green line) with the same parameters, for reference. The range between $r = 0.1$ and $r = 10$ is similar to that presented in Fig. 2.3, but when going further in, it appears that the cuspy polytrope has a density increase of more than 5 magnitudes, before falling down again. Such a structure is not stable. Therefore, this solution of the Lane-Emden equation can not be considered as representing the physical structure of astrophysical self-gravitating systems.

We will not investigate further the behaviour of cuspy SPs as it would require all a study in itself. But we demonstrated that it is very important to test the behaviour of such solutions to the Lane-Emden equation all the way to the center before using them as theoretical predictions.

2.3.3 Gravitational potential and density slope at the origin

The question of whether cuspy SPs can be considered as predictions from nonextensive statistical mechanics theory brings us to investigate what can be considered as physical conditions at the center of SPs. We will now turn to classical statistical mechanics, and study why only natural boundary conditions are considered in this formalism.

We find the answer in the works of S. Chandrasekhar and J. Binney. The solutions of the Lane-Emden equation with a finite density at the origin necessarily have a zero density slope at the origin (Chandrasekhar 1939). Moreover, a finite gravitational potential requires a finite density for SPs (Binney & Tremaine 1987). Therefore, only solutions with a zero

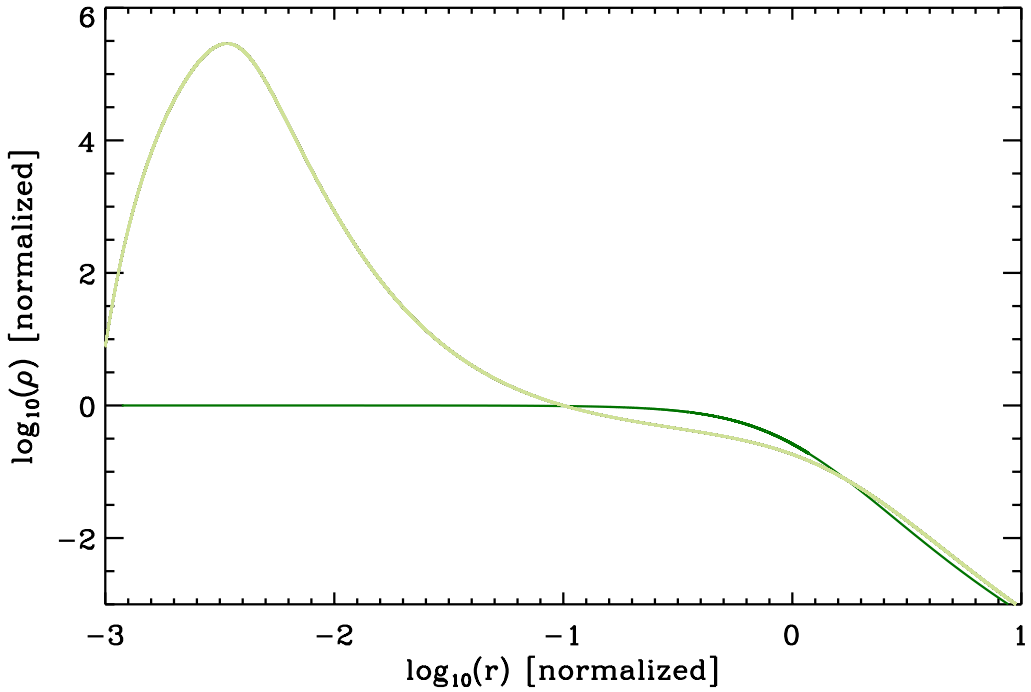

Figure 2.4: *Density profiles of classical and cuspy stellar polytropes for* $n = 16.5$. *Both profiles pass through the point* $\rho = \rho_0$ *at* $r = 0.1$, *but while the classical stellar polytrope has a logarithmic slope* $d\log_{10}(\rho)/d\log_{10}(\mathrm{r}) = 0$ *at that point (curve in dark green), the cuspy stellar polytrope has a logarithmic slope* $d\log_{10}(\rho)/d\log_{10}(\mathrm{r}) = -1$ *at that point (curve in light green). The behaviour of the profiles for* $r < 0.1$ *is computed by solving the Lane-Emden equation inwards. It reveals the divergent behaviour of this cuspy stellar polytrope in the central parts. The profiles are normalized to* $\rho_0 = \sigma_0 = G = 1$.

density slope at the origin have a finite gravitational potential at the origin. The details of the demonstration based on the two cited works can be found in Appendix B.

We would like to emphasize two things now:

1. An infinite gravitational potential at the center is not unphysical. Therefore, cuspy SPs might be physically relevant solutions of nonextensive statistical mechanics, provided that they show a well-behaved profile all the way to the center. On the other hand, the class of SPs with natural boundary conditions at the center exhibits by default a physical behaviour all the way to the center.

2. If we come back to the case of CDM halos that are of interest in this work, we can

say that simulated DM halos definitely have a finite gravitational potential at the center. Therefore, to establish a consistent comparison between theory and simulations, only SPs with a finite gravitational potential should be considered, that is, SPs with a zero slope at the origin. This conclusion will be used to restrict our study to classical SPs for the rest of this work.

2.3.4 Summary

In summary, classical SPs as used in Leubner (2005) and Zavala et al. (2006) guarantee on one hand physical conditions at the center and have a core which differs from simulated CDM halos but might be in agreement with observed DM halos. On the other hand, cuspy SPs used in Kronberger et al. (2006) and Barnes et al. (2007) match simulated CDM halos density profiles on both inner and outer parts, but they do not guaranty physical conditions at the center. While they are interesting in their own right as fitting profiles, it is necessary to test their central behaviour before considering them as physical predictions of nonextensive statistical mechanics.

Finally, predictions from nonextensive statistical mechanics for DM halos can be directly compared with simulated CDM halos, which are purely collisionless self-gravitating systems (on the contrary, the structure of observed DM halos may suffer effects from baryonic matter, and is not straightforward to compare with the theory). Simulated halos have by definition a finite gravitational potential at the center, and therefore a consistent comparison of simulations with predictions of nonextensive statistical mechanics must use solutions of the Lane-Emden equation with a finite gravitational potential at the center. Such solutions require a zero density slope at the center. Therefore, only classical SPs, and not cuspy SPs, provide a consistent comparison with simulated CDM halos.

We will not further consider cuspy SPs, but focus the study on the comparison between classical SPs and simulated CDM halos.

2.4 Comparison of SPs to simulated CDM halo radial profiles

In order to compare the predictions of nonextensive statistical mechanics to the results of N-body simulations, we compute radial profiles of fundamental quantities of astrophysical self-gravitating systems: the matter density $\rho(r)$, the logarithmic density slope $d\log_{10}(\rho)/d\log_{10}(\mathrm{r})$, the integrated mass $M(r)$, and the circular velocity $V_c(r)$ (see Fig. 2.5). As we have seen in § 2.3.2, SPs are solutions of the Lane-Emden equation (Binney & Tremaine 1987), depending on three free parameters: the polytropic index n, the central density ρ_0 and the central velocity dispersion σ_0. We will consider now only solutions with a zero density slope at the center (§ 2.3.4). The value of n (related to q) is an intrinsic property of each system, but has not been determined from first principles and is therefore a free parameter. SPs with $n > 3/2$ are stable due to Antonov's stability criterion, that is, $\mathrm{d}f(\epsilon)/\mathrm{d}\epsilon < 0$ (Binney & Tremaine 1987). Other values of n are unrealistic: $n = 3/2$ corresponds to a distribution function independent of ϵ, and $n < 3/2$ to a distribution function diverging at the escape energy $\epsilon = 0$. Therefore, we compute numerical solutions of the Lane-Emden equation for $n > 3/2$, choosing values of n ranging from 2 to ∞. We verified the consistency of our profiles using the analytical solutions of the Lane-Emden equation, as well as the isothermal sphere, which is the asymptotic solution when $n \to \infty$[3].

CDM structures in N-body simulations evolve from primordial fluctuations via hierarchical clustering to form halos of universal shape, well described by the NFW model (Navarro et al. 1996). These halos formed through accretion and mergers are sufficiently similar to those obtained by monolithic collapse, that is, isolated halos, so that we do not take into account in this study the influence of formation history and cosmological environment on the final state of simulated halos (Huss et al. 1999).

Collisionless systems have very long collisional relaxation timescales to reach the "true" equilibrium, but reaches a stable quasiequilibrium state faster (dynamical timescales are

[3]Analytical solutions exist only for $n = 0, 1, 5$. We approximate $n \to \infty$ by $n = 500$, as large values of n tend asymptotically towards the isothermal sphere.

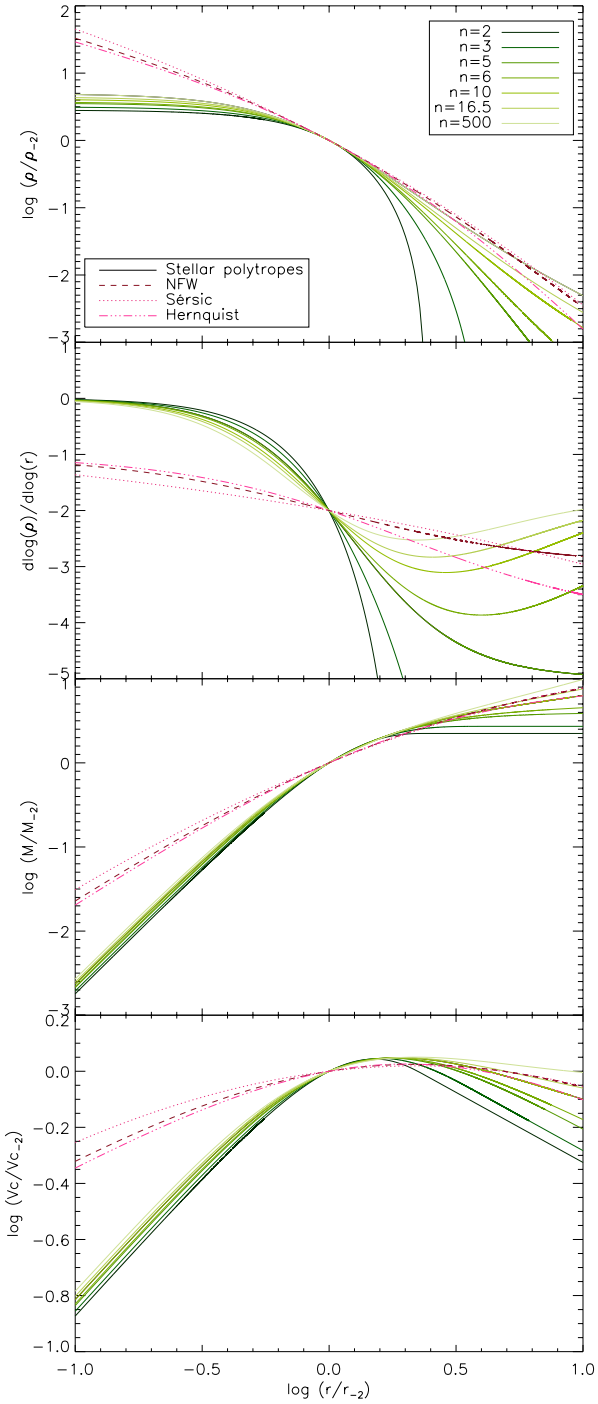

Figure 2.5: *From top to bottom are presented the radial profiles of the density, the logarithmic density slope, the integrated mass and the circular velocity. The profiles are scaled to* r_{-2}*, the radius at which the slope equals* -2*. Stellar polytropes predicted by nonextensive statistical mechanics are represented by the solid curves with the shades of green corresponding to different polytropic index* n *as indicated in the panel. Simulated dark-matter halos are represented by the NFW model (pink dashed curve), the 3D Sérsic model (pink dotted curve;* $\alpha = 0.17$*) and the Hernquist model (pink dash-dotted curve;* $a = 0.45$*).*

short compared to cosmological timescales, that is, the age of the universe) through the processes of violent relaxation and phase-mixing (Binney & Tremaine 1987). The quasiequilibria predicted by numerical cosmological simulations and by nonextensive statistical mechanics, respectively, may in either case be considered the most probable state the system reaches.

Many empirical models have been proposed as fitting the universal profile of CDM halos. We use in our study three of them to represent simulated halos. The NFW model is the more commonly used (Navarro et al. 1996). The Sérsic model has been proposed recently as fitting more accurately the inner part of high-resolution halos (Navarro et al. 2004; Graham et al. 2006). The Hernquist model provides a simple description of self-gravitating systems, for which all the profiles we use have analytical expressions (Hernquist 1990). As seen in Fig. 2.5, these three profiles form a group with similar shapes and we do not need to use actual simulations in our study.

To compare simulated CDM halos to SPs, we select the radial range for which recent N-body simulations are robustly resolved. Based on the high-resolution simulations published in Navarro et al. (2004), this corresponds to $0.1r_{-2} < r < 10r_{-2}$, where r_{-2} is the radius at which the logarithmic density slope equals -2. To compare SPs of all values of n with simulated halos, we need a scaling suitable for finite- and infinite-mass halos, circular velocity profiles with and without a maximum, and density profiles with very different steepness: r_{-2} provides such a universal scaling [4]. Moreover, it allows us to take equally into account the inner and outer parts of the halo, respectively defined as having a slope shallower and steeper than -2 (Navarro et al. 1996). Finally, our study is independent of scaling parameters: SP profiles are scaled depending on the choice of ρ_0 and σ_0, but the shape depends only on n. Therefore, scaling to r_{-2} makes identical any profiles of same n but different ρ_0 and σ_0, keeping only information about the shape. All the profiles we present, as scaled to r_{-2}, depend only on structural parameters: the range of n for SPs,

[4]The scaling radius r_{-2} is determined uniquely in the case of a monotonically decreasing slope. However, SPs of $n \geq 5$ have a logarithmic density slope oscillating around -2 (Medvedev & Rybicki 2001; Binney & Tremaine 1987); we therefore define r_{-2} as the smallest radius at which the slope is -2.

$\alpha = 0.17$ for the three-dimensional Sérsic profile (Navarro et al. 2004), $a = 0.45$ for the Hernquist profile (Hernquist 1990), and r_s for the NFW profile [5]. In Fig. 2.5 we compare SPs with simulated CDM halos, scaling to r_{-2}.

In the outer parts, where $r > r_{-2}$, SPs have very different shapes depending on the polytropic index n. Profiles with $n < 5$ correspond to finite-mass halos, while $n \geq 5$ polytropes have infinite mass, tending to the isothermal sphere when $n \to \infty$. While finite-mass polytropes may appear more attractive from a physical point of view, they also provide worse fits to simulated CDM halos, with an outer slope as steep as $d\log_{10}(\rho)/d\log_{10}(r) < -5$ at $10r_{-2}$. For infinite-mass SPs with larger values of the polytropic index, $n = 16.5$ (as found in Kronberger et al. (2006)) agrees with NFW and Sérsic models, while $n = 10$ agrees with the Hernquist model. Therefore, *some infinite-mass SPs can provide a good description of the outer parts of simulated halos.*

In the inner parts, where $r < r_{-2}$, SPs share a similar property: they have a large core, the shape and the extent of which depend little on the value of n. This feature is in striking disagreement with the predictions of N-body simulations, which show steeper inner slopes. While this core structure itself has been advanced as an advantage of SPs over the NFW profile (Zavala et al. 2006), solving the well-known cusp-core problem between simulations and observations (Gentile et al. 2004), it appears in Fig. 2.5 that this is not the case: the difference between SPs and simulated halos in the density, density slope and mass profiles is as high as one order of magnitude at $0.1r_{-2}$. Therefore, *for any polytropic index n, SPs do not properly describe the inner parts of simulated halos.*

[5] In the NFW model, the scale radius r_s is equal to r_{-2}.

2.5 Discussion

We have established here that the predictions of nonextensive statistical mechanics are not corroborated by simulations of CDM halos. Our results are based on readily observable quantities, that is, the matter density itself, and profiles derived from it. These findings are in direct contrast to previous works which found reasonable agreement because they either considered only the outer parts of simulated halos (Leubner 2005), used a nonzero density slope as initial condition near the center (Kronberger et al. 2006), or used values of $n < 5$ that lead to too steep density profiles in the outer parts (Zavala et al. 2006). Support for our conclusions, however, comes from Barnes et al. (2007) who, even though fixing a nonzero density slope near the center to match the NFW density profile, found inconsistency between SP and CDM halo velocity dispersion profiles. While we are cautious about the physical relevance of such profiles, it is of interest to emphasize that neither cored nor cuspy polytropes can describe properly simulated CDM halos.

These results imply a fundamental difference in the matter distribution of astrophysical self-gravitating systems predicted by nonextensive statistical mechanics and by N-body simulations. Such a discrepancy raises three main questions. 1) Is our comparison with simulated CDM halos valid? 2) Is nonextensive statistical mechanics the proper theory to describe collisionless long-range interaction systems at equilibrium? And 3) how does this study relate to observed DM halos? We briefly address these issues below.

1a. We study idealized systems which do not take into account complex effects in DM halos such as velocity anisotropy (Hansen & Moore 2006) or triaxiality (Hayashi et al. 2007). However, the error we make by using isotropic and spherically averaged models to represent DM halos is small compared to the discrepancy we find between SPs and simulated halos. Moreover, we do not address here general problems of statistical mechanics of self-gravitating systems like, e.g., infinite mass (Hjorth & Madsen 1991), so as to focus on the issues specific to nonextensive statistical mechanics.

1b. N-body simulations depend on various parameters, such as the choice of the softening length and the number of particles, which can introduce numerical effects in the

resulting halos. The softening of the gravitational force on a small scale, introduced to avoid two-body interactions, creates a core at the center of the halo, approximately the size of the softening length. The number of particles fixes the maximum phase-space density resolved at redshift zero, and if not large enough, a core appears due to the lack of particles in the center. Both effects lead to a shallower density profile in the center of halos if the simulation is of low resolution (Moore et al. 1998). Therefore, the discrepancy we observe between simulated profiles and SPs is genuine and increases with the resolution of numerical simulations.

1c. We compare theoretical statistical predictions to cosmological simulations, but the latter depend on initial conditions and cosmological parameters. Initial conditions are fixed by the shape of the power spectrum of initial fluctuations $P(k) \propto k^{n_s}$, that is, by the choice of the spectral index n_s. From CMB observations, we have an indication that $n_s = 0.960 \pm 0.014$ (Komatsu et al. 2008), but tests on cosmological simulations proved that they depend very little on the choice of n_s and on the cosmological model used (Navarro et al. 1997). Therefore, the universal profiles of simulated halos can be compared to statistical theories as a general prediction.

1d. The choice of a scaling is necessary to compare DM halo models, but can bring a visualization bias. We checked if the use of r_{-2} leads us to overestimate the disagreement between nonextensive statistical mechanics and N-body simulations. However, adjusting the fit in the outer parts of the halo, that is, scaling to the virial radius, increases even more the discrepancy in the inner parts, while scaling profiles to fit well at smaller radii makes the discrepancy appear in the outer parts of the halo.

2. Nonextensive statistical mechanics relies on three assumptions: *a)* the generalized entropy S_q is the right form to describe long-range interaction systems, *b)* the system is at equilibrium, and its most probable state is given by the maximum entropy principle, and *c)* S_q is maximized at fixed energy, leading to a system whose distribution function depends only on the energy per unit mass, and has isotropic velocity dispersion. Though simulated halos show evidence of velocity anisotropy, the relation between density slope and velocity anisotropy (Hansen & Moore 2006) shows that it is isotropic in the center, where

violent relaxation (Lynden-Bell 1967) (the process by which strong potential fluctuations efficiently drives the system towards equilibrium) is most effective. Therefore, assumptions *b)* and *c)* hold true in the center. However, it is in the inner parts that the disagreement between SPs and simulated halos is the strongest. Hence, we suggest that the assumption *a)*, that is, the choice of the generalized entropy S_q motivated by nonextensive statistical mechanics, cannot be used to predict the equilibrium structures of simulated CDM halos.

3. Simulated CDM halos are in good agreement with observations of nearby galaxy clusters (Pointecouteau et al. 2005), but discrepancies appear at galactic scale, among others, the inner core found from spiral galaxy rotation curves (Gentile et al. 2004). SPs, interestingly, have an inner core too, but the discrepancy we observe between SPs and simulated CDM halos is too large to explain the core of observed DM halos. Adding adiabatic contraction in simulations results in CDM halos with steeper inner parts, which would not change our conclusions.

2.6 Conclusion

The study presented in this chapter was motivated by testing a possible theoretical prediction for the structure of DM halos. Eventually, it established that nonextensive statistical mechanics (Tsallis 1988; Plastino & Plastino 1993; Taruya & Sakagami 2003), a theory generalizing classical statistical mechanics and thermodynamics, does not describe the equilibrium state of astrophysical self-gravitating systems, as represented by CDM halos formed in N-body simulations.

On one hand, that conclusion indicates that the theory (in its simplest form) applied to astrophysical self-gravitating systems might need revision. More insights into the physical meaning of nonextensive statistical mechanics, and particularly of the index q, is of critical importance.

On the other hand, from an astrophysical point of view, nonextensive statistical mechanics can not provide a theoretical prediction for the equilibrium structures of DM halos, as was hoped for. Finding a theoretical description of DM halo structures derived from first principles remains an open question.

Most of this chapter is to be published as: C. Féron, J. Hjorth, J. P. McKean and J. Samsing (2008) – *"A search for disk-galaxy lenses in the Sloan Digital Sky Survey"*, submitted to The Astrophysical Journal, `http://arXiv.org/abs/0810.0780`.

Chapter 3

Finding disk-galaxy lenses in the SDSS: toward measuring the M/L ratio of disk galaxies

Abstract

Gravitational lensing provides a promising way of constraining the mass distribution of disk galaxies and measuring their mass-to-light (M/L) ratio. These are key components for comparing the mass of disks grown in cosmological simulations to the luminosity of observed galaxies. The first automated spectroscopic search for disk-galaxy lenses is presented here, using the Sloan Digital Sky Survey database. Eight disk-galaxy gravitational lens candidates are studied, using a combination of ground-based imaging and long-slit spectroscopy.

3.1 Introduction

In this chapter is treated one aspect of the TF relation zero point problem (§ 1.2.2). Some recent studies indicate that part if not all of the problem might come from the generalization of Galactic stellar population properties to other disk galaxies, and renew the importance of measuring the M/L[1] ratio of disk galaxies. Such measurements would not only bring insights into the TF relation zero point problem, but also improve our knowledge of physical processes in and structure of disk galaxies, by adding valuable constraints to

[1]The M/L ratios are expressed in solar units throughout this study.

stellar population models. The study presented in this chapter is the first automated search for disk-galaxy lenses (that is, gravitational lenses where the lensing mass is a disk galaxy), opening new perspectives for measuring the M/L ratio of disk galaxies.

3.1.1 A possible source of the TF relation zero point problem

It is still unclear whether the TF relation zero point problem (§ 1.2.2) originates in the simulations (Dutton et al. 2007), in the ΛCDM cosmology (van den Bosch et al. 2003), or in the generalization of the Milky Way (MW) initial mass function (IMF) to other disk galaxies (Flynn et al. 2006). The IMF describes the mass spectrum of stars in galaxies. Combined to the star formation history (SFH) which accounts for the evolution of the number of stars with time in a galaxy, it allows to compute stellar population models, and therefore the stellar population present in a galaxy at a given time, as well as its mass and luminosity, among other physical values. The MW is used as a reference to describe the stellar population of distant galaxies. However, recent studies found the MW to be offset from the observed TF relation by about the same amount as disk-galaxies simulated using Solar Neighborhood IMFs (Flynn et al. 2006; Portinari & Sommer-Larsen 2007, and Fig. 1.3 in § 1.2.2). This suggests that simulations may be consistent with the model they reproduce, but the Galactic IMF may not be representative of all disk galaxies. Unfortunately, the IMF can be directly measured only from stars in the Solar Neighborhood, and therefore the different models proposed to describe the IMF are all based on the example of our Galaxy (see Portinari et al. (2004) for a review of IMFs).

The M/L ratio of disk galaxies can be used to constrain the shape of the IMF (de Jong & Bell 2007). The M/L ratio of disk galaxies is sensitive to the SFH, observed as an evolution of the M/L ratio with Hubble type and color, and to the shape of the IMF. Indeed, the stars at the low-mass end of the IMF contribute significantly to the mass of the galaxy disk, but not to its luminosity. Hence, a bottom-light IMF yields a low M/L ratio. Considering the TF zero point problem, adopting a more bottom-light IMF than the Solar Neighborhood IMF to simulate disk galaxies would shift the zero point of the

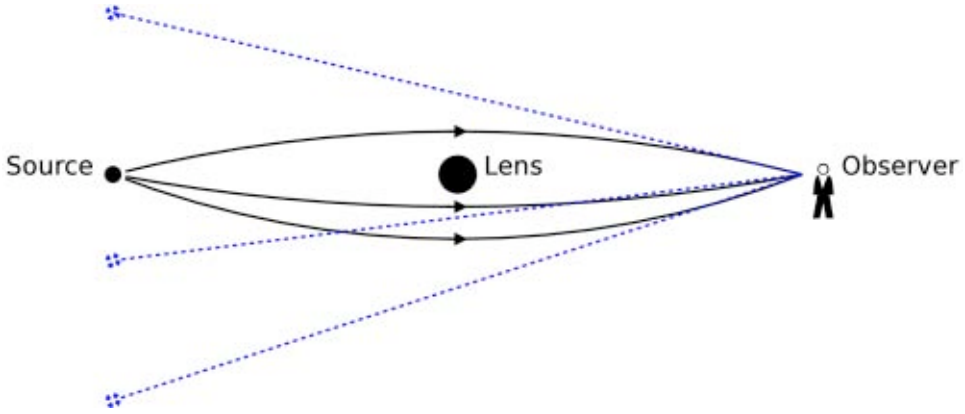

Figure 3.1: *Deflection of a source light rays by a lensing galaxy along the observer line-of-sight.*

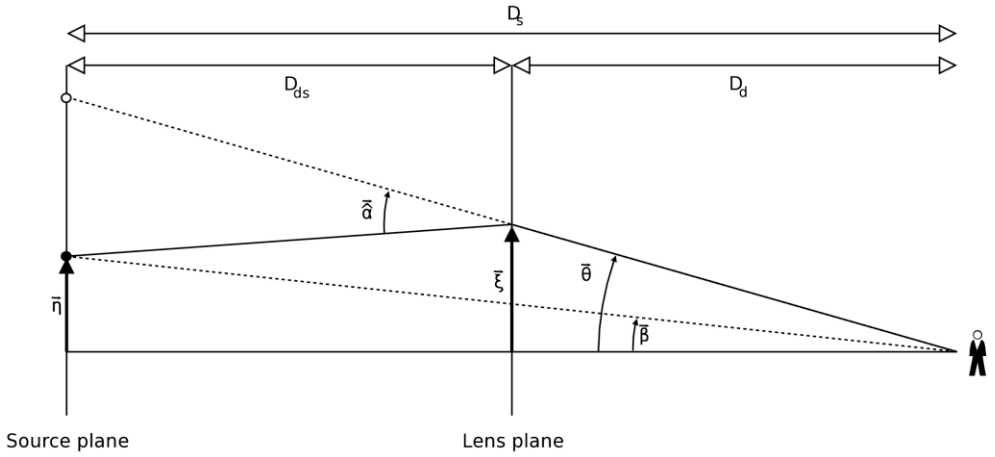

Figure 3.2: *Lensing geometry.*

simulated TF relation toward lower masses (or higher luminosities), in agreement with the observed TF relation.

Yet, to date, detailed individual measurements of M/L ratios exist for three disk galaxies only. These being the MW (Flynn et al. (2006), $M_*/L_I = 1.20$ for the stellar matter in the Galactic disk), the Sc galaxy NGC 4414 (Vallejo et al. (2002), $M_*/L_I \sim 1$), and the Sab spiral lens 2237+0305, i.e., the Einstein Cross (Trott & Webster (2002), $M_*/L_I = 1.1$ for the disk). There are several methods used to determine indirectly the M/L ratio of disk galaxies, for example, stellar population models (assuming the shape of the IMF), and relations between the color and M/L ratio derived from the maximum rotation curves of spiral galaxies (Bell & de Jong 2001; Salucci et al. 2008).

3.1.2 Measuring M/L ratios with gravitational lensing

When a galaxy lies close to the line of sight to a distant object, such as a quasar or a higher redshift galaxy, the path of the light from the distant source is bent by the galaxy's gravitational field, producing magnified, multiple images of the distant source. This effect is known as gravitational lensing, and allow not only to study distant objects that are lensed, but also the mass distribution of the lensing galaxy, which is what we are interested in for this study.

We will take the occasion now to introduce some concepts of gravitational lensing which will be used later in this chapter. The deflection of light rays by a galaxy gravitational field (Fig. 3.1) can be, if the deflection angle is small, schematized by a simple geometry (Fig. 3.2). The deflection angle $\hat{\alpha}$ is related to the angular position of the source as seen by the observer β, and the actual position of the source θ, by the lens equation

$$\beta = \theta - \frac{D_{ds}}{D_s}\hat{\alpha}(\theta). \tag{3.1}$$

The angular diameter distances between the observer and the deflector D_d, between the observer and the source D_s, and between the deflector and the source D_{ds}, are functions of the cosmology and the redshifts of the respective objects (Hogg 1999).

If the deflector is considered as a point mass M, and the observer, the lens and the source are perfectly aligned, the lens equation becomes

$$\theta = \frac{D_{ds}}{D_d D_s}\frac{4GM}{c^2\theta}, \tag{3.2}$$

that is,

$$\theta_E = \sqrt{\frac{D_{ds}}{D_d D_s}\frac{4GM}{c^2}}. \tag{3.3}$$

The light from the source is seen by the observer as a ring around the lens galaxy, of angular radius θ_E. The phenomenon is called an Einstein ring, with θ_E the Einstein radius.

It is then straightforward to compute the mass within the Einstein radius:

$$M = \frac{\theta_E^2 c^2}{4G} \frac{D_d D_s}{D_{ds}}. \tag{3.4}$$

This provides a useful simplified model to estimate the mass of a lens galaxy within the Einstein radius. It will be used in § 3.4 to estimate the M/L ratio of the new gravitational lenses which are presented in this work.

Coming back now to the study of disk galaxies, gravitational lensing can provide an independent measurement of the M/L ratio of their disk and bulge. The lensing geometry is sensitive to the total mass enclosed within the Einstein radius, and to the total projected ellipticity, giving information on the combination of the bulge, disk and DM halo. However, a disk-halo degeneracy remains due to the lack of constraints on the halo ellipticity. The study of the spiral lens B1600+434 (Jaunsen & Hjorth 1997) by Maller et al. (2000) proved the feasibility of breaking this degeneracy assuming an independent mass measurement which would constrain the disk and halo contributions at larger radii. Following this method, Trott & Webster (2002) studied the Einstein Cross (Huchra et al. 1985) and measured the bulge and disk M/L ratios of the spiral lens, using two H I rotation points in addition to the lensing constraints. These two studies found evidence for a sub-maximum disk[2], in contradiction with rotation curve studies (Salucci & Persic 1999).

Unfortunately, only seven confirmed disk-galaxy lenses are known to date (see Table 3.1). In comparison, about a hundred elliptical-galaxy lenses were already known[3] before the large surveys of recent years (Bolton et al. 2008; Faure et al. 2008). This difference is due in part to the fact that disk galaxies are less massive than elliptical galaxies, and so have a lower multiple image cross-section. Theoretical models predict that only 10% to 20% of lenses are due to spiral galaxies (Keeton & Kochanek 1998; Möller et al. 2007). Moreover, their detection by optical imaging can be made more challenging due to the small separation of the lensed images and by dust extinction in the disk.

[2]The theoretical study of Shin & Evans (2007) also points towards spiral lens galaxies having sub-maximum disks.

[3]CASTLES, `http://cfa-www.harvard.edu/castles/`

Table 3.1. *Disk galaxy lenses*

Name	N[a]	$z_{\rm lens}$	$z_{\rm source}$	$r_{\rm Einstein}$[b]	disk M/L	Comments	ref
B0218+357	2	0.685	0.944	0.17	···	Too crowded by the quasar images	1, 2
B1600+434	2	0.41	1.59	0.70	···	···	3, 4, 5
CXOCY J2201-3201	2	0.32	3.90	0.41	$M_*/L_V = 4$	One [O II] rotation point	6
OAC-GL J1223-1239	2	0.4656	unknown	0.42	···	···	7
PKS 1830-211	2	0.886	2.507	0.491	···	System near to galactic plane	8
PMN J2004-1349	2	unknown	unknown	0.56	···	···	9
Q2237+0305	4	0.0394	1.695	0.9	$M_*/L_I = 1.1$	Two H I rotation points	10, 11

[a]Number of lensed images.

[b] In arcsec.

References. — (1) Patnaik et al. (1992); (2) York et al. (2005); (3) Jaunsen & Hjorth (1997); (4) Koopmans et al. (1998); (5) Maller et al. (2000); (6) Castander et al. (2006); (7) Covone et al. (2008); (8) Winn et al. (2002); (9) Winn et al. (2003); (10) Huchra et al. (1985); (11) Trott & Webster (2002)

Fortunately, spectroscopic selection of candidates opens new perspectives for finding disk-galaxy lens systems. The Sloan Lens Advanced Camera for Surveys (SLACS) project has pioneered this new technique to discover strong gravitational lenses (Bolton et al. 2004, 2006), using the large spectroscopic database of the Sloan Digital Sky Survey (SDSS; York et al. 2000). They selected luminous red galaxies with absorption-line dominated spectra that also showed at least three emission lines from a background galaxy along the line-of-sight. Imaging with the *Hubble Space Telescope* (*HST*) has confirmed over 70 new gravitational lenses[4], with a survey efficiency over 65 %. All of the confirmed systems had measured lens and source redshifts, which is required for determining the mass of the lens (Bolton et al. 2008). The Optimal Line-of-Sight (OLS) lens survey (Willis et al. 2005, 2006) extended the search to those lens candidates showing only one emission line from a background galaxy. This allowed lensed galaxies at higher redshifts to be investigated. They found seven new early-type gravitational lenses from the SDSS, which they confirmed using a combination of ground-based imaging and spectroscopic observations.

Spectroscopic selection can also be used to efficiently find disk-galaxy lenses in the SDSS. However, the foreground galaxy as well as the background galaxy can have strong

[4]We note that the full SLACS sample of confirmed lenses presented in Bolton et al. (2008) contains six systems classified as late-type (Sa or later).

emission lines, making the search more difficult. Also, the small number of disk-galaxies discovered to date indicates that this project can be challenging. Yet, here we show that it is feasible.

In addition, galaxy-galaxy lenses bring better constraints than lensed quasars on the mass distribution of the lens galaxy. The lensed images are typically extended, containing much more information than point sources, and they are faint, allowing accurate photometry and astrometry of the disk galaxy to be carried out. Moreover, the low redshift of $z \sim 0.1$ for SDSS galaxies is favorable for adding rotation curve measurements to the lensing constraints in the future.

The purpose of this work is to prove the feasibility of efficiently discovering disk-galaxy lenses by an automated spectroscopic search, using the large spectroscopic database of the SDSS. This is not a statistical study. We present a method to find low redshift galaxy-galaxy lenses where the lens galaxy is a disk, these systems being particularly well suited for measuring the M/L ratios of disk galaxies and the mass distribution in their central parts.

We assume a ΛCDM cosmology throughout the study with the following cosmological parameter values: $\Omega_m = 0.3$, $\Omega_\Lambda = 0.7$, $H_0 = 70$ km s^{-1} Mpc^{-1}. In this cosmology, $1''$ corresponds to 1.84 kpc at a redshift $z = 0.1$.

3.2 Lens candidates selection

3.2.1 Massive disk galaxies in the SDSS

The SDSS provides a large optical imaging and spectroscopic database of astronomical objects, covering more than a quarter of the sky (York et al. 2000). Defining proper selection criteria to constitute a sample of massive disk galaxies out of the SDSS database is not trivial. Disk galaxies have very diverse spectral types, ranging from the absorption dominated spectra of S0 and Sa galaxies to the emission line spectra of Sb and Sc galaxies. However, it is possible to identify disk galaxies using color criteria. The study of Strateva et al. (2001) shows that galaxies in the SDSS are distributed in two groups divided by the color separator $u - r = 2.22$ around redshift $z = 0.1$, with a redshift evolution roughly parallel to the separator line. For each population, the peak density corresponds to elliptical and spiral galaxies, respectively. This provides a good criterion to select a sample of spiral galaxies in the SDSS. However, because gravitational lensing depends highly on the mass of the lensing galaxy, and spiral galaxies are on average less massive than elliptical galaxies, we want to find massive disk galaxies to increase the probability that the background galaxies will be multiply imaged. That is, try to select preferentially S0 and Sa galaxies, which are more massive than Sb and Sc galaxies.

The study of Fukugita et al. (1995) gives more constraints on the color of different galaxy types in the SDSS passband system. Tables are available for various galaxy redshifts ($z = 0.0, 0.2, 0.5, 0.8$); we use the $z = 0.2$ galaxy color values, as we impose on our sample the redshift range $0.1 < z < 0.3$. The upper redshift limit is fixed by the redshift selection in the Main Galaxy Sample of the SDSS (Percival et al. 2007). The lower redshift limit is chosen to increase the efficiency of our survey. Indeed, about half of the SDSS Main Galaxy Sample lies below $z = 0.1$, but these galaxies have a lower probability of being gravitational lenses due to their low redshift. We compare the color values from Fukugita et al. (1995) to the color distribution of SDSS galaxies found by Strateva et al. (2001, see their Fig. 1). The color of galaxies at $z = 0.2$ calculated in the SDSS passband system by Fukugita et al.

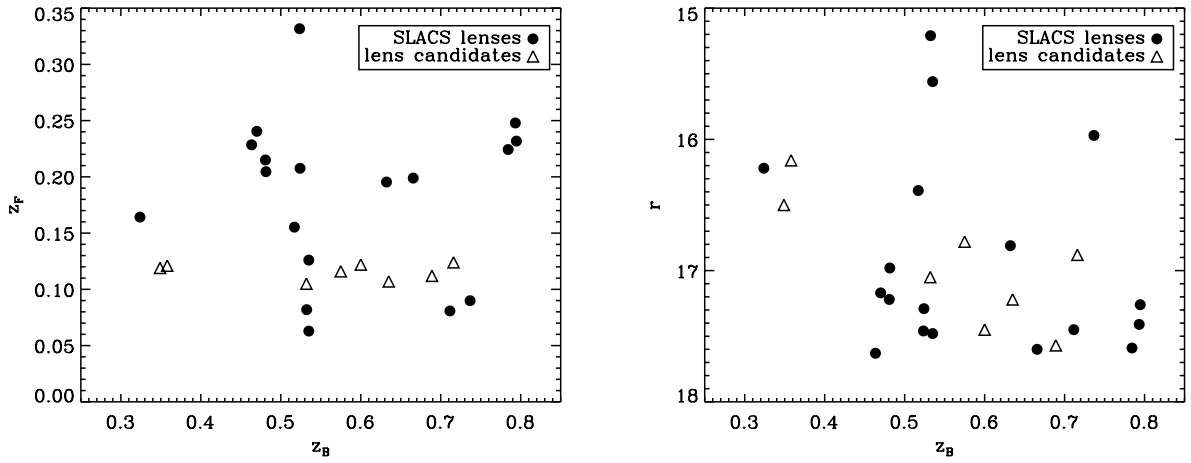

Figure 3.3: *Distribution of the foreground galaxy redshift z_F, the background galaxy redshift z_B and the r magnitude of our lens candidates compared to the SLACS strong lenses from Bolton et al. (2006) (the larger sample of SLACS strong lenses published in Bolton et al. (2008) was not available at the time we did the selection of our lens candidates).*

(1995) have a higher (redder) $u - g$ when compared to those galaxies actually observed by the SDSS in the same passband system (Strateva et al. 2001). Therefore, we use the color of Sab and Sbc galaxies at $z = 0.2$ from Fukugita et al. (1995), which cover part of the region of color-space situated between the density peaks for the elliptical and spiral galaxy populations in the SDSS (Strateva et al. 2001). This is where we expect to find the most massive disk galaxies in color-space.

This leads us to define a color selection criterion[5] $1.4 < u - g < 2$ and $0.7 < g - r < 1$, in addition to the $r < 17.7$ selection intrinsic to the SDSS Main Galaxy Sample. We find a sample of 41625 candidate massive disk galaxies, using the SDSS Fifth Data Release (Adelman-McCarthy et al. 2007). Being based only on color, this selection will include some elliptical galaxies. Visual inspection and galaxy modeling will be necessary to identify the disk galaxies among the gravitational lens candidates.

[5]We used a combination of $u - g$ and $g - r$ color rather than $u - r$ color in order to match the search criteria available in the SDSS SkyServer Spectroscopic Query Form, which we used to retrieve and download our sample of galaxies.

3.2.2 Spectroscopic selection

The selection of lens candidates among our sample of massive disk galaxies is two-stepped. First, we select spectra presenting evidence for at least three emission lines from a background galaxy. Second, we filter these candidates based on redshift and magnitude criteria to keep only those candidates with the highest lensing probabilities.

We developed an automated method to select the spectra presenting evidence of at least three emission lines from a background galaxy. Knowing the redshift of the foreground galaxy from the SDSS database, we can flag the emission lines belonging to the foreground galaxy as well as skylines, and find the remaining emission lines. We select as lens candidates those spectra showing at least three emission lines among [O II] $\lambda\lambda$3727, Hβ 4861, [O III] 4959, [O III] 5007 and Hα 6563, that belong to a higher redshift galaxy.

In this pilot study, we looked only for bright lenses, that is, candidates we can easily follow-up with ground-based observations. Therefore, we decided to use a signal-to-noise (S/N) ratio per pixel selection to find emission lines, which is directly obtained from the ratio of the SDSS flux and noise spectra. This method is sufficient to detect bright emission lines, and saves the computation time that an integrated S/N selection would require. The limits we used for the S/N ratio per pixel were, $S/N > 5$ for the first emission line peak and then $S/N > 3$ for the other emission line peaks (that were at the same redshift as the first emission line peak). This first step of the selection results in 20 spectra presenting a higher redshift galaxy aligned along the line-of-sight.

We apply a second selection based on lensing probability: systems with a large strong lensing cross-section will have a higher probability for the background galaxy to be multiply imaged, and not only magnified. Studies of gravitational lens systems have found that isothermal mass models are a good approximation for the lensing mass distribution (Koopmans et al. 2006). For a singular isothermal sphere model, the strong lensing cross-section is $\sigma_{SL} = \pi\ \theta_E^2$ with $\theta_E = 4\ \pi\ (\sigma^2/c^2)\ (D_{LS}/D_S)$, where θ_E is the Einstein radius, σ is the velocity dispersion of the lens galaxy, D_{LS} is the angular diameter distance between the lens and the source, which depends on the lens redshift, the source redshift

Table 3.2. *Lens candidates*

Name	R.A. (J2000)	Decl. (J2000)	Plate-MJD-Fiber	z_F	z_B	r
J0812+5436	08 12 13.30	+54 36 50.9	spSpec-53384-1871-114	0.121	0.358	16.16
J0903+5448	09 03 15.62	+54 48 56.4	spSpec-51908-0450-226	0.112	0.689	17.57
J0942+6111	09 42 49.08	+61 11 15.5	spSpec-51910-0486-155	0.124	0.716	16.88
J1150+1202	11 50 19.56	+12 02 57.3	spSpec-53142-1609-141	0.105	0.532	17.05
J1200+4014	12 00 46.90	+40 14 00.0	spSpec-53401-1976-183	0.116	0.575	16.78
J1356+5615	13 56 16.53	+56 15 06.1	spSpec-52797-1323-531	0.122	0.600	17.45
J1455+5304	14 55 43.55	+53 04 41.2	spSpec-52674-1164-270	0.107	0.635	17.22
J1625+2818	16 25 51.95	+28 18 21.4	spSpec-52822-1408-417	0.119	0.349	16.50

and the cosmological parameters, and D_S is the source angular diameter distance. The lensing cross-section increases as a function of the lens galaxy mass and of the lens-source angular diameter distance, that is, of the redshift interval between the lens and the source. Unfortunately, we do not have measurements of σ, which provides a prior on the mass for the candidate galaxies in our sample. Instead, we use the observed r-band magnitude from the SDSS database to obtain a rough estimate of the old stellar population luminosity and hence the mass of each galaxy, that is, the most massive galaxies are those with the lowest r magnitudes.

We select a final sample of eight gravitational lens candidates as those systems with the same range in r magnitude, foreground galaxy redshift z_F and background galaxy redshift z_B as the confirmed SLACS lenses (see Fig. 3.3). The final sample has the following characteristics. All of the lens candidates have $z_F \sim 0.1$. The background galaxy redshifts are distributed in two subsamples. The first in a group at $0.5 < z_B < 0.8$ with $16.7 < r < 17.7$, and the second in a group of two lens candidates with specially low background galaxy redshifts at $0.3 < z_B < 0.4$, but more massive lens galaxies with $16 < r < 16.7$. The list of final lens candidates with redshift and r magnitude information is presented in Table 3.2. The full SDSS spectra of the lens candidates are presented in Fig. 3.4, and the detected background emission lines are shown in Fig. 3.5.

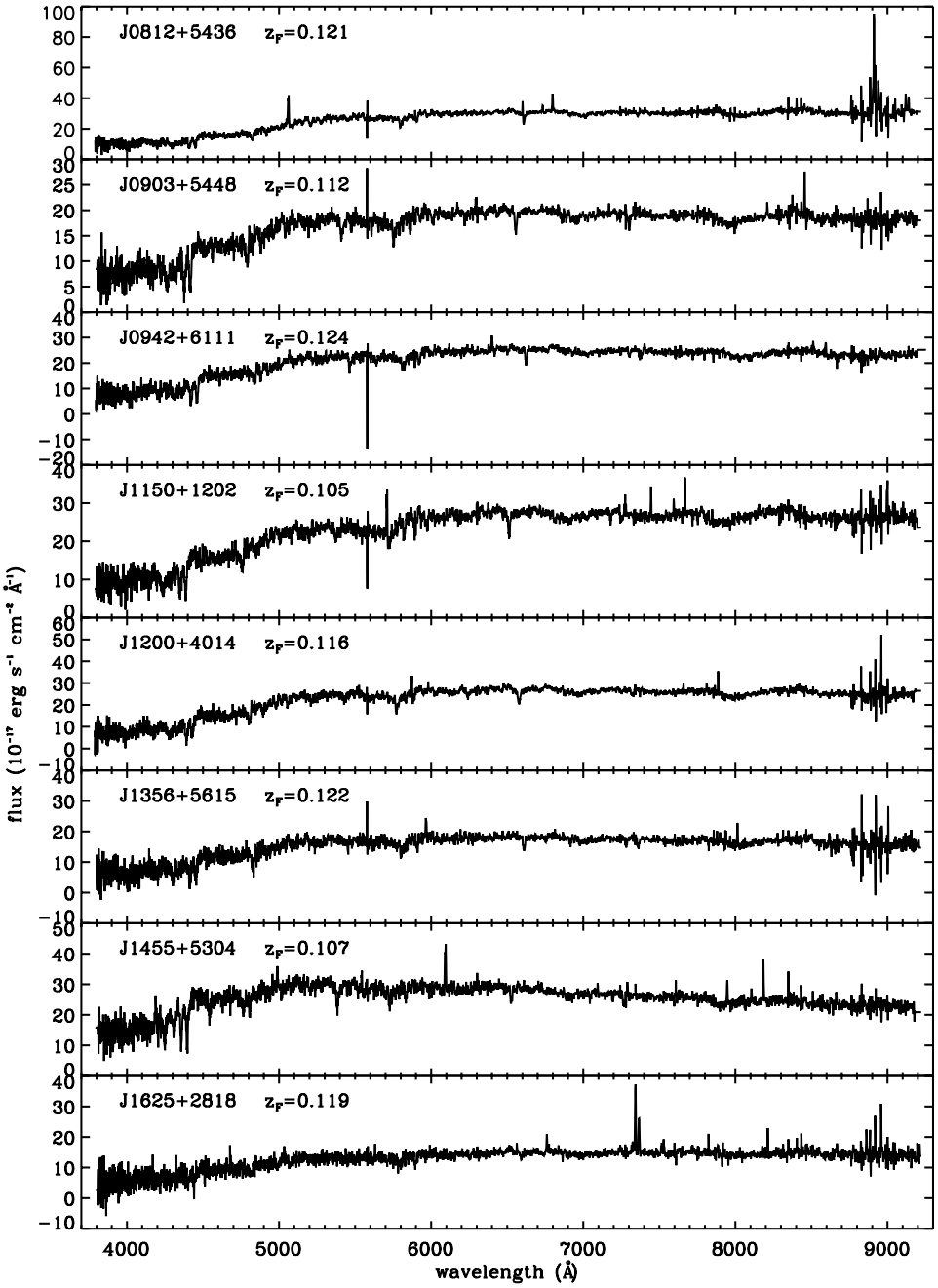

Figure 3.4: *Full SDSS spectra of the selected gravitational lens candidates (from Princeton/MIT SDSS Spectroscopy).*

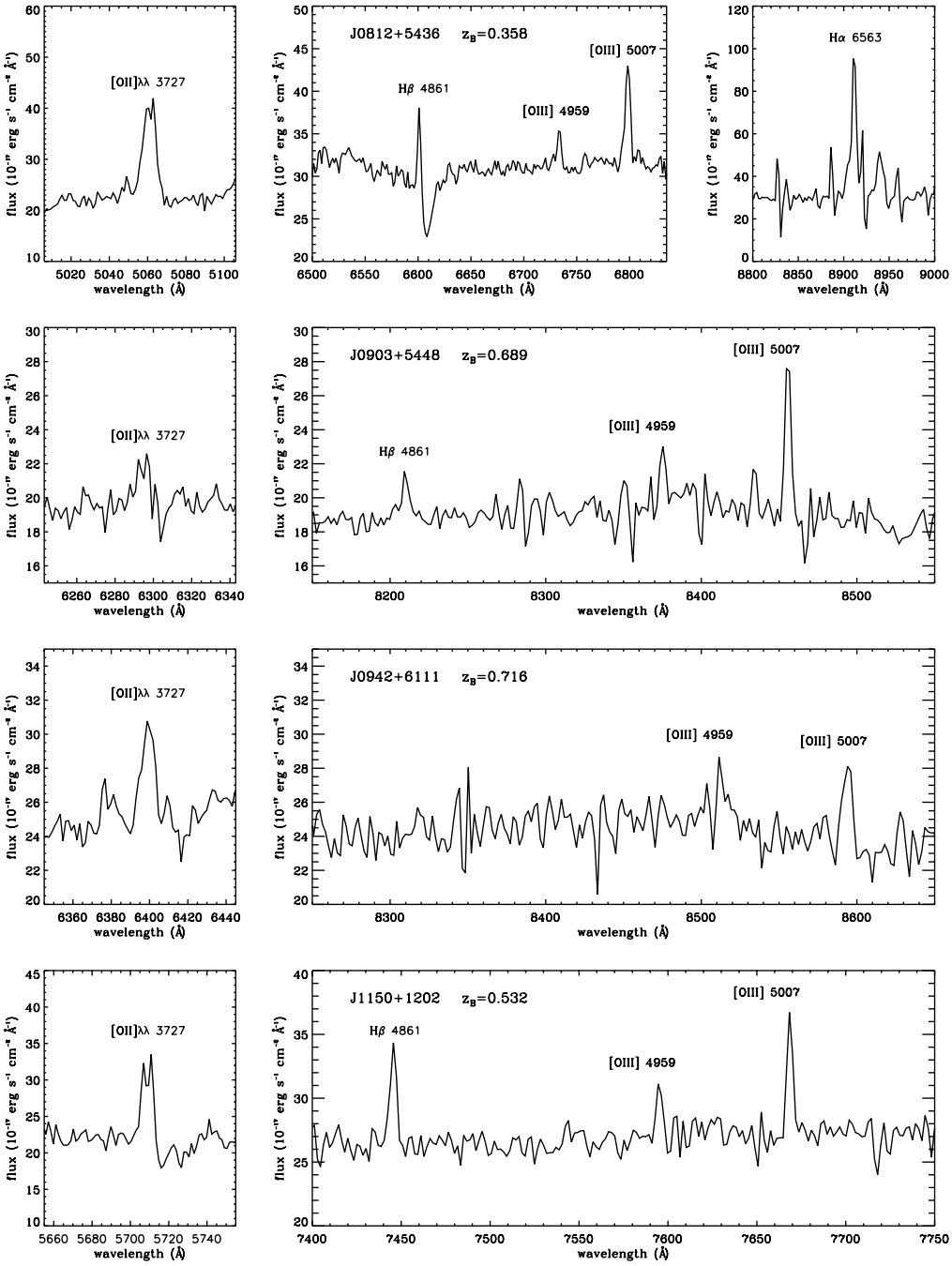

Figure 3.5: *Emission lines of the background galaxies in the SDSS spectra for the selected gravitational lens candidates (from Princeton/MIT SDSS Spectroscopy).*

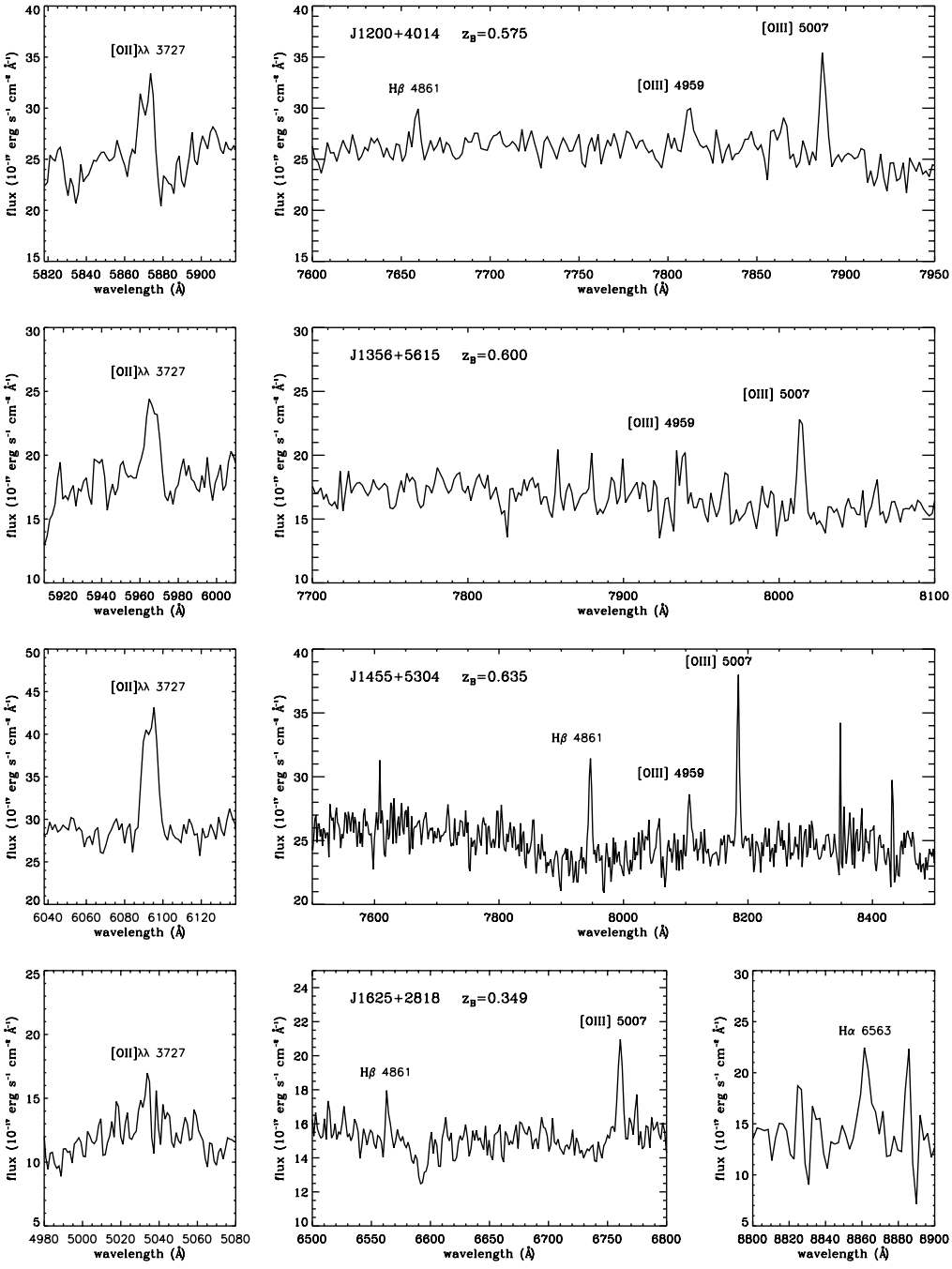

Figure 3.5: *(continued)*

3.3 Follow-up of lens candidates

3.3.1 Strategy

We use a combination of u'-band imaging and spatially resolved long-slit spectroscopy to confirm or reject the lensing hypothesis for the eight disk-lens candidates. Observations require a combination of both methods as the multiple images we want to detect are faint (they are not visible in the SDSS images) and are expected to be close to the galaxy center (disk galaxies have smaller Einstein radii than elliptical galaxies, due to their lower central concentration).

Imaging in the u' band provided, after modeling and subtraction of the foreground galaxy, an indication of the position of the potential lensed images, which guided us for positioning the slit for spectroscopic observations. However, the residuals in the image could also be non-smooth parts from the galaxy; therefore we considered them only as potential lensed images of a background source, and upgraded them to confirmed lensed images only when finding in the long-slit spectroscopy a background galaxy emission line at the same position. The u' band was chosen over other optical bands because it minimizes the contamination from the foreground massive disk galaxy, which is faint in the blue end of the spectrum, while the background source is likely to be bright in the u' band, as indicated by its strong emission lines tracing the presence of star-forming regions.

The SDSS spectra, which were taken with a $3''$ diameter fiber, have already shown that there is a background source near to the line-of-sight of the candidate lens galaxy. Spatially resolved long-slit spectroscopy allows us to detect spatially resolved multiple images of the emission lines of the background galaxy. As the slit can probe only a limited region around the foreground galaxy (e.g., the north-south axis, or the east-west axis), we placed it according to the galaxy-subtracted u'-band image. If we detected one potential lensed image we placed the slit in a position going through the image and the center of the galaxy; if we found multiple images around the galaxy, we took spectra in two different positions of the slit which optimized the number of potential lensed images covered by our

Table 3.3. *Seeing (FWHM) conditions during observations (in arcsec)*

Lens	u' exptime 1800 s	g' exptime 300 s	r' exptime 300 s	i' exptime 300 s	spectroscopy: east-west slit	spectroscopy: north-south slit
J0812+5436	1.15	1.43	1.39	1.65	1.08	···
J0903+5448	1.13	1.3	1.32	1.50	···	1.14
J0942+6111	1.30	1.39	1.24	1.52	0.70	···
J1150+1202	1.17	2.02	1.24	1.71	0.89	···
J1200+4014	1.17	1.11	1.17	1.02	0.76	1.14
J1356+5615	1.11	1.17	1.15	0.85	0.76	0.91
J1455+5304	1.02	1.28	1.04	0.95	···	1.00
J1625+2818	1.00	···	···	···	0.57	0.86

observations.

This strategy gave us a high chance of detecting the presence of multiple images of the same background source around the foreground lensing galaxy.

Confirming the presence of a disk in the candidate lensing galaxies was achieved by taking additional optical images in the g', r' and i' bands. Four of the candidate lensing galaxies were visually identified as disk galaxies. For the other galaxies, we made a fit of the main galaxy component in the u', g', r' and i' bands and deduced a first-order estimate about the morphology of the galaxy.

We now present the optical imaging and spectroscopy of the eight gravitational lens candidates.

3.3.2 Imaging

Observations

Optical images of the lens candidates were taken at the 2.5-m Nordic Optical Telescope (NOT), at the Observatorio del Roque de los Muchachos (Canary Islands, Spain), with the MOSaic CAmera (MOSCA) during 2007 April 14-17 under variable weather conditions. We used the MOSCA instrument to take advantage of its good sensitivity in the u' band. As the size of our targets does not require a mosaic camera, we centered our observations on one of the four CCDs of the mosaic, the CCD10 which showed the best properties regarding flux gradient and bad pixels on the chip. We used the SDSS filters u', g', r' and i' so as

to be able to directly calibrate our observations with the SDSS database. The u'-band observations were performed during dark sky conditions and when the seeing conditions were favorable, in order to resolve the multiple images of the background sources. Exposure times of 1800 s were used due to the expected faintness of the lensed images. The g'-, r'- and i'-band observations were performed during grey sky conditions with exposure times of 300 s in each band (see Table 3.3 for the details of the observations).

Data reduction

The optical images of the lens candidates were processed in IDL using standard data reduction techniques. The data were bias-subtracted and flat-fielded, the cosmic rays were removed using L.A.Cosmic (van Dokkum 2001). The dark current was negligible.

MOSCA images have for peculiarities that the images are 2×2 binned, and the overscan stripe is made of only one column. The last point requires carefulness in the data reduction, as it leads to poor statistics in determining the overscan level, and thus in determining the bias level to subtract from each image. However, a linear relation was found between the average bias level and the average overscan level with little scatter. Using this linear relation to scale the 2D structure of the masterbias, the bias level was accurately subtracted, when tested on individual bias images.

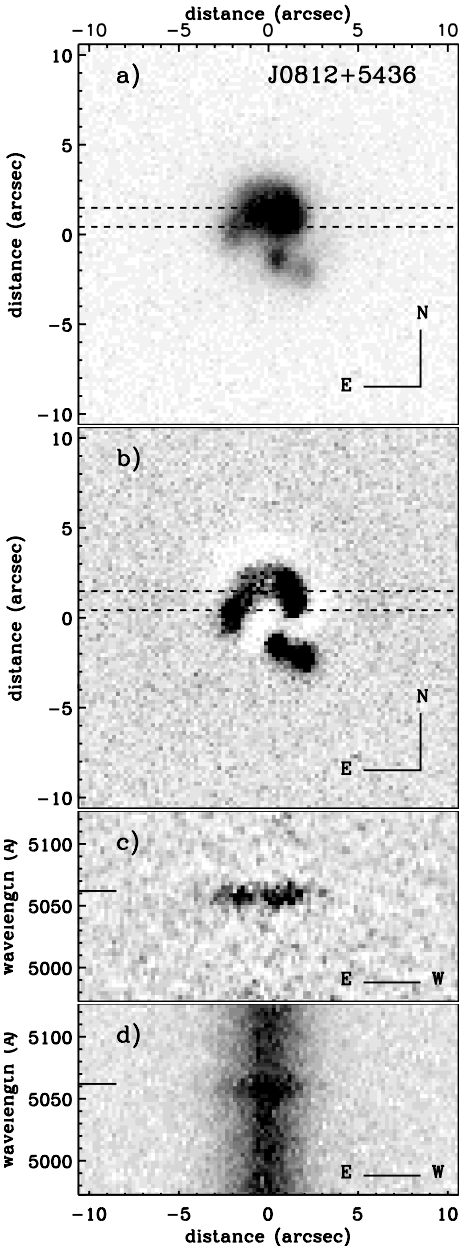

Figure 3.6: *Panel a) shows the u'-band image of J0812+5436, and panel b) the u'-band residual image after galaxy subtraction. The dashed lines indicate the position and width of the slit used to take long-slit spectra of the target. Panel c) shows a section of the 2D spectrum of J0812+5436 with the [O II] $\lambda\lambda$3727 emission line of the background galaxy, at $\lambda = 5062$ Å, after skyline and galaxy subtraction, convolved with a gaussian of $\sigma = 1$ pixel for display purpose ; panel d) shows the same part of spectrum after skyline subtraction only.*

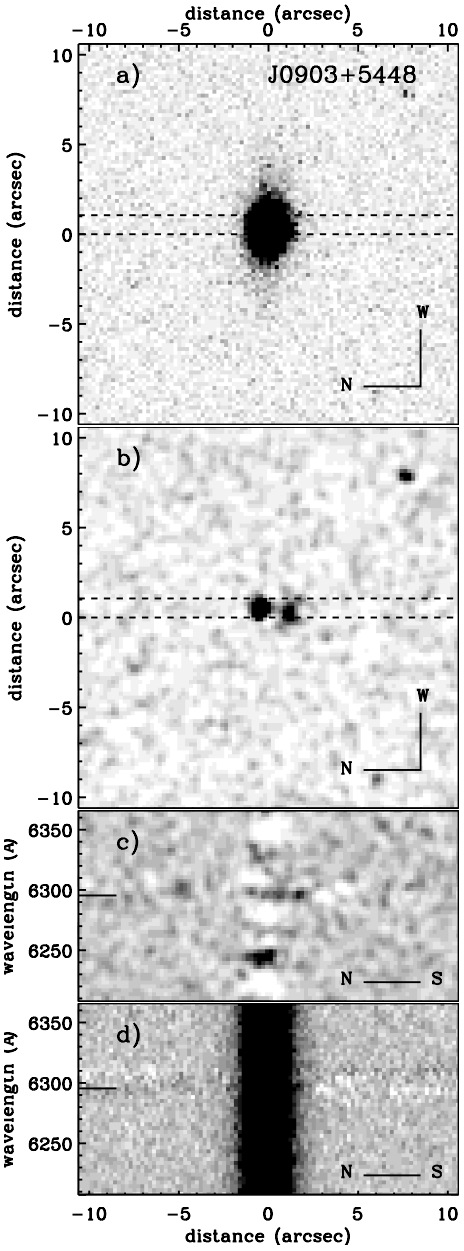

Figure 3.7: *Panel a) shows the u'-band image of J0903+5448, and panel b) the u'-band residual image after galaxy subtraction, convolved with a gaussian of $\sigma = 2$ pixels for display purpose. The dashed lines indicate the position and width of the slit used to take long-slit spectra of the target. Panel c) shows a section of the 2D spectrum of J0903+5448 with the [O II] $\lambda\lambda$3727 emission line of the background galaxy, at $\lambda = 6295$ Å, after skyline and galaxy subtraction, convolved with a gaussian of $\sigma = 2$ pixels for display purpose; panel d) shows the same part of spectrum after skyline subtraction only.*

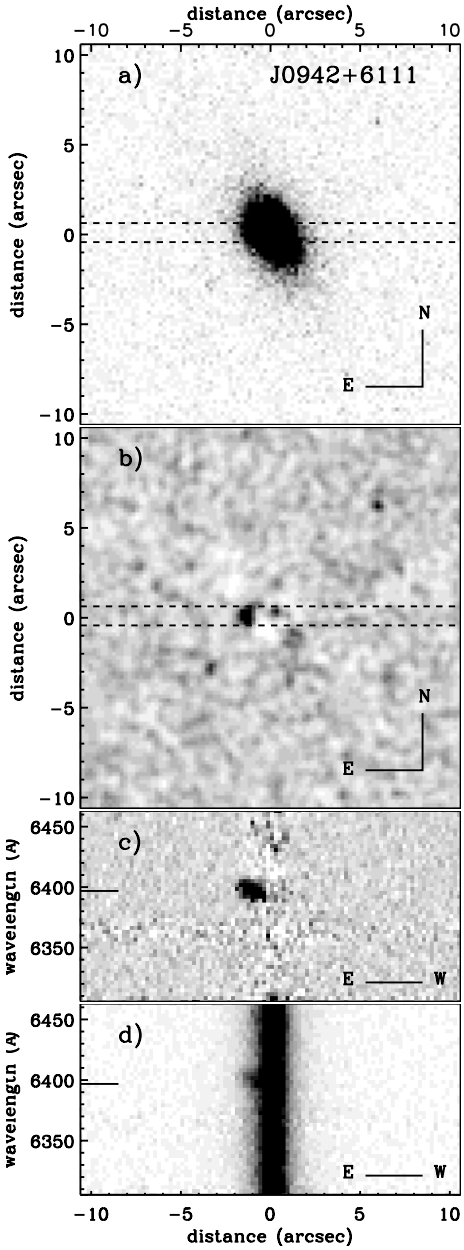

Figure 3.8: *Panel a) shows the u'-band image of J0942+6111, and panel b) the u'-band residual image after galaxy subtraction, convolved with a gaussian of $\sigma = 2$ pixels for display purpose. The dashed lines indicate the position and width of the slit used to take long-slit spectra of the target. Panel c) shows a section of the 2D spectrum of J0942+6111 with the [O II] $\lambda\lambda$3727 emission line of the background galaxy, at $\lambda = 6397$ Å, after skyline and galaxy subtraction; panel d) shows the same part of spectrum after skyline subtraction only.*

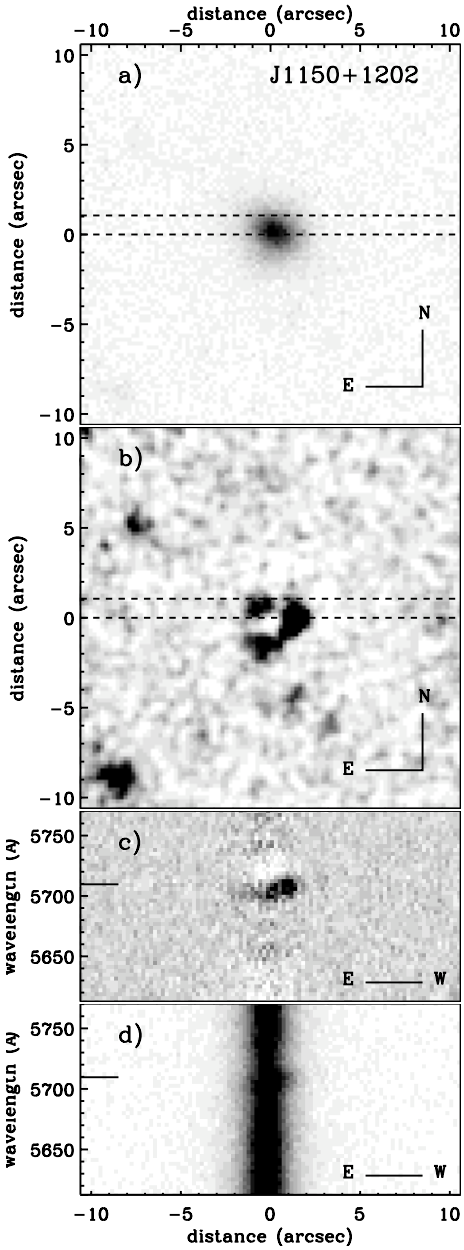

Figure 3.9: *Panel a) shows the u'-band image of J1150+1202, and panel b) the u'-band residual image after galaxy subtraction, convolved with a gaussian of $\sigma = 1$ pixel for display purpose. The dashed lines indicate the position and width of the slit used to take long-slit spectra of the target. Panel c) shows a section of the 2D spectrum of J1150+1202 with the [O II] $\lambda\lambda$3727 emission line of the background galaxy, at $\lambda = 5710$ Å, after skyline and galaxy subtraction; panel d) shows the same part of spectrum after skyline subtraction only.*

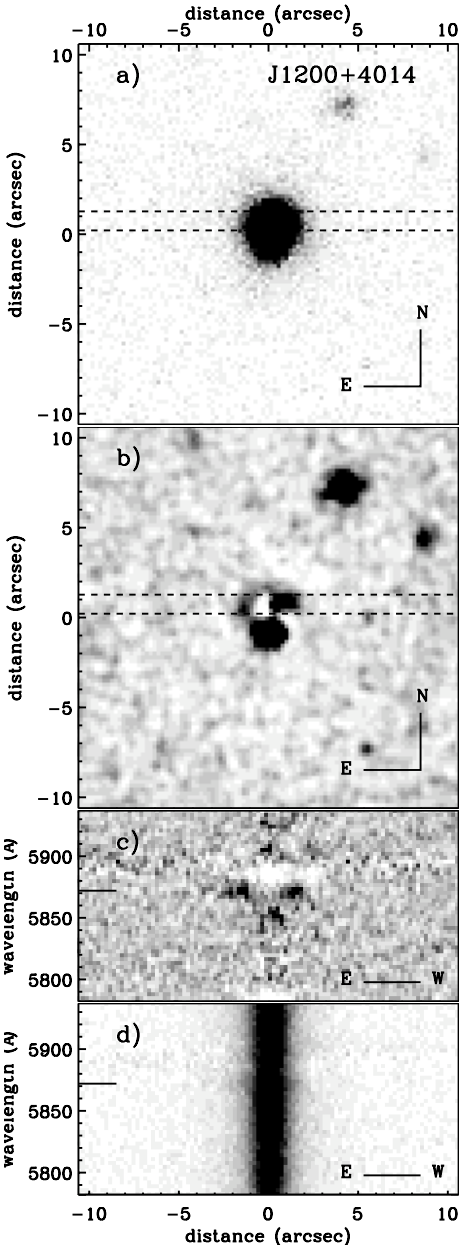

Figure 3.10: *Panel a) shows the u'-band image of J1200+4014, and panel b) the u'-band residual image after galaxy subtraction, convolved with a gaussian of $\sigma = 2$ pixels for display purpose. The dashed lines indicate the position and width of the slit used to take the east-west long-slit spectra of the target. Panel c) shows a section of the 2D spectrum of J1200+4014 with the [O II] $\lambda\lambda$3727 emission line of the background galaxy, at $\lambda = 5871$ Å, after skyline and galaxy subtraction, convolved with a gaussian of $\sigma = 1$ pixel for display purpose; panel d) shows the same part of spectrum after skyline subtraction only.*

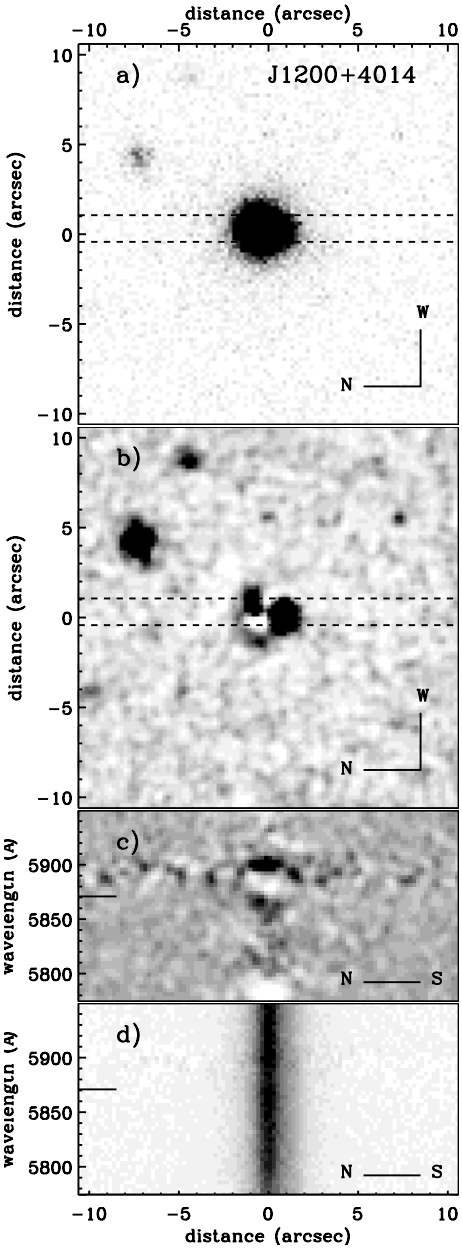

Figure 3.11: *Panel a) shows the u'-band image of J1200+4014, and panel b) the u'-band residual image after galaxy subtraction, convolved with a gaussian of $\sigma = 2$ pixels for display purpose. The dashed lines indicate the position and width of the slit used to take the north-south long-slit spectra of the target. Panel c) shows a section of the 2D spectrum of J1200+4014 with the [O II] $\lambda\lambda$3727 emission line of the background galaxy, at $\lambda = 5871$ Å, after skyline and galaxy subtraction, convolved with a gaussian of $\sigma = 2$ pixels for display purpose; panel d) shows the same part of spectrum after skyline subtraction only.*

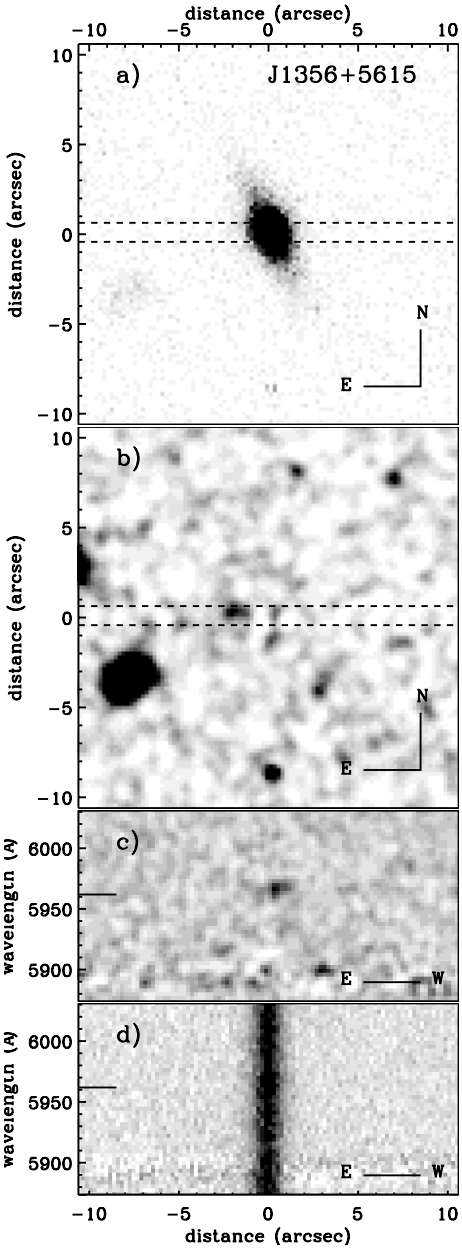

Figure 3.12: *Panel a) shows the u'-band image of J1356+5615, and panel b) the u'-band residual image after galaxy subtraction, convolved with a gaussian of $\sigma = 3$ pixels for display purpose. The dashed lines indicate the position and width of the slit used to take the east-west long-slit spectra of the target. Panel c) shows a section of the 2D spectrum of J1356+5615 with the [O II] $\lambda\lambda$3727 emission line of the background galaxy, at $\lambda = 5962$ Å, after skyline and galaxy subtraction, convolved with a gaussian of $\sigma = 2$ pixels for display purpose; panel d) shows the same part of spectrum after skyline subtraction only.*

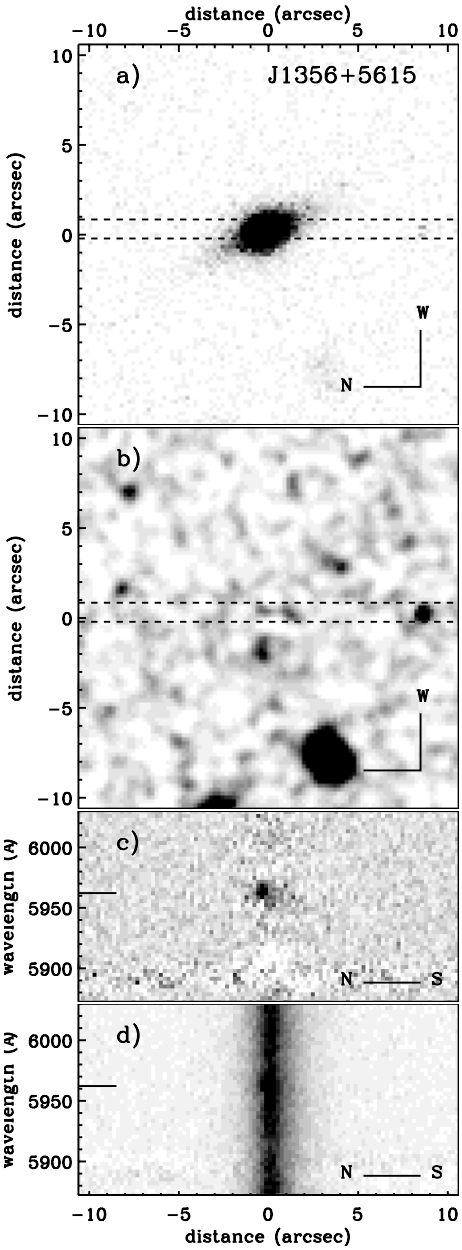

Figure 3.13: *Panel a) shows the u'-band image of J1356+5615, and panel b) the u'-band residual image after galaxy subtraction, convolved with a gaussian of $\sigma = 3$ pixels for display purpose. The dashed lines indicate the position and width of the slit used to take the north-south long-slit spectra of the target. Panel c) shows a section of the 2D spectrum of J1356+5615 with the [O II] $\lambda\lambda$3727 emission line of the background galaxy, at $\lambda = 5962$ Å, after skyline and galaxy subtraction; panel d) shows the same part of spectrum after skyline subtraction only.*

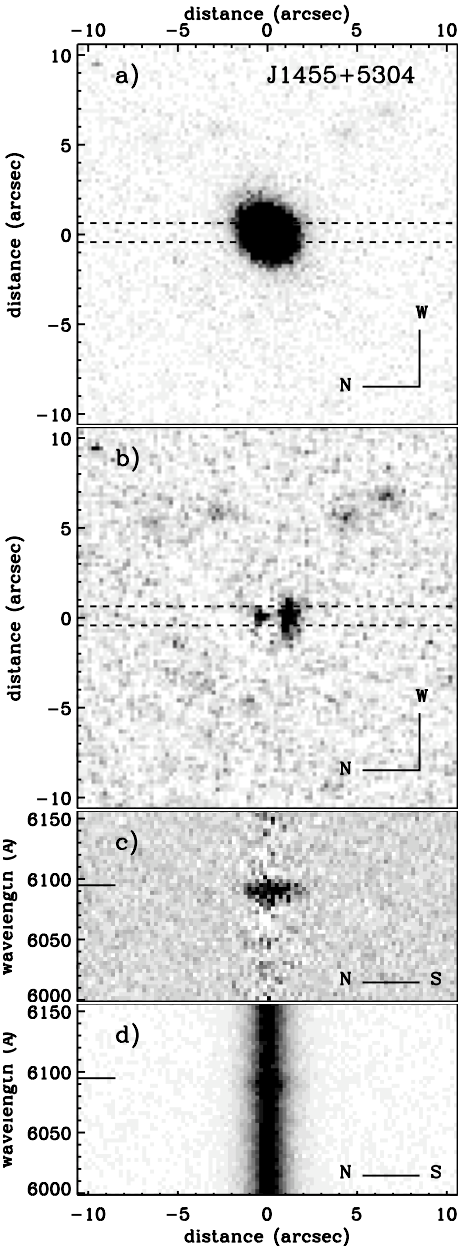

Figure 3.14: *Panel a) shows the u'-band image of J1455+5304, and panel b) the u'-band residual image after galaxy subtraction, convolved with a gaussian of $\sigma = 1$ pixel for display purpose. The dashed lines indicate the position and width of the slit used to take long-slit spectra of the target. Panel c) shows a section of the 2D spectrum of J1455+5304 with the [O II] $\lambda\lambda$3727 emission line of the background galaxy, at $\lambda = 6095$ Å, after skyline and galaxy subtraction; panel d) shows the same part of spectrum after skyline subtraction only.*

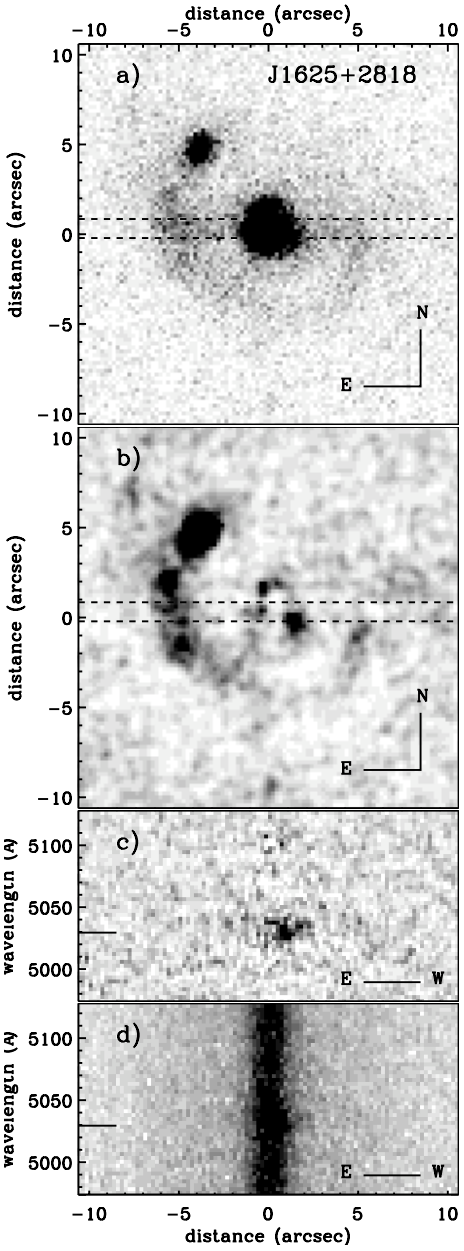

Figure 3.15: *Panel a) shows the u'-band image of J1625+2818, and panel b) the u'-band residual image after galaxy subtraction, convolved with a gaussian of $\sigma = 2$ pixels for display purpose. The dashed lines indicate the position and width of the slit used to take the east-west long-slit spectra of the target. Panel c) shows a section of the 2D spectrum of J1625+2818 with the [O II] $\lambda\lambda$3727 emission line of the background galaxy, at $\lambda = 5029$ Å, after skyline and galaxy subtraction, convolved with a gaussian of $\sigma = 1$ pixel for display purpose; panel d) shows the same part of spectrum after skyline subtraction only.*

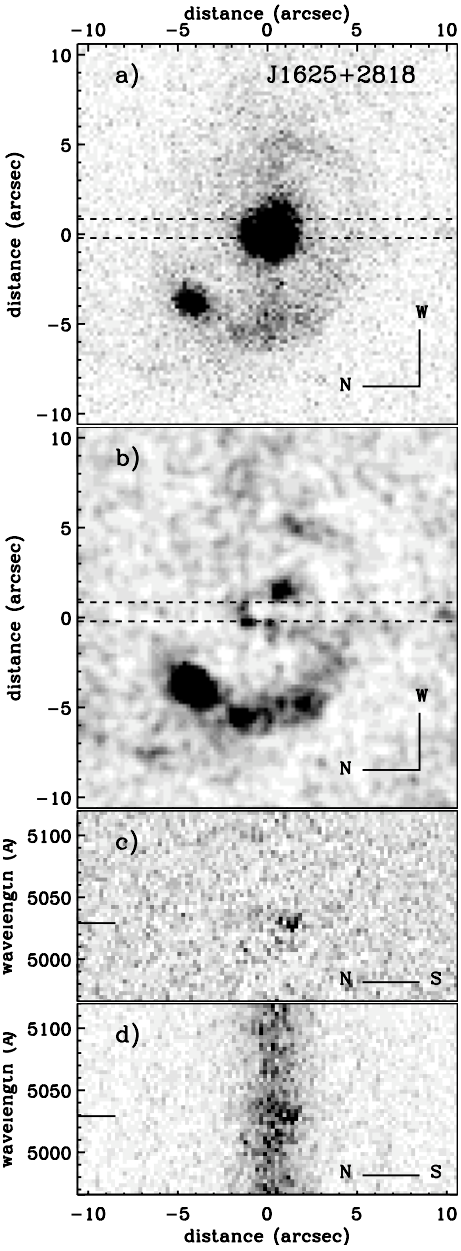

Figure 3.16: *Panel a) shows the u'-band image of J1625+2818, and panel b) the u'-band residual image after galaxy subtraction, convolved with a gaussian of $\sigma = 2$ pixels for display purpose. The dashed lines indicate the position and width of the slit used to take the north-south long-slit spectra of the target. Panel c) shows a section of the 2D spectrum of J1625+2818 with the [O II] $\lambda\lambda$3727 emission line of the background galaxy, at $\lambda = 5029$ Å, after skyline and galaxy subtraction, convolved with a gaussian of $\sigma = 1$ pixel for display purpose; panel d) shows the same part of spectrum after skyline subtraction only.*

Galaxy modeling

The surface-brightness profile of the galaxies were modeled using the publicly available software GALFIT (Peng et al. 2002). We used a Sérsic function (Sérsic 1963, 1968), that is, a seven parameter model (x, y, orientation, ellipticity, Sérsic index n, scale radius and total magnitude), convolved with the point spread function, as defined from the stars in the field. The advantage of fitting a Sérsic function is to recover a large range of galaxy profiles depending on the index n, for example, from the de Vaucouleurs profile ($n = 4$) to the exponential disk ($n = 1$).

In the u' band, we use from one to three Sérsic components in our models, depending on each case, in order to get a proper subtraction of the galaxy to identify the potential lensed images in the residuals. During this process, any strong emission from the candidate lensed background source was masked out to avoid skewing the fit to the lensing galaxy. The u'-band images and residual images are presented in Figs. 3.6 to 3.16 (a and b). The results are summarized case by case in § 3.3.4.

The data for the lensing galaxies in the g', r', and i'-bands were modeled by only one Sérsic component, as here we are only interested in the morphology of the main component. This part is treated in more detail in § 3.3.5.

3.3.3 Long-slit spectroscopy

Observations

Long-slit spectroscopy of the lens candidates was obtained at the NOT with the Andalucia Faint Object Spectrograph and Camera (ALFOSC) during 2007 May 7-11 under variable weather conditions. We used a slit width ranging from $1''$ to $1.3''$ depending on the seeing. We chose the grism #4 which covers a wavelength range 3200 Å to 9100 Å matching that of the SDSS spectra. This was a crucial point in order to confirm the presence of the three or more emission lines detected in the SDSS spectra of our gravitational lens candidates. However, it was at the expense of the resolving power of R$\sim$710, which is lower than that

used for the SDSS spectra.

The slit position was determined based on the results of the galaxy subtraction presented in § 3.3.4.

Data reduction

The spectroscopic data were processed using standard data reduction methods with the Image Reduction and Analysis Facility (IRAF), and using L.A.Cosmic for the cosmic-ray removal. The 2D spectra were bias subtracted, flat-fielded, and dispersion corrected using He and Ne arc spectra. The skylines were subtracted by fitting a low order cubic spline interpolation to each row and subtracting it from the 2D spectrum. The galaxy contribution was subtracted using a similar technique along the columns of the galaxy spectrum. 1D spectra were extracted from the calibrated, skyline-subtracted 2D spectra, in order to measure with better precision the wavelength of the background source emission lines, and the redshift of the background source.

To double-check the results, 1D spectra were also extracted directly from the raw bias-subtracted, flat-fielded 2D spectra, the skylines and background subtraction being performed during the extraction. The 1D spectra extracted using both methods are consistent with each other, in their background emission lines and source redshifts.

3.3.4 Combined results from imaging and long-slit spectroscopy

We present in a combined figure, for each lens candidate, the u' band photometry and the long-slit spectroscopy, showing both the observations and the residuals after galaxy subtraction (see Figs. 3.6 to 3.16). The optical images and the 2D spectra are presented with an identical spatial scale for the horizontal axis. The slit is indicated for each galaxy by two dashed lines in the u'-band images. In the 2D spectra, the spatial axis corresponds to the position along the slit, and the wavelength axis corresponds to a wavelength range around the expected [O II] $\lambda\lambda$3727 emission line of the background galaxy. When spectroscopic observations of a lens candidate were obtained in two orientations of the slit, the

two spectra are presented in separate figures, with the galaxy image rotated to present the slit horizontally, as indicated by the compass on each image. Below we discuss the lens candidates case by case, including the photometric data, spectroscopic data and combined results.

J0812+5436

Imaging–The galaxy-subtracted u'-band image shows two bright residuals linked by an arc around the north of the galaxy, suggestive of lensed images (see Fig. 3.6, *a* and *b*). The two structures at the south of the galaxy are difficult to identify, but the nearest to the galaxy might be a lensed image. We planned spectroscopic observations in two positions of the slit: an orientation east-west passing through the side images, and an orientation north-south to study the southern objects. Unfortunately, bad weather conditions prevented us from taking the north-south spectrum.

2D spectrum–We study the 2D spectrum around $\lambda = 5062$ Å, the wavelength of the expected [O II] $\lambda\lambda$3727 emission line. After galaxy subtraction, two bright residual images appear on each side of the galaxy at the wavelength $\lambda = 5060$ Å (see Fig. 3.6, *c* and *d*). The west image is at $0.7 \pm 1.1''$ and the east image at $1.3 \pm 0.6''$ from the center of the galaxy spectrum. They correspond to the positions through the slit of the images detected in the u' band. Although the two images in the spectrum are not neatly separated, the faint signal between them corresponds to the arc detected in the u' band, thus confirming the strong lens nature of the candidate.

Conclusions–We confirmed that J0812+5436 is a strong gravitational lens. The Einstein radius is $r_E = 1.8 \pm 0.4''$, based on the half distance between the two confirmed lensed images, in the u' band image. The redshift of the lensed galaxy is $z_B = 0.357$, as measured from the one dimensional spectrum. However, it is not possible to detail the nature of the residual images at the south of the galaxy, as we lack spectroscopic observations for them. The object nearest to the galaxy might be a lensed image of the same background source, while the furthest object might be unrelated.

J0903+5448

Imaging–The galaxy-subtracted u'-band image shows two residuals suggestive of lensed images (see Fig. 3.7, *a* and *b*). The north image is at $0.6\ \pm 0.6''$ and the south image at $0.9 \pm 0.3''$ from the galaxy center. We obtained spectroscopic observations with the slit in a north-south orientation, going through the two images.

2D spectrum–We study the 2D spectrum around $\lambda = 6295$ Å, the wavelength of the expected [O II] $\lambda\lambda$3727 emission line. After galaxy subtraction, a faint and continuous signal across the galaxy width appears at $\lambda = 6298$ Å (see Fig. 3.7, *c* and *d*), extending from $1.0''$ north to $2.0''$ south of the galaxy center. However, we do not detect distinctly an emission line from the background galaxy, nor if it is multiply imaged. The proximity of a strong skyline at $\lambda = 6300$ Å, the subtraction of which is bringing noise in this region of the spectrum, makes the study difficult. The [O III] 5007 emission line would in theory bring better information on the lens candidate, presenting a better S/N ratio (see Fig. 3.5), but in practice the fringing in the red part of our spectra makes it even more difficult to study.

Conclusions–The presence of a background galaxy near J0903+5448 is confirmed from the SDSS (Princeton/MIT spectroscopy) one dimensional spectrum of the target, at a redshift $z_B = 0.689$. However, we do not detect properly the emission lines from the background galaxy in our own spectrum, due to the vicinity of a strong sky line near to the [O II] $\lambda\lambda$3727 emission line, and the fringing in the red part of the spectrum where the other strong emission lines of the background galaxy are found. Although the two residual images appearing in the u' band observation are very suggestive of lensing, better spectroscopic observations of the [O III] 5007 emission line would be necessary to confirm the lens nature of the candidate.

J0942+6111

Imaging–The galaxy-subtracted u'-band image shows a residual image at the east of the galaxy center (see Fig. 3.8, *a* and *b*). We planned spectroscopic observations with the slit

in the east-west orientation, passing through the potential lensed image and the center of the galaxy.

2D spectrum–We study the 2D spectrum around $\lambda = 6397$ Å, the wavelength of the expected [O II] $\lambda\lambda$3727 emission line. After galaxy subtraction, one bright residual image appears at 1.1 $\pm 0.8''$ east of the galaxy center, at the wavelength $\lambda = 6396$ Å (see Fig. 3.8, *c* and *d*).

Conclusions–We confirmed the presence of an image of a background source near J0942+6111. The redshift of the background galaxy is $z_B = 0.716$, as measured from the one dimensional spectrum. We can not confirm that the system is a lens, as we detect only one image of the background source.

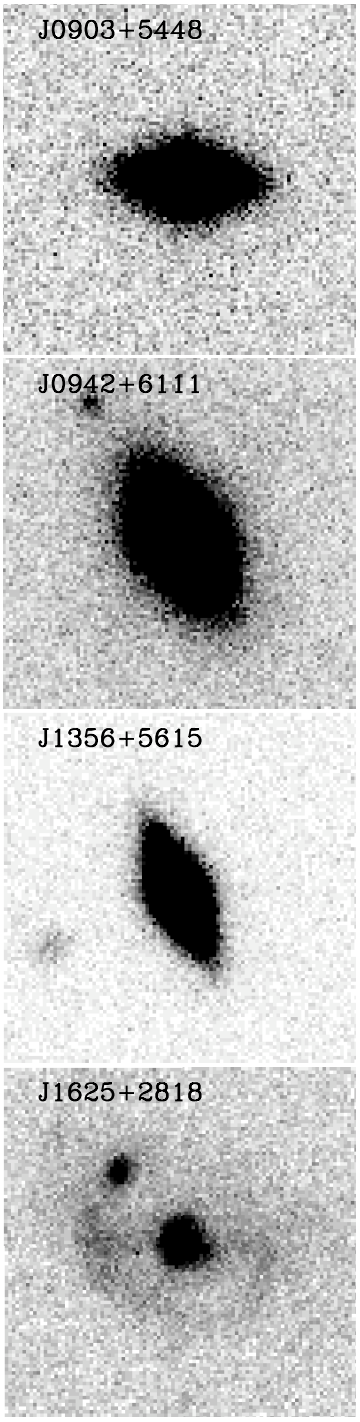

Figure 3.17: *Imaging in the r' band of the targets which are obvious disk galaxies (J1625+2818 is shown in the u' band). The size of the images is* $21.7'' \times 21.7''$.

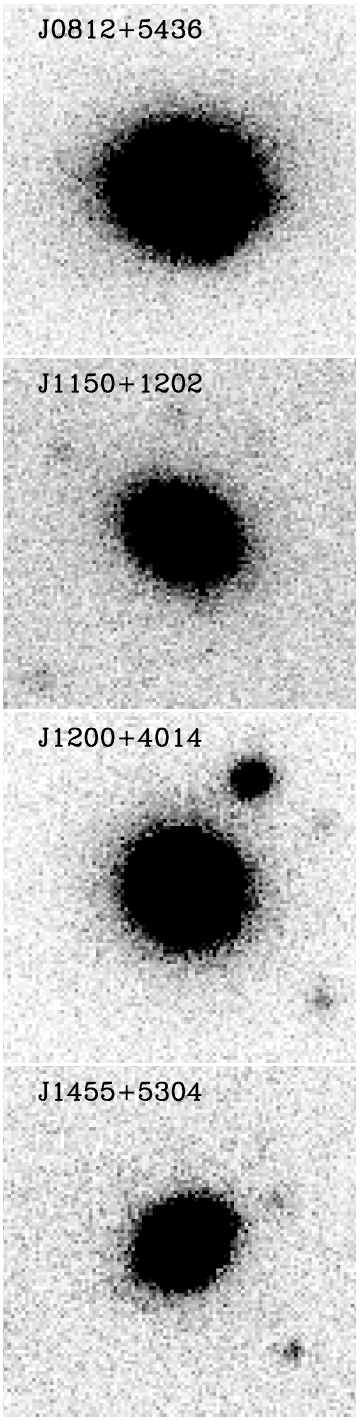

Figure 3.18: *Imaging in the r' band of the targets whose morphology can not be deduced by visual inspection and require galaxy modeling to know if they are disk galaxies. The size of the images is* $21.7'' \times 21.7''$.

J1150+1202

Imaging–The galaxy-subtracted u'-band image shows three bright residual images in a west, north-east and south-east configuration (see Fig. 3.9, *a* and *b*). We planned spectroscopic observations with east-west and north-south orientations of the slit to cover the three potential lensed images. Unfortunately, bad weather conditions prevented us from taking the north-south spectrum.

2D spectrum–We study the 2D spectrum around $\lambda = 5710$ Å, the wavelength of the expected [O II] $\lambda\lambda$3727 emission line. After galaxy subtraction, one bright residual image appears at $0.8 \pm 0.8''$ west of the galaxy center, at the wavelength $\lambda = 5704$ Å (see Fig. 3.9, *c* and *d*). The emission line is superposed to the Mg I 5175 absorption line (in white in Fig. 3.9, *c*) of the foreground galaxy at redshift $z_f = 0.105$. A faint extension of the [O II] $\lambda\lambda$3727 emission line is seen at the east of the galaxy, which may indicate a second image of the emission line. Comparing to the u' band, the bright image of the emission line corresponds to the west image, and the faint extension corresponds to the north-east image. As the west image appears brighter than the other image in the u' band observations, this explain that it is less affected by the presence of the Mg I 5175 absorption line.

Conclusions–We confirm the presence of an image of a background source near J1150+1202. The redshift of the background galaxy is $z_B = 0.531$, as measured from the one dimensional spectrum. We can not confirm that the source is multiply imaged, but the presence of a faint extension to the [O II] $\lambda\lambda$3727 emission line concording with the north-east image in the u'-band residuals gives strong indication for multiple images. It is not possible to detail the nature of the residual image at the south of the galaxy, as we lack spectroscopic observations for it. However, the presence of three images in the u'-band residual image, concording with one and possibly two spectroscopically confirmed images of the background source, while the third image is not proven spectroscopically, indicates the system is probably a strong gravitational lens.

J1200+4014

Imaging–The galaxy-subtracted u'-band image shows three residual images in a north-east, north-west and south configuration, suggestive of lensed images (see Fig. 3.10, *a* and *b*). Moreover, the three images seem to be linked by a faint ring, suggestive of an Einstein ring superposed to the lensed images. We obtained spectroscopic observations in the east-west and north-south orientations, covering the three potential lensed images.

2D spectrum–We study the 2D spectra around $\lambda = 5871$ Å, the wavelength of the expected [O II] $\lambda\lambda$3727 emission line. After galaxy subtraction in the east-west spectrum, two bright residual images appear on each side of the galaxy at the wavelength $\lambda = 5870$ Å (see Fig. 3.10, *c* and *d*). In spite of the presence of a strong skyline at $\lambda = 5890$ Å, the subtraction of which induces noise in this part of the spectrum, the presence of the two residual images at the wavelength of the expected [O II] $\lambda\lambda$3727 emission line give a strong indication for multiple images of the background source. The east image is at $1.7 \pm 0.7''$ and the west image at $1.0 \pm 0.6''$ from the center of the galaxy spectrum. Comparing the position of the two images to the u'-band residual image, it appears these two images correspond to the north-east and north-west images . After galaxy subtraction in the north-south spectrum, we detect a faint image of the source on the north side of the galaxy at the wavelength $\lambda = 5870$ Å, but we find no evidence for the bright south image, which is therefore not belonging to the same source (see Fig. 3.11, *c* and *d*).

Conclusions–We confirm the presence of a background galaxy near J1200+4014, with strong indication that it is multiply imaged, and therefore, that the system is a lens. The redshift of the background galaxy is $z_B = 0.575$, as measured from the one dimensional spectrum. The third image, at the south of the galaxy, is not an image of the identified background source, but probably an unrelated object which is almost superposed to the foreground galaxy.

J1356+5615

Imaging–The galaxy-subtracted u'-band image shows two residual images at the east and south of the galaxy (see Fig. 3.12, *a* and *b*). There is also a central image which might be an artifact due to the difficulty of fitting the central pixels. We obtained spectroscopic observations in the east-west and north-south orientations of the slit, covering the three potential lensed images.

2D spectrum–We study the 2D spectra around $\lambda = 5962$ Å, the wavelength of the expected [O II] $\lambda\lambda$3727 emission line. After galaxy subtraction of each of the east-west and north-south spectra, a residual image appears in each spectrum, respectively at 0.7 $\pm 0.5''$ west and 0.7 $\pm 0.3''$ north of the center of the galaxy spectrum, at the wavelength $\lambda = 5962$ Å (see Fig. 3.12 and Fig. 3.13, *c* and *d*). These correspond to the central image in the u'-band residual image. We do not detect any of the two other images present in the u'-band residual image.

Conclusions–We confirm the presence of a central image of a background galaxy detected in both orientations of the slit. The redshift of the background galaxy is $z_B = 0.575$, as measured from the one dimensional spectrum. It is not possible to determine if the images in the two spectra are two detections of the same image, or if there are actually two central images of the background source, or if they form a lensing arc. Therefore we can not conclude whether J1356+5615 is a strong lens or not.

J1455+5304

Imaging–The galaxy-subtracted u'-band image shows two residual images suggestive of lensed images, one on each side of the galaxy center (see Fig. 3.14, *a* and *b*). The north image is at 0.5 $\pm 0.5''$ and the south image at 1.0$\pm 0.4''$ from the galaxy center. We obtained spectroscopic observations with the slit in the north-south orientation, going through the two images.

2D spectrum—We study the 2D spectrum around $\lambda = 6095$ Å, the wavelength of the expected [O II] $\lambda\lambda$3727 emission line. After galaxy subtraction, a residual image extending

across the galaxy width appears at the wavelength $\lambda = 6090$ Å (see Fig. 3.14, *c* and *d*). Although we observe a continuous signal, we can make the hypothesis that there are two unresolved images, and estimate their positions assuming they are separated at the center of the galaxy. This leads to a north image at $0.6 \pm 0.6''$ and a south image at $0.9 \pm 0.9''$ from the center of the galaxy spectrum. This is consistent with the position through the slit of the two images detected in the u' band, thus confirming the strong lens nature of the candidate.

Conclusion–We confirm that J1455+5304 is a strong gravitational lens. The Einstein radius is $r_E = 0.7 \pm 0.4''$, based on the half distance between the two confirmed lensed images, in the u' band image. The redshift of the background galaxy is $z_B = 0.634$, as measured from the one dimensional spectrum.

J1625+2818

Imaging–The galaxy-subtracted u'-band image shows residuals suggestive of lensing: one bright image at the south-west of the bulge, and three smaller images superposed to what seems an arc on the north-east side of the bulge (see Fig. 3.15, *a* and *b*). We obtained spectroscopic observations in the east-west and north-south orientations, covering the potential lensed images.

2D spectrum–We study the 2D spectra around $\lambda = 5029$ Å, the wavelength of the expected [O II] $\lambda\lambda$3727 emission line. After galaxy subtraction in the east-west spectrum, a residual image appears at the wavelength $\lambda = 5032$ Å, at $0.8 \pm 0.3''$ west from the center of the galaxy spectrum (see Fig. 13, c and d). It corresponds to the position of the south-west image in the u'-band residual image. After galaxy subtraction in the North-South spectrum, a residual image appears at the wavelength $\lambda = 5032$ Å, at $0.9 \pm 0.5''$ south from the center of the galaxy spectrum (see Fig. 14, c and d). When compared to the u'-band residual image, the position of the image in the north-south spectrum does not correspond to the position of the north-east images which the slit was intended to probe, but corresponds to the position of the south-west image at the edge of the slit. However,

Table 3.4. *Morphology*

	u' band	g' band	r' band	i' band
		J0812+5436		
χ^2 for $n = 1$	1.548	1.378	1.689	2.424
χ^2 for $n = 4$	2.227	1.417	1.673	1.482
best fit n	0.74	1.82	1.92	2.35
		J1150+1202		
χ^2 for $n = 1$	1.129	1.129	1.499	1.279
χ^2 for $n = 4$	1.127	1.110	1.367	1.172
best fit n	1.98	2.32	2.42	3.06
		J1200+4014		
χ^2 for $n = 1$	1.161	1.453	1.664	1.697
χ^2 for $n = 4$	1.133	1.204	1.265	1.264
best fit n	3.38	2.83	2.68	2.82
		J1455+5304		
χ^2 for $n = 1$	1.181	1.216	1.419	1.517
χ^2 for $n = 4$	1.160	1.162	1.235	1.357
best fit n	2.62	2.35	2.80	2.52

we can see on the u' band image that the south-west image is brighter and larger than the other residual images. Moreover, the spectrum of the foreground galaxy shows many emission lines: this makes the peak of the [O II] $\lambda\lambda$3727 emission line of the background galaxy difficult to detect among the peaks of the foreground galaxy (see Fig. 3). This could explain that we detect only the brightest of the images of the background emission line, while the fainter images would be at the level of the noise occasioned by the foreground galaxy.

Conclusions–We confirm the presence of an image of a background source near J1625+2818. The redshift of the background galaxy is $z_B = 0.350$, as measured from the one dimensional spectrum. We can not confirm that the source is multiply imaged, as we detect spectroscopically only the brightest image. The remaining residual images might be too faint to be detected in our spectra. However, the configuration of the residuals in the u' band image points toward a good probability that the system is a strong gravitational lens.

3.3.5 Morphology

The galaxies J0903+5448, J0942+6111 and J1356+5615 can be identified as disk galaxies directly from looking at their optical images[6]. As for the galaxy J1625+2818, we can see it is a barred spiral with a dominant bulge (see Fig. 3.17). However, the candidate massive disk galaxies J0812+5436, J1150+1202, J1200+4014 and J1455+5304 do not have characteristics that allow us to identify their galaxy type by simple visual inspection (see Fig. 3.18).

To gain further insight into the morphology of these galaxies, we used GALFIT to model the main component of each galaxy with a Sérsic profile. We fitted the galaxies in each of the available photometric bands: u', g', r' and i'. For each fit we used a simple method which allows us to get robust information about the morphology of the main component of the galaxies in each band: we fitted the data with a Sérsic profile keeping n fixed to 4 (de Vaucouleurs bulge), then fitted the data with a Sérsic profile keeping n fixed to 1 (exponential disk). The comparison of the χ^2 of the two fits tells us if the morphology of the galaxy is nearer to a bulge or a disk. We also fitted the data with a Sérsic profile where n is let free.

While this method allows us to determine if the galaxy morphology is definitely a disk or a bulge, it is difficult to identify S0 galaxies, which have a Sérsic index between the two models. For most of the cases, we can only say that the galaxy is not dominated by a disk, but we can not determine clearly between S0 and elliptical galaxies.

Here follows a summary galaxy by galaxy of the results, which are presented in Table 3.4.

J0812+5436

In the u' and g' bands the χ^2 of the fit is smaller for a disk ($n = 1$) while in the r' and i' band the χ^2 of the fit is smaller for a bulge ($n = 4$). This indicates that the galaxy is composed of a disk and a bulge. However, due to the very bright lensed images superposed

[6]Fitting these galaxies would not bring more information about their morphology, as GALFIT does not include the inclination of the disk as a fitting parameter, and all the three galaxies are far from edge-on. Therefore, the Sérsic index n would be increased artificially, as the light received is more concentrated due to the inclination of the disk.

Table 3.5. *Mass-to-Light ratios*

Name	$M_{\rm tot}/L_I$	$M_{\rm tot}/L_R$	$M_{\rm tot}/L_B$	$M_{\rm tot}/L_U$
J0812+5436	5.4 $\pm$1.5	8.2 $\pm$2.0	11.2 $\pm$2.8	14.6 $\pm$2.3
J1455+5304	1.5 $\pm$0.9	2.2 $\pm$1.3	3.0 $\pm$1.7	3.1 $\pm$1.9

to the galaxy, the fit may not be completely reliable, although the lensed images were masked. Therefore, we can only conclude that J0812+5436 is a probable disk or S0 galaxy.

J1150+1202

In the u' band the χ^2 of the fit is similar for a disk ($n = 1$) and a bulge ($n = 4$), while in the i', r' and i' bands the χ^2 of the fit is smaller for a bulge ($n = 4$). In addition, the best fit values in all the bands are for $1 < n < 4$, which is between a disk and a bulge model. We conclude that SDSS J1150+1202 is probably an S0 galaxy.

J1200+4014

In all bands the χ^2 of the fit is smaller for a bulge ($n = 4$). We conclude that SDSS J1200+4014 is probably an S0 or an elliptical galaxy.

J1455+5304

In all bands the χ^2 of the fit is smaller for a bulge ($n = 4$). We conclude that SDSS J1455+5304 is probably an S0 or an elliptical galaxy.

3.4 Mass-to-light ratios

We compute estimates of the total M/L ratios for the gravitational lenses we have discovered. This is realized assuming a point mass lens (§ 3.1.2) to deduce the total mass within the Einstein radius, and computing the luminosity within the Einstein radius using a Sérsic profile (Graham & Driver 2005). Our images are calibrated using the SDSS database magnitudes, and K-correction is applied following Oke & Sandage (1968). The results are presented in Table 3.5. However, these values are difficult to compare to usual M/L ratios, as they probe the total mass and not just the stellar or baryonic matter.

In the case of the S0 or elliptical galaxy lens J1455+5304, the Einstein radius is small ($r_E = 0.7 \pm 0.4''$), so we can expect that the mass probed within is largely dominated by baryons. On this basis, the $M_{\rm tot}/L_I = 1.5 \pm 0.9$ for J1455+5304 we obtain is consistent with the value from Trott & Webster (2002) of $M/L_I = 1.1 \pm 0.2$ for the disk of the Sab spiral lens the Einstein Cross.

In the case of the (probable disk-galaxy) lens J0812+5436, we obtain a particularly high M/L ratio, with $M_{\rm tot}/L_I = 5.4 \pm 1.5$. The Einstein radius is larger than expected for galaxy-galaxy lensing systems, with $r_E = 1.8 \pm 0.4''$. The total mass within might contain a large amount of DM, although it is still in the few central kiloparsecs of the galaxy. We note that J0812+5436 is surrounded by four galaxies at a similar redshift in a radius ~ 150 kpc. This group of galaxies may add to the gravitational potential deflecting the background source.

The limited observational precision that we obtain on measuring the Einstein radius and the surface brightness of the different components of the galaxies limits us in the study of the M/L ratios of these new galaxy-galaxy lenses. Therefore, we can not gain insight on the M/L ratios of the different components, nor constrain the shape of the IMF or the maximum disk hypothesis. High resolution imaging such as with *HST* is required to further study the M/L ratio of these lens galaxies.

Table 3.6. *Results*

Name	Type	Morphology
J0812+5436	strong lens	probably disk
J0903+5448	unknown	disk
J0942+6111	unknown	disk
J1150+1202	probably strong lens	probably S0
J1200+4014	probably strong lens	S0 or elliptical
J1356+5615	unknown	disk
J1455+5304	strong lens	S0 or elliptical
J1625+2818	unknown	spiral

3.5 Discussion

The results of the follow-up of the eight disk-galaxy gravitational lens candidates are summarized in Table 3.6. From the optical imaging and spectroscopy presented here, we can determine clearly that two systems are strong gravitational lenses, J0812+5436 being a probable disk or S0 galaxy, and J1455+5304 being a S0 or elliptical galaxy.

Concerning the other candidates, we classify as probable gravitational lenses those systems in which we find indication of multiple imaging from both imaging and spectroscopy, although observations do not allow us a complete confirmation of the lens nature of the system. We find two probable gravitational lenses, J1150+1202 being probably a S0 galaxy, and J1200+4014 being a S0 or elliptical galaxy.

Finally, we classify as unknown the systems for which we found indication of multiple imaging in optical observations, but could not confirm the presence of multiple images in the spectroscopy. These systems are good lens candidates but the quality of our observations did not allow us to conclude on their nature. In this category, we find J0903+5448, J0942+6111, and J1356+5615 which are disk dominated galaxies, as well as the spiral galaxy J1625+2818.

We see that for most of the gravitational lens candidates, our combined photometric and spectroscopic observations are not sufficient to determine clearly the presence of multiple images of the background source. This is due mainly to the fact that the images of the background source are very near to the center of the foreground galaxy, the Einstein radius being expected to be of the order of $\sim 1''$. Therefore, ground-based observations suffer from seeing conditions for such a study. Moreover, some of the images might be obscured by dust in disk galaxies.

Confirmation of the remaining lens candidates will require either high resolution spatially-resolved spectroscopy, or high resolution imaging. Integral field spectroscopy would allow us to probe both the presence of multiple images of a background source and the configuration of the lensed images. However, because the galaxies in our study are candidate massive disk galaxies, they are not expected to present much structures in the blue part

of the spectrum, which would be mistaken for lensed images. In the case of the spiral lens J1625+2818, the position of the potential lensed images around the bulge also prevented any contamination by the arms for detecting the potential lensed images. Therefore, *HST* imaging might be the best choice for at the same time confirming the genuine lens nature of our disk-galaxy lens candidates, confirming the disk nature of our new gravitational lenses, and studying the mass distribution of these systems.

In the following we present suggestions for improving the efficiency of a search and for enlarging the size of the survey.

1- Due to the very large number of galaxies in the SDSS Main Galaxy Sample, we covered only a part of the color parameter space corresponding to disk galaxies. We chose to limit ourselves to the region containing early-type disk galaxies, which are massive disk galaxies and therefore better suited our purpose. A larger survey should span all of the disk galaxy color range (applying a suitable r magnitude criterion to select massive galaxies), although this would largely increase the size of the initial galaxy sample.

2- The automated method we used to select spectra showing evidence for a background galaxy along the line of sight is based on a S/N ratio per pixel emission-line detection. This was done in order to select bright peaks in the spectra. A complete search should be based on an integrated S/N ratio selection to detect and identify all background emission lines.

3- We did not cover the redshift range $z < 0.1$, as very few lenses are expected at such a low redshift. However, half of the galaxies in the SDSS Main Sample lie in this region, so it would be of interest to explore it also.

4- Selecting lens candidates based on the presence of three emission lines limits, in the case of the SDSS, the redshift of the background galaxy to $z < 0.8$. Selection based on one detected emission line and its identification as the [O II] $\lambda\lambda$3727 doublet, as in the OLS-survey (Willis et al. 2005, 2006), would allow us to enlarge the sample of lens candidates. Indeed, almost all our gravitational lens candidates have a resolved [O II] $\lambda\lambda$3727 doublet.

5- Among the SLACS lenses, some late-type galaxy lenses were found (Bolton et al. 2008), although they were targeting red early-type galaxies. This happens when the bulge in the

disk galaxy is prominent, and therefore this should be taken into account when searching for the disk galaxy population in other large surveys.

3.6 Conclusion

In this chapter was presented the first automated search for disk-galaxy gravitational lenses using the SDSS database, and proved the feasibility of such a project with the discovery of a galaxy-galaxy lens which is very probably a disk, of four interesting disk-galaxy lens candidates, and three confirmed or probable lenses which may be S0 galaxies. *HST* images will be needed to further study the systems presented in this work, particularly to probe the presence of a disk in the lens galaxy of J0812+5436 and study its mass distribution, as well as to confirm the lens nature of the interesting disk-galaxy lens candidates we discovered.

This project is the first step in finding more disk-galaxy lenses in the SDSS, and possibly in other large surveys. To date, only seven disk-galaxy lenses are known. Assembling a larger sample of disk-galaxy lenses would open up promising perspectives for measuring the M/L ratios of disks and bulges. This would allow to improve our understanding of the structure and stellar population of disk galaxies, as well as to gain insights into a possible source of the TF zero point problem, which challenges the ΛCDM model.

Chapter 4

Conclusions

This thesis presented two studies realized in a same idea: investigating ways to gain insights and physical understanding into the problems that ΛCDM faces at galactic scales.

A possible approach to understanding the cusp-core problem is tested in Chapter 2. Predictions of nonextensive statistical mechanics are tested against simulated DM halos, in the hope that this formalism can provide a theoretical description of DM halo structures, and particularly of their inner parts, from first principles. Unfortunately, a careful study leads to the conclusion that nonextensive statistical mechanics is unable to describe the structure of DM halos. This result points at the need to reconsider the formalism in its simplest form, and leaves the theoretical prediction of DM halo structures an open question.

The TF relation zero point problem has a possible origin in the generalization of the MW IMF to other disk galaxies. The shape of the IMF can be constrained using the M/L ratios of disk galaxies. Gravitational lensing provides a promising way to measure independently the M/L ratios of disk galaxies, but for the scarcity of disk-galaxy lens discoveries. In Chapter 3 is presented an automated search for disk-galaxy lens candidates, as well as imaging and long-slit spectroscopy of eight disk-galaxy lens candidates. Although the study is limited by the resolution of observations to completely probe the nature of the candidates, the discovery of two new gravitational lenses including a very probable disk galaxy and a probable S0 galaxy, as well as the confirmation that at least four other systems are interesting disk-galaxy lens candidates, are promising results to increase the number of known disk galaxy lenses. High resolution imaging is needed to further study these systems, be it to confirm the disk nature of the confirmed gravitational lenses, or

the lens nature of the disk-galaxies, and for measuring their M/L ratio. This study opens promising perspectives to gain further insights into the structure of disk galaxies, and their baryonic and dark matter distributions.

Appendix A

Nonextensive statistical mechanics: stellar polytropes in the old and new formalisms

In this Appendix are presented some details on the derivation of stellar polytropes (SPs) distribution function from nonextensive statistical mechanics, in both old and new formalisms.

Astrophysical self-gravitating systems are described by the distribution function $f(\mathbf{x},\mathbf{v})$, where $\mathbf{x}$ and $\mathbf{v}$ are the position and the velocity of each particle, and $d^6\tau$ is the six-dimensional phase-space element. ϕ is the gravitational potential.

A.1 Old formalism

The generalized entropy S_q reads as

$$S_q = -\frac{1}{q-1}\int (f(\mathbf{x},\mathbf{v})^q - f(\mathbf{x},\mathbf{v}))d^6\tau. \tag{A.1}$$

It can be extremized at fixed mass and energy using Lagrange multipliers (Plastino & Plastino 1993):

$$\delta S - \alpha\delta M - \beta\delta E = 0. \tag{A.2}$$

The total mass of the system reads as

$$M = \int f(\mathbf{x},\mathbf{v})d^6\tau \tag{A.3}$$

and the total energy as

$$E = \int \frac{1}{2}(v^2 + \phi) f(\mathbf{x},\mathbf{v}) d^6\tau. \tag{A.4}$$

This leads to

$$f(\mathbf{x},\mathbf{v}) \propto \epsilon^{1/(q-1)}, \tag{A.5}$$

where ϵ is the relative energy per unit mass.

This is a distribution function similar to the one of SPs (Binney & Tremaine 1987)

$$f(\mathbf{x},\mathbf{v}) \propto \epsilon^{n-3/2} \quad (\epsilon > 0), \tag{A.6}$$

$$f(\mathbf{x},\mathbf{v}) = 0 \quad (\epsilon \leq 0), \tag{A.7}$$

when identifying the polytropic index n as

$$n = \frac{3}{2} + \frac{1}{q-1}. \tag{A.8}$$

A.2 New formalism

In a newer version of the theory (Tsallis et al. 1998), the fundamental quantity describing the system is not the distribution function $f(\mathbf{x},\mathbf{v})$ anymore, but the probability function $p(\mathbf{x},\mathbf{v})$. All macroscopic quantities can be expressed with the escort probability distribution, defined as

$$P_q(\mathbf{x},\mathbf{v}) = \frac{p(\mathbf{x},\mathbf{v})^q}{\int p(\mathbf{x},\mathbf{v})^q d^6\tau}, \tag{A.9}$$

in the following way:

$$< O_i >_q = \int O_i P_q(\mathbf{x},\mathbf{v}) d^6\tau. \tag{A.10}$$

In the new formalism, the generalized entropy of eq. 2.2 is function of the fundamental probability function $p(\mathbf{x},\mathbf{v})$:

$$S_q = -\frac{1}{q-1} \int (p(\mathbf{x},\mathbf{v})^q - p(\mathbf{x},\mathbf{v})) d^6\tau. \tag{A.11}$$

This time again, the generalized entropy S_q is extremized to find the equilibrium distribution function f(**x**,**v**) of the system, but for this the relation between f(**x**,**v**) and p(**x**,**v**) is needeed. Eq. A.10 applied to the total mass leads to

$$< M >_q = \int f(\mathbf{x},\mathbf{v}) d^6\tau = \int M P_q(\mathbf{x},\mathbf{v}) d^6\tau, \tag{A.12}$$

that is,

$$f(\mathbf{x},\mathbf{v}) = M P_q(\mathbf{x},\mathbf{v}) = M \frac{p(\mathbf{x},\mathbf{v})^q}{\int p(\mathbf{x},\mathbf{v})^q d^6\tau}. \tag{A.13}$$

This relation already constrains the total mass of the system. Therefore, the constraints used for the maximization are the total energy from eq. A.4, and the normalization of the probability function $\int p(\mathbf{x},\mathbf{v}) d^6\tau = 1$.

Once more the Lagrange multipliers method is applied to find the maximum entropy state of the system (Taruya & Sakagami 2003):

$$\delta S_q - \alpha\delta \int p(\mathbf{x},\mathbf{v}) d^6\tau - \beta\delta \int \frac{1}{2}(v^2 + \phi) f(\mathbf{x},\mathbf{v}) d^6\tau = 0, \tag{A.14}$$

the derivation being with respect to p(**x**,**v**).

This leads to an equilibrium distribution function

$$f(\mathbf{x},\mathbf{v}) \propto \epsilon^{q/(1-q)}. \tag{A.15}$$

It is still of the form of SPs, with this time

$$n = \frac{1}{2} + \frac{1}{1-q}. \tag{A.16}$$

Appendix B

Gravitational potential and density slope at the origin in stellar polytropes

In this Appendix are presented two demonstrations which combination proves that only stellar polytropes with zero density slope at the center have a finite gravitational potential at the origin.

B.1 Relation between density and slope at the origin

Solutions of the Lane-Emden equation which are finite at the origin necessarily have $d\theta/d\xi = 0$ *at* $\xi = 0$.

The following demonstration is based on Chandrasekhar (1939).

PROOF: The Lane-Emden equation is

$$\frac{1}{\xi}\frac{d}{d\xi}\left(\xi^2\frac{d\theta}{d\xi}\right) = -\theta^n, \tag{B.1}$$

with θ the normalized density and ξ the normalized radius. Defining a new variable

$$\chi = \theta\xi, \tag{B.2}$$

the Lane-Emden equation becomes

$$\frac{d^2\chi}{d\xi^2} = -\frac{\chi^n}{\xi^{n-1}}. \tag{B.3}$$

We consider the solutions of the Lane-Emden equation which are finite at the origine:

$$(\theta = finite, \xi = 0) \rightarrow (\chi = \xi\theta = 0, \xi = 0). \tag{B.4}$$

These are solutions of $\chi(\xi)$ passing through the origin. We can expand them:

$$\chi(\xi) = \xi \left(\frac{d\chi}{d\xi}\right)_{\xi=0} + \frac{\xi^2}{2}\left(\frac{d^2\chi}{d\xi^2}\right)_{\xi=0} + \cdots, \tag{B.5}$$

$$\frac{d\chi}{d\xi} = \left(\frac{d\chi}{d\xi}\right)_{\xi=0} + \xi\left(\frac{d^2\chi}{d\xi^2}\right)_{\xi=0} + \cdots. \tag{B.6}$$

Now we want to calculate the density slope as a function of χ and find its value at the origin.

$$\frac{d\theta}{d\xi} = \frac{1}{\xi}\frac{d\chi}{d\xi} - \frac{\chi}{\xi^2}, \tag{B.7}$$

$$\left(\frac{d\theta}{d\xi}\right)_{\xi=0} = \lim_{\xi=0}\left[\frac{1}{\xi}\frac{d\chi}{d\xi} - \frac{\chi}{\xi^2}\right]. \tag{B.8}$$

Replacing $\chi(\xi)$ and $\frac{d\chi}{d\xi}$ in the last expression, and using that $\chi = 0$ at $\xi = 0$, leads to

$$\left(\frac{d\theta}{d\xi}\right)_{\xi=0} = \lim_{\xi=0}\left[-\frac{1}{2}\left(\frac{\chi}{\xi}\right)^{n-1}\chi\right] = 0. \tag{B.9}$$

B.2 Relation between gravitational potential and density

For stellar polytropes the matter density ρ and the relative gravitational potential ψ are linked by $\rho = c_n\psi^n$ where c_n is a constant depending on the polytropic index n.

The following demonstration is based on Binney & Tremaine (1987).

PROOF: The distribution function of stellar polytropes reads as

$$f(\epsilon) \propto \epsilon^{n-\frac{3}{2}}. \tag{B.10}$$

Then the matter density is

$$\rho = 4\pi \int f(\psi - \frac{1}{2}v^2)v^2 dv \propto \int (\psi - \frac{1}{2}v^2)^{n-\frac{3}{2}} v^2 dv, \tag{B.11}$$

where $\psi = -\phi + \phi_0$ is the relative potential, ϕ_0 a constant, and $\epsilon = \psi - \frac{1}{2}v^2$ is the relative energy.

Substitution:

$$v^2 = 2\psi \cos^2\theta, \tag{B.12}$$

$$dv = -\frac{\sin 2\theta}{v} d\theta d\psi = \mp \frac{\sin 2\theta}{\sqrt{2\psi}\cos\theta} d\theta d\psi, \quad (\psi > 0). \tag{B.13}$$

The matter density becomes

$$\rho \propto \int (\psi - \psi\cos^2\theta)^{n-\frac{3}{2}} \times 2\psi\cos^2\theta \times \frac{\sin 2\theta}{\sqrt{2\psi}\cos\theta} d\theta d\psi, \tag{B.14}$$

$$\rho \propto \int \psi^{n-1} d\psi \int \sin^{2n-3}\theta \sin 2\theta \cos\theta d\theta, \tag{B.15}$$

$$\rho \propto \psi^n \int g(\theta, n) d\theta, \tag{B.16}$$

$$\rho = c_n \psi^n. \tag{B.17}$$

Appendix C

Statement of coauthorship

This Appendix lists papers in which work presented in this thesis is included, and for each of them is given the detail of my contribution.

C.1 Paper I

Simulated Dark-Matter Halos as a Test of Nonextensive Statistical Mechanics

by

C. Féron & J. Hjorth

Physical Review E 77, 022106 (2008)

C. Féron wrote the paper. She also computed numerically the radial profiles presented in Figure 1, made Figure 1, and did all the analysis. The idea for this paper was provided by J. Hjorth, as well as comments and advice.

Chloé Féron Jens Hjorth

C.2 Paper II

A Search for Disk-Galaxy Lenses in the Sloan Digital Sky Survey

by

C. Féron, J. Hjorth, J. P. McKean & J. Samsing

Submitted to *The Astrophysical Journal*

C. Féron wrote the paper. She defined and selected the sample of disk-galaxy lens candidates. She wrote the proposal to obtain observing time for studying the disk-galaxy lens candidates. She went observing the targets at the Nordic Optical Telescope, both for the imaging and the spectroscopy. She reduced all the data, and did most of the data analysis. She also computed the mass-to-light ratios of the confirmed gravitational lenses, and made all the figures in the paper. J. Samsing developed part of the software used to select the lens candidates among the sample of candidate massive disk galaxies. J. P. McKean participated to the data reduction by teaching C. Féron to reduce long-slit spectroscopy data. He also analyzed independently part of the spectroscopic data for cross-checking the results. The idea for this paper was provided by J. Hjorth, as well as comments and advice.

Chloé Féron Jens Hjorth

Bibliography

Adelman-McCarthy, J. K., Agüeros, M. A., Allam, S. S., Anderson, K. S. J., Anderson, S. F., Annis, J., Bahcall, N. A., Bailer-Jones, C. A. L., Baldry, I. K., Barentine, J. C., Beers, T. C., Belokurov, V., Berlind, A., Bernardi, M., Blanton, M. R., Bochanski, J. J., Boroski, W. N., Bramich, D. M., Brewington, H. J., Brinchmann, J., Brinkmann, J., Brunner, R. J., Budavári, T., Carey, L. N., Carliles, S., Carr, M. A., Castander, F. J., Connolly, A. J., Cool, R. J., Cunha, C. E., Csabai, I., Dalcanton, J. J., Doi, M., Eisenstein, D. J., Evans, M. L., Evans, N. W., Fan, X., Finkbeiner, D. P., Friedman, S. D., Frieman, J. A., Fukugita, M., Gillespie, B., Gilmore, G., Glazebrook, K., Gray, J., Grebel, E. K., Gunn, J. E., de Haas, E., Hall, P. B., Harvanek, M., Hawley, S. L., Hayes, J., Heckman, T. M., Hendry, J. S., Hennessy, G. S., Hindsley, R. B., Hirata, C. M., Hogan, C. J., Hogg, D. W., Holtzman, J. A., Ichikawa, S.-i., Ichikawa, T., Ivezić, Ž., Jester, S., Johnston, D. E., Jorgensen, A. M., Jurić, M., Kauffmann, G., Kent, S. M., Kleinman, S. J., Knapp, G. R., Kniazev, A. Y., Kron, R. G., Krzesinski, J., Kuropatkin, N., Lamb, D. Q., Lampeitl, H., Lee, B. C., Leger, R. F., Lima, M., Lin, H., Long, D. C., Loveday, J., Lupton, R. H., Mandelbaum, R., Margon, B., Martínez-Delgado, D., Matsubara, T., McGehee, P. M., McKay, T. A., Meiksin, A., Munn, J. A., Nakajima, R., Nash, T., Neilsen, E. H., Jr., Newberg, H. J., Nichol, R. C., Nieto-Santisteban, M., Nitta, A., Oyaizu, H., Okamura, S., Ostriker, J. P., Padmanabhan, N., Park, C., Peoples, J. J., Pier, J. R., Pope, A. C., Pourbaix, D., Quinn, T. R., Raddick, M. J., Re Fiorentin, P., Richards, G. T.,

Richmond, M. W., Rix, H.-W., Rockosi, C. M., Schlegel, D. J., Schneider, D. P., Scranton, R., Seljak, U., Sheldon, E., Shimasaku, K., Silvestri, N. M., Smith, J. A., Smolčić, V., Snedden, S. A., Stebbins, A., Stoughton, C., Strauss, M. A., SubbaRao, M., Suto, Y., Szalay, A. S., Szapudi, I., Szkody, P., Tegmark, M., Thakar, A. R., Tremonti, C. A., Tucker, D. L., Uomoto, A., Vanden Berk, D. E., Vandenberg, J., Vidrih, S., Vogeley, M. S., Voges, W., Vogt, N. P., Weinberg, D. H., West, A. A., White, S. D. M., Wilhite, B., Yanny, B., Yocum, D. R., York, D. G., Zehavi, I., Zibetti, S., & Zucker, D. B. (2007). The Fifth Data Release of the Sloan Digital Sky Survey. *ApJS*, *172*, 634–644.

Austin, C. G., Williams, L. L. R., Barnes, E. I., Babul, A., & Dalcanton, J. J. (2005). Semianalytical Dark Matter Halos and the Jeans Equation. *ApJ*, *634*, 756–774.

Barnes, E. I., Williams, L. L. R., Babul, A., & Dalcanton, J. J. (2007). Velocity Distributions from Nonextensive Thermodynamics. *ApJ*, *655*, 847–850.

Bell, E. F., & de Jong, R. S. (2001). Stellar Mass-to-Light Ratios and the Tully-Fisher Relation. *ApJ*, *550*, 212–229.

Bielby, R. M., & Shanks, T. (2007). Anomalous SZ contribution to three-year WMAP data. *MNRAS*, *382*, 1196–1202.

Binney, J., & Tremaine, S. (1987). *Galactic dynamics*. Princeton, NJ, Princeton University Press, 1987, 747 p.

Bolton, A. S., Burles, S., Koopmans, L. V. E., Treu, T., Gavazzi, R., Moustakas, L. A., Wayth, R., & Schlegel, D. J. (2008). The Sloan Lens ACS Survey. V. The Full ACS Strong-Lens Sample. *ApJ*, *682*, 964–984.

Bolton, A. S., Burles, S., Koopmans, L. V. E., Treu, T., & Moustakas, L. A. (2006). The Sloan Lens ACS Survey. I. A Large Spectroscopically Selected Sample of Massive Early-Type Lens Galaxies. *ApJ*, *638*, 703–724.

Bolton, A. S., Burles, S., Schlegel, D. J., Eisenstein, D. J., & Brinkmann, J. (2004). Sloan Digital Sky Survey Spectroscopic Lens Search. I. Discovery of Intermediate-Redshift Star-forming Galaxies behind Foreground Luminous Red Galaxies. *AJ*, *127*, 1860–1882.

Bonamente, M., Joy, M. K., LaRoque, S. J., Carlstrom, J. E., Reese, E. D., & Dawson, K. S. (2006). Determination of the Cosmic Distance Scale from Sunyaev-Zel'dovich Effect and Chandra X-Ray Measurements of High-Redshift Galaxy Clusters. *ApJ*, *647*, 25–54.

Burkert, A. (1995). The Structure of Dark Matter Halos in Dwarf Galaxies. *ApJ*, *447*, L25+.

Castander, F. J., Treister, E., Maza, J., & Gawiser, E. (2006). CXOCY J220132.8-320144: An Edge-on Spiral Gravitational Lens. *ApJ*, *652*, 955–962.

Chandrasekhar, S. (1939). *An introduction to the study of stellar structure*. Chicago, Ill., The University of Chicago press [1939].

Courteau, S., Dutton, A. A., van den Bosch, F. C., MacArthur, L. A., Dekel, A., McIntosh, D. H., & Dale, D. A. (2007). Scaling Relations of Spiral Galaxies. *ApJ*, *671*, 203–225.

Covone, G., Paolillo, M., Napolitano, N. R., Capaccioli, M., Longo, G., Kneib, J. P., Jullo, E., Richard, J., Khovanskaya, O., Sazhin, M., Grogin, N. A., & Schreier, E. (2008). Gauging the dark matter fraction in a L* S0 galaxy at z=0.47 through gravitational lensing from deep HST/ACS imaging. *ArXiv e-prints*, `http://lanl.arxiv.org/abs/0809.4125`.

de Blok, W. J. G., & Bosma, A. (2002). High-resolution rotation curves of low surface brightness galaxies. *A&A*, *385*, 816–846.

de Jong, R. S., & Bell, E. F. (2007). *Comparing Dynamical and Stellar Population Mass-To-Light Ratio Estimates*, (pp. 107–+). Island Universes - Structure and Evolution of Disk Galaxies.

Dehnen, W., & McLaughlin, D. E. (2005). Dynamical insight into dark matter haloes. *MNRAS*, *363*, 1057–1068.

Dutton, A. A., van den Bosch, F. C., Dekel, A., & Courteau, S. (2007). A Revised Model for the Formation of Disk Galaxies: Low Spin and Dark Halo Expansion. *ApJ*, *654*, 27–52.

Faure, C., Kneib, J.-P., Covone, G., Tasca, L., Leauthaud, A., Capak, P., Jahnke, K., Smolcic, V., de la Torre, S., Ellis, R., Finoguenov, A., Koekemoer, A., Le Fevre, O., Massey, R., Mellier, Y., Refregier, A., Rhodes, J., Scoville, N., Schinnerer, E., Taylor, J., Van Waerbeke, L., &

Walcher, J. (2008). First Catalog of Strong Lens Candidates in the COSMOS Field. *ApJS*, *176*, 19–38.

Flynn, C., Holmberg, J., Portinari, L., Fuchs, B., & Jahreiß, H. (2006). On the mass-to-light ratio of the local Galactic disc and the optical luminosity of the Galaxy. *MNRAS*, *372*, 1149–1160.

Freedman, W. L., Madore, B. F., Gibson, B. K., Ferrarese, L., Kelson, D. D., Sakai, S., Mould, J. R., Kennicutt, R. C., Jr., Ford, H. C., Graham, J. A., Huchra, J. P., Hughes, S. M. G., Illingworth, G. D., Macri, L. M., & Stetson, P. B. (2001). Final Results from the Hubble Space Telescope Key Project to Measure the Hubble Constant. *ApJ*, *553*, 47–72.

Fukugita, M., Shimasaku, K., & Ichikawa, T. (1995). Galaxy Colors in Various Photometric Band Systems. *PASP*, *107*, 945–+.

Gentile, G., Salucci, P., Klein, U., Vergani, D., & Kalberla, P. (2004). The cored distribution of dark matter in spiral galaxies. *MNRAS*, *351*, 903–922.

Gnedin, O. Y., Weinberg, D. H., Pizagno, J., Prada, F., & Rix, H.-W. (2007). Dark Matter Halos of Disk Galaxies: Constraints from the Tully-Fisher Relation. *ApJ*, *671*, 1115–1134.

Governato, F., Mayer, L., Wadsley, J., Gardner, J. P., Willman, B., Hayashi, E., Quinn, T., Stadel, J., & Lake, G. (2004). The Formation of a Realistic Disk Galaxy in Λ-dominated Cosmologies. *ApJ*, *607*, 688–696.

Governato, F., Willman, B., Mayer, L., Brooks, A., Stinson, G., Valenzuela, O., Wadsley, J., & Quinn, T. (2007). Forming disc galaxies in ΛCDM simulations. *MNRAS*, *374*, 1479–1494.

Graham, A. W., & Driver, S. P. (2005). A Concise Reference to (Projected) Sérsic $R^{1/n}$ Quantities, Including Concentration, Profile Slopes, Petrosian Indices, and Kron Magnitudes. *Publications of the Astronomical Society of Australia*, *22*, 118–127.

Graham, A. W., Merritt, D., Moore, B., Diemand, J., & Terzić, B. (2006). Empirical Models for Dark Matter Halos. II. Inner Profile Slopes, Dynamical Profiles, and ρ/σ^3. *AJ*, *132*, 2701–2710.

Hansen, S. H. (2004). Dark matter density profiles from the Jeans equation. *MNRAS*, *352*, L41–L43.

Hansen, S. H., Egli, D., Hollenstein, L., & Salzmann, C. (2005). Dark matter distribution function from non-extensive statistical mechanics. *New Astronomy*, *10*, 379–384.

Hansen, S. H., & Moore, B. (2006). A universal density slope Velocity anisotropy relation for relaxed structures. *New Astronomy*, *11*, 333–338.

Hansen, S. H., Moore, B., Zemp, M., & Stadel, J. (2006). A universal velocity distribution of relaxed collisionless structures. *Journal of Cosmology and Astro-Particle Physics*, *1*, 14–+.

Hayashi, E., Navarro, J. F., & Springel, V. (2007). The shape of the gravitational potential in cold dark matter haloes. *MNRAS*, *377*, 50–62.

Hernquist, L. (1990). An analytical model for spherical galaxies and bulges. *ApJ*, *356*, 359–364.

Hjorth, J., & Madsen, J. (1991). Violent relaxation and the R exp 1/4 law. *MNRAS*, *253*, 703–709.

Hogg, D. W. (1999). Distance measures in cosmology. *ArXiv e-prints*, `http://lanl.arxiv.org/abs/astro-ph/9905116`.

Huchra, J., Gorenstein, M., Kent, S., Shapiro, I., Smith, G., Horine, E., & Perley, R. (1985). 2237 + 0305 - A new and unusual gravitational lens. *AJ*, *90*, 691–696.

Huss, A., Jain, B., & Steinmetz, M. (1999). How Universal Are the Density Profiles of Dark Halos? *ApJ*, *517*, 64–69.

Jaunsen, A. O., & Hjorth, J. (1997). Detection of a spiral lens galaxy and optical variability in the gravitational lens system B1600+434. *A&A*, *317*, L39–L42.

Jiulin, D. (2006). What Does the Nonextensive Parameter Stand for in Self-Gravitating Systems? *Ap&SS*, *305*, 247–251.

Kassin, S. A., de Jong, R. S., & Weiner, B. J. (2006). Dark and Baryonic Matter in Bright Spiral Galaxies. II. Radial Distributions for 34 Galaxies. *ApJ*, *643*, 804–824.

Keeton, C. R., & Kochanek, C. S. (1998). Gravitational Lensing by Spiral Galaxies. *ApJ*, *495*, 157–+.

Komatsu, E., Dunkley, J., Nolta, M. R., Bennett, C. L., Gold, B., Hinshaw, G., Jarosik, N., Larson, D., Limon, M., Page, L., Spergel, D. N., Halpern, M., Hill, R. S., Kogut, A., Meyer, S. S., Tucker, G. S., Weiland, J. L., Wollack, E., & Wright, E. L. (2008). Five-Year Wilkinson Microwave Anisotropy Probe (WMAP) Observations: Cosmological Interpretation. *ArXiv e-prints*, `http://lanl.arxiv.org/abs/0803.0547`.

Koopmans, L. V. E., de Bruyn, A. G., & Jackson, N. (1998). The edge-on spiral gravitational lens B1600+434. *MNRAS*, *295*, 534–+.

Koopmans, L. V. E., Treu, T., Bolton, A. S., Burles, S., & Moustakas, L. A. (2006). The Sloan Lens ACS Survey. III. The Structure and Formation of Early-Type Galaxies and Their Evolution since z $\sim$ 1. *ApJ*, *649*, 599–615.

Kronberger, T., Leubner, M. P., & van Kampen, E. (2006). Dark matter density profiles: a comparison of nonextensive theory with N-body simulations. *A&A*, *453*, 21–25.

Leubner, M. P. (2005). Nonextensive Theory of Dark Matter and Gas Density Profiles. *ApJ*, *632*, L1–L4.

Lieu, R., Mittaz, J. P. D., & Zhang, S.-N. (2006). The Sunyaev-Zel'dovich Effect in a Sample of 31 Clusters: A Comparison between the X-Ray Predicted and WMAP Observed Cosmic Microwave Background Temperature Decrement. *ApJ*, *648*, 176–199.

Lynden-Bell, D. (1967). Statistical mechanics of violent relaxation in stellar systems. *MNRAS*, *136*, 101–+.

Maller, A. H., Simard, L., Guhathakurta, P., Hjorth, J., Jaunsen, A. O., Flores, R. A., & Primack, J. R. (2000). Breaking the Disk/Halo Degeneracy with Gravitational Lensing. *ApJ*, *533*, 194–202.

Medvedev, M. V., & Rybicki, G. (2001). The Structure of Self-gravitating Polytropic Systems with n around 5. *ApJ*, *555*, 863–867.

Merritt, D., Navarro, J. F., Ludlow, A., & Jenkins, A. (2005). A Universal Density Profile for Dark and Luminous Matter? *ApJ*, *624*, L85–L88.

Möller, O., Kitzbichler, M., & Natarajan, P. (2007). Strong lensing statistics in large, $z < 0.2$, surveys: bias in the lens galaxy population. *MNRAS*, *379*, 1195–1208.

Moore, B., Governato, F., Quinn, T., Stadel, J., & Lake, G. (1998). Resolving the Structure of Cold Dark Matter Halos. *ApJ*, *499*, L5+.

Moore, B., Quinn, T., Governato, F., Stadel, J., & Lake, G. (1999). Cold collapse and the core catastrophe. *MNRAS*, *310*, 1147–1152.

Navarro, J. F., Frenk, C. S., & White, S. D. M. (1996). The Structure of Cold Dark Matter Halos. *ApJ*, *462*, 563–+.

Navarro, J. F., Frenk, C. S., & White, S. D. M. (1997). A Universal Density Profile from Hierarchical Clustering. *ApJ*, *490*, 493–+.

Navarro, J. F., Hayashi, E., Power, C., Jenkins, A. R., Frenk, C. S., White, S. D. M., Springel, V., Stadel, J., & Quinn, T. R. (2004). The inner structure of ΛCDM haloes - III. Universality and asymptotic slopes. *MNRAS*, *349*, 1039–1051.

Navarro, J. F., & Steinmetz, M. (2000a). Dark Halo and Disk Galaxy Scaling Laws in Hierarchical Universes. *ApJ*, *538*, 477–488.

Navarro, J. F., & Steinmetz, M. (2000b). The Core Density of Dark Matter Halos: A Critical Challenge to the ΛCDM Paradigm? *ApJ*, *528*, 607–611.

Oke, J. B., & Sandage, A. (1968). Energy Distributions, K Corrections, and the Stebbins-Whitford Effect for Giant Elliptical Galaxies. *ApJ*, *154*, 21–+.

Patnaik, A. R., Browne, I. W. A., King, L. J., Muxlow, T. W. B., Walsh, D., & Wilkinson, P. N. (1992). 0218+357: The Smallest Separation Lensed System. In R. Kayser, T. Schramm, & L. Nieser (Eds.) *Gravitational Lenses*, vol. 406 of *Lecture Notes in Physics, Berlin Springer Verlag*, (pp. 140–+).

Peng, C. Y., Ho, L. C., Impey, C. D., & Rix, H.-W. (2002). Detailed Structural Decomposition of Galaxy Images. *AJ*, *124*, 266–293.

Percival, W. J., Nichol, R. C., Eisenstein, D. J., Frieman, J. A., Fukugita, M., Loveday, J., Pope, A. C., Schneider, D. P., Szalay, A. S., Tegmark, M., Vogeley, M. S., Weinberg, D. H., Zehavi, I., Bahcall, N. A., Brinkmann, J., Connolly, A. J., & Meiksin, A. (2007). The Shape of the Sloan Digital Sky Survey Data Release 5 Galaxy Power Spectrum. *ApJ*, *657*, 645–663.

Plastino, A. R., & Plastino, A. (1993). Stellar polytropes and Tsallis' entropy. *Physics Letters A*, *174*, 384–386.

Pointecouteau, E., Arnaud, M., & Pratt, G. W. (2005). The structural and scaling properties of nearby galaxy clusters. I. The universal mass profile. *A&A*, *435*, 1–7.

Portinari, L., & Sommer-Larsen, J. (2007). The Tully-Fisher relation and its evolution with redshift in cosmological simulations of disc galaxy formation. *MNRAS*, *375*, 913–924.

Portinari, L., Sommer-Larsen, J., & Tantalo, R. (2004). On the mass-to-light ratio and the initial mass function in disc galaxies. *MNRAS*, *347*, 691–719.

Robertson, B., Yoshida, N., Springel, V., & Hernquist, L. (2004). Disk Galaxy Formation in a Λ Cold Dark Matter Universe. *ApJ*, *606*, 32–45.

Salucci, P., Lapi, A., Tonini, C., Gentile, G., Yegorova, I., & Klein, U. (2007). The universal rotation curve of spiral galaxies - II. The dark matter distribution out to the virial radius. *MNRAS*, *378*, 41–47.

Salucci, P., & Persic, M. (1999). Maximal halos in high-luminosity spiral galaxies. *A&A*, *351*, 442–446.

Salucci, P., Yegorova, I. A., & Drory, N. (2008). The disc mass of spiral galaxies. *MNRAS*, *388*, 159–164.

Sandage, A., Tammann, G. A., Saha, A., Reindl, B., Macchetto, F. D., & Panagia, N. (2006). The Hubble Constant: A Summary of the Hubble Space Telescope Program for the Luminosity Calibration of Type Ia Supernovae by Means of Cepheids. *ApJ*, *653*, 843–860.

Sellwood, J. A. (2008). Bar-Halo Friction in Galaxies. III. Halo Density Changes. *ApJ*, *679*, 379–396.

Sérsic, J. L. (1963). Influence of the atmospheric and instrumental dispersion on the brightness distribution in a galaxy. *Boletin de la Asociacion Argentina de Astronomia La Plata Argentina*, *6*, 41–+.

Sérsic, J. L. (1968). *Atlas de galaxias australes*. Cordoba, Argentina: Observatorio Astronomico, 1968.

Shin, E. M., & Evans, N. W. (2007). The Milky Way Galaxy as a strong gravitational lens. *MNRAS*, *374*, 1427–1436.

Silva, R., & Alcaniz, J. S. (2004). Non-extensive statistics and the stellar polytrope index. *Physica A Statistical Mechanics and its Applications*, *341*, 208–214.

Strateva, I., Ivezić, Ž., Knapp, G. R., Narayanan, V. K., Strauss, M. A., Gunn, J. E., Lupton, R. H., Schlegel, D., Bahcall, N. A., Brinkmann, J., Brunner, R. J., Budavári, T., Csabai, I., Castander, F. J., Doi, M., Fukugita, M., Győry, Z., Hamabe, M., Hennessy, G., Ichikawa, T., Kunszt, P. Z., Lamb, D. Q., McKay, T. A., Okamura, S., Racusin, J., Sekiguchi, M., Schneider, D. P., Shimasaku, K., & York, D. (2001). Color Separation of Galaxy Types in the Sloan Digital Sky Survey Imaging Data. *AJ*, *122*, 1861–1874.

Syer, D., & White, S. D. M. (1998). Dark halo mergers and the formation of a universal profile. *MNRAS*, *293*, 337–+.

Taruya, A., & Sakagami, M.-A. (2003). Gravothermal catastrophe and Tsallis' generalized entropy of self-gravitating systems. (III). Quasi-equilibrium structure using normalized /q-values. *Physica A Statistical Mechanics and its Applications*, *322*, 285–312.

Taylor, J. E., & Navarro, J. F. (2001). The Phase-Space Density Profiles of Cold Dark Matter Halos. *ApJ*, *563*, 483–488.

Tremaine, S., Henon, M., & Lynden-Bell, D. (1986). H-functions and mixing in violent relaxation. *MNRAS*, *219*, 285–297.

Trott, C. M., & Webster, R. L. (2002). Dissecting a galaxy: mass distribution of 2237+0305. *MNRAS*, *334*, 621–630.

Tsallis, C. (1988). Possible generalization of Boltzmann-Gibbs statistics. *Journal of Statistical Physics*, *52*, 479–487.

Tsallis, C., Mendes, R. S., & Plastino, A. R. (1998). The role of constraints within generalized nonextensive statistics. *Physica A: Statistical and Theoretical Physics*, *261*, 534–554.

Tully, R. B., & Fisher, J. R. (1977). A new method of determining distances to galaxies. *A&A*, *54*, 661–673.

Vallejo, O., Braine, J., & Baudry, A. (2002). The stellar mass to light ratio in the isolated spiral NGC 4414. *A&A*, *387*, 429–440.

van Albada, T. S., & Sancisi, R. (1986). Dark matter in spiral galaxies. *Royal Society of London Philosophical Transactions Series A*, *320*, 447–464.

van den Bosch, F. C., Mo, H. J., & Yang, X. (2003). Towards cosmological concordance on galactic scales. *MNRAS*, *345*, 923–938.

van Dokkum, P. G. (2001). Cosmic-Ray Rejection by Laplacian Edge Detection. *PASP*, *113*, 1420–1427.

Van Hese, E., Baes, M., & Dejonghe, H. (2008). The dynamical structure of dark matter halos with universal properties. *ArXiv e-prints*, `http://lanl.arxiv.org/abs/0809.0901`.

Williams, L. L. R., Babul, A., & Dalcanton, J. J. (2004). Investigating the Origins of Dark Matter Halo Density Profiles. *ApJ*, *604*, 18–39.

Willis, J. P., Hewett, P. C., & Warren, S. J. (2005). The discovery of two new galaxy-galaxy lenses from the Sloan Digital Sky Survey. *MNRAS*, *363*, 1369–1375.

Willis, J. P., Hewett, P. C., Warren, S. J., Dye, S., & Maddox, N. (2006). The OLS-lens survey: the discovery of five new galaxy-galaxy strong lenses from the SDSS. *MNRAS*, *369*, 1521–1528.

Winn, J. N., Hall, P. B., & Schechter, P. L. (2003). Mass and Dust in the Disk of a Spiral Lens Galaxy. *ApJ*, *597*, 672–679.

Winn, J. N., Kochanek, C. S., McLeod, B. A., Falco, E. E., Impey, C. D., & Rix, H.-W. (2002). PKS 1830-211: A Face-on Spiral Galaxy Lens. *ApJ*, *575*, 103–110.

York, D. G., Adelman, J., Anderson, J. E., Jr., Anderson, S. F., Annis, J., Bahcall, N. A., Bakken, J. A., Barkhouser, R., Bastian, S., Berman, E., Boroski, W. N., Bracker, S., Briegel, C., Briggs, J. W., Brinkmann, J., Brunner, R., Burles, S., Carey, L., Carr, M. A., Castander, F. J., Chen, B., Colestock, P. L., Connolly, A. J., Crocker, J. H., Csabai, I., Czarapata, P. C., Davis, J. E., Doi, M., Dombeck, T., Eisenstein, D., Ellman, N., Elms, B. R., Evans, M. L., Fan, X., Federwitz, G. R., Fiscelli, L., Friedman, S., Frieman, J. A., Fukugita, M., Gillespie, B., Gunn, J. E., Gurbani, V. K., de Haas, E., Haldeman, M., Harris, F. H., Hayes, J., Heckman, T. M., Hennessy, G. S., Hindsley, R. B., Holm, S., Holmgren, D. J., Huang, C.-h., Hull, C., Husby, D., Ichikawa, S.-I., Ichikawa, T., Ivezić, Ž., Kent, S., Kim, R. S. J., Kinney, E., Klaene, M., Kleinman, A. N., Kleinman, S., Knapp, G. R., Korienek, J., Kron, R. G., Kunszt, P. Z., Lamb, D. Q., Lee, B., Leger, R. F., Limmongkol, S., Lindenmeyer, C., Long, D. C., Loomis, C., Loveday, J., Lucinio, R., Lupton, R. H., MacKinnon, B., Mannery, E. J., Mantsch, P. M., Margon, B., McGehee, P., McKay, T. A., Meiksin, A., Merelli, A., Monet, D. G., Munn, J. A., Narayanan, V. K., Nash, T., Neilsen, E., Neswold, R., Newberg, H. J., Nichol, R. C., Nicinski, T., Nonino, M., Okada, N., Okamura, S., Ostriker, J. P., Owen, R., Pauls, A. G., Peoples, J., Peterson, R. L., Petravick, D., Pier, J. R., Pope, A., Pordes, R., Prosapio, A., Rechenmacher, R., Quinn, T. R., Richards, G. T., Richmond, M. W., Rivetta, C. H., Rockosi, C. M., Ruthmansdorfer, K., Sandford, D., Schlegel, D. J., Schneider, D. P., Sekiguchi, M., Sergey, G., Shimasaku, K., Siegmund, W. A., Smee, S., Smith, J. A., Snedden, S., Stone, R., Stoughton, C., Strauss, M. A., Stubbs, C., SubbaRao, M., Szalay, A. S., Szapudi, I., Szokoly, G. P., Thakar, A. R., Tremonti, C., Tucker, D. L., Uomoto, A., Vanden Berk, D., Vogeley, M. S., Waddell, P., Wang, S.-i., Watanabe, M., Weinberg, D. H., Yanny, B., & Yasuda, N. (2000). The Sloan Digital Sky Survey: Technical Summary. *AJ*, *120*, 1579–1587.

York, T., Jackson, N., Browne, I. W. A., Wucknitz, O., & Skelton, J. E. (2005). The Hubble constant from the gravitational lens CLASS B0218+357 using the Advanced Camera for Surveys. *MNRAS*, *357*, 124–134.

Zavala, J., Núñez, D., Sussman, R. A., Cabral-Rosetti, L. G., & Matos, T. (2006). Stellar

polytropes and Navarro Frenk White halo models: comparison with observations. *Journal of Cosmology and Astro-Particle Physics*, *6*, 8–+.